NUMERICAL SIMULATIONS OF PARTICLE TURBULENT DISPERSION AND DEPOSITION WITH IMPLICATIONS FOR THE SPREADING OF AIRBORNE DISEASES

Akim Lavrinenko

UNIVERSITAT ROVIRA i VIRGILI

Numerical simulations of particle turbulent dispersion and deposition with implications for the spreading of airborne diseases

Akim Lavrinenko

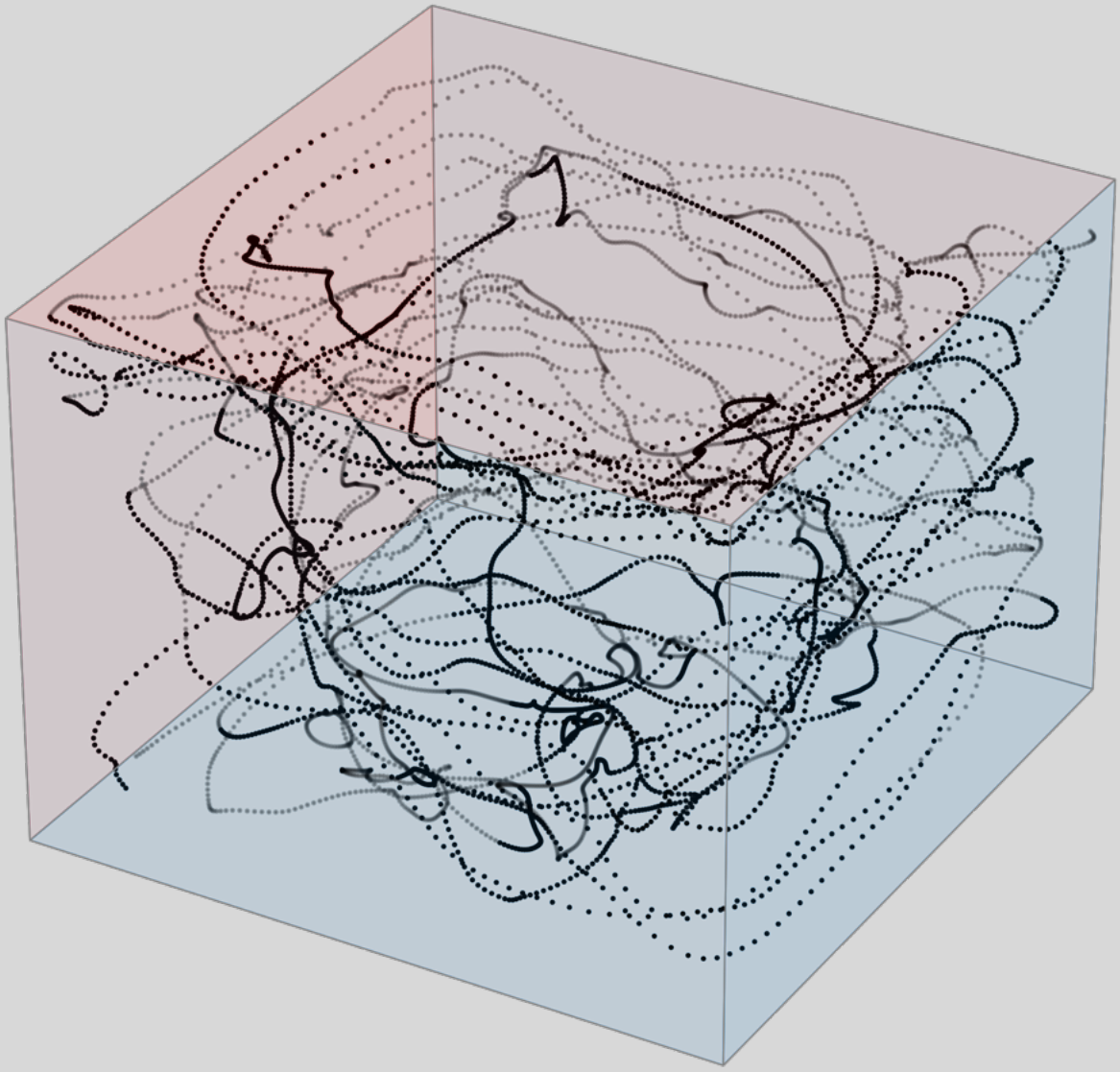

DOCTORAL THESIS
2023

UNIVERSITAT ROVIRA I VIRGILI
NUMERICAL SIMULATIONS OF PARTICLE TURBULENT DISPERSION AND
DEPOSITION WITH IMPLICATIONS FOR THE SPREADING OF AIRBORNE DISEASES
Akim Lavrinenko

UNIVERSITAT
ROVIRA i VIRGILI

Numerical simulations of particle turbulent dispersion and deposition with implications for the spreading of airborne diseases

DOCTORAL THESIS

Author:
AKIM LAVRINENKO

Supervisor:
Prof. ALEXANDRE FABREGAT
Prof. JORDI PALLARES

A thesis submitted in fulfillment of the requirements
for the degree of Doctor of Philosophy

Departament d'Enginyeria Mecànica

UNIVERSITAT ROVIRA I VIRGILI
Tarragona

November 22, 2023

UNIVERSITAT ROVIRA I VIRGILI
NUMERICAL SIMULATIONS OF PARTICLE TURBULENT DISPERSION AND
DEPOSITION WITH IMPLICATIONS FOR THE SPREADING OF AIRBORNE DISEASES
Akim Lavrinenko

Declaration of Authorship

I state that the present study, entitled: **"Numerical simulations of particle turbulent dispersion and deposition with implications for the spreading of airborne diseases"** presented by AKIM LAVRINENKO for the award of Doctor of Philosophy, has been carried out under our supervision at the Department of Mechanical Engineering of Rovira i Virgili university.

Tarragona, October 5, 2023

Supervised by:

FABREGAT TOMAS, ALEXANDRE (AUTENTICACIÓN)
Firmado digitalmente por FABREGAT TOMAS, ALEXANDRE (AUTENTICACIÓN)
Fecha: 2023.10.06 11:05:09 +02'00'

Prof. ALEXANDRE FABREGAT

PALLARES CURTO, JORGE MARIA (FIRMA)
Firmado digitalmente por PALLARES CURTO, JORGE MARIA (FIRMA)
Nombre de reconocimiento (DN): c=ES, serialNumber=39683027T, sn=PALLARES, givenName=JORGE MARIA, cn=PALLARES CURTO, JORGE MARIA (FIRMA)
Fecha: 2023.10.05 16:11:39 +02'00'

Prof. JORDI PALLARES

"The highest activity a human being can attain is learning for understanding, because to understand is to be free."

Baruch Spinoza

UNIVERSITAT ROVIRA I VIRGILI

Abstract

Departament d'Enginyeria Mecànica

Doctor of Philosophy

Numerical simulations of particle turbulent dispersion and deposition with implications for the spreading of airborne diseases

by AKIM LAVRINENKO

This thesis embarks on a numerical examination of particle transport within turbulent flows, using both a particle-laden jet flow generated by a violent expiratory event (mild sneeze or cough) and a cubical cavity with differentially heated walls driving a large-scale recirculating turbulent flow with particles as case studies.

Study shows that violent expiratory event can be divided into two distinct stages. The initial stage, commencing immediately after exhalation and lasting approximately 2 s, is characterized by turbulent particle dispersion primarily driven by the jet/puff flow resulting from the rapid exhalation. Following this initial 2 s period, a second stage emerges as a substantial portion of the turbulent kinetic energy dissipates due to viscosity. In this subsequent stage, the primary factors influencing particle dispersion shift to ambient air currents influenced by natural and artificial factors, such as room temperature gradients, or forced convection mechanisms like heating and ventilation. The research begins with an exploration of the ability of different numerical methodologies in predicting the behavior of particle-laden jet flows. Specifically Direct Numerical Simulation and Unsteady Reynolds Averaged Navier-Stokes equations with a $k-\epsilon$ turbulence model by comparing both methodologies in the context of particle cloud dispersion during the first stage of a mild cough or sneeze. This comparison demonstrated that the Unsteady Reynolds Averaged Navier-Stokes model is capable of simulating the dynamics of the cough-induced flow capturing key topological features of the resulting thermal jet/puff. The role of particle size was underscored, with the observation that particles smaller

than 64 µm ascend due to the drag force exerted by the warm buoyant puff created by the cough, while the particles with a diameter of 64 µm and larger tend to follow parabolic paths due to dominant gravitational forces. Nonetheless, when compared to fully resolved simulation results, the vertical dispersion of the thermal and particle cloud were found to be underestimated in the Unsteady Reynolds Averaged Navier-Stokes solution.

Following the initial investigations of turbulent particle dispersion in case of respiratory events, the research delves into the outcomes of the "2022 International Computational Fluid Dynamics Challenge on Violent Expiratory Events" organized by the Department of Mechanical Engineering of Universitat Rovira i Virgili and the Department of Engineering and Architecture of the university of Udine (Italy). The goal was to assess the effectiveness of various computational codes, turbulence models and computational grid resolution in accurately modeling particle short-term dispersion on a larger scale. The results demonstrated that the most of the models in current study can provide reasonable estimates of the shape and dynamics of the buoyant thermal cloud. Nonetheless, a consistent underestimation of vertical turbulent mixing was noted, especially in the Unsteady Reynolds Averaged Navier-Stokes-based models. Furthermore, when juxtaposed with Direct Numerical Simulation results, both Unsteady Reynolds Averaged Navier-Stokes and Large-Eddy Simulation approaches were found to overstate the horizontal dispersion of smaller particle clouds. These findings emphasize the need for more precise modeling techniques in turbulent jet aerosol dispersion, supporting the conclusions from earlier stage of the study.

One more crucial topic of this study is the exploration of aerosol transport in buoyancy-driven turbulent flows within enclosed spaces. Research continues with the investigation of the second stage of a violent expiratory event which resembles long-term long-range particle cloud dispersion. Research results provides insight into how turbulent intensity and increased advection velocities within the wall boundary layers impact aerosol dispersion rates. It suggests that a spherical cloud of particles ranging in diameter from 0.1 to 2.5 µm can be homogeneously distributed

within a $\sim$3 m side room in $\sim$500 s after release in considered conditions. The particle dispersion is driven by the large-scale recirculation flow produced by a temperature difference in the walls of the cavity with a Rayleigh number of 3.6×10^9. The comparison of the fully resolved simulations with analytical models show the limitation of these models in accurately predicting mixing time of particle clouds.

The work further investigates the turbulent dispersion and deposition of airborne solid particles in a cubical cavity with two pairs of differentially heated opposed walls. Numerical setups mimics the experimental conditions of measurements reported in the literature, which allows to make direct comparison of numerical and experimental results. The study is focused on the determination of the effects of particle size, solid-gas density ratio, and the hydrodynamics within the thermal and momentum boundary layers near solid surfaces. On top of that the study closed the gap in the literature and extends the wall-averaged Nusselt number correlations up to a Rayleigh number of 3.6×10^9 and presents deposition rates in line with both experimental data and analytical boundary layer solutions.

In summary, this doctoral work covers several aspects of particle dispersion and deposition dynamics in varied airflow conditions, utilizing numerical simulations and comparing results with existing experimental results and theoretical models. The insights derived can have far-reaching implications for developing more accurate models of short and long-term aerosol particle transport, safety guidelines that help to mitigate virus-laden aerosol infestation as well as surface soiling and turbulence modeling in natural convective multiphase flows.

UNIVERSITAT ROVIRA I VIRGILI
NUMERICAL SIMULATIONS OF PARTICLE TURBULENT DISPERSION AND
DEPOSITION WITH IMPLICATIONS FOR THE SPREADING OF AIRBORNE DISEASES
Akim Lavrinenko

Acknowledgements

I would like to express my deepest appreciation to everyone who has significantly contributed to my PhD research journey.

I extend my sincerest gratitude to my advisors, Dr. Alexandre Fabregat and Dr. Jordi Pallares. Their invaluable guidance, continuous support, and patience have been instrumental in this research work and my personal and professional growth.

My heartfelt acknowledgment goes out to my wife, Marina Buklagina. Her endless love, encouragement, understanding, and support have been my backbone throughout this endeavor.

Special recognition goes to the committee members of the Doctoral Programme in Nanoscience, Materials, and Chemical Engineering, particularly Núria Juanpere and Professor Alex Fragoso. Their constant encouragement, insightful feedback, and assistance in navigating the program's administrative requirements have been of immense value.

I am deeply grateful to Lluís Vàzquez Vilamajó, our department manager, for his efficient management skills and readiness to assist with various organizational and research-related aspects. His contributions have made this research journey smoother and more enjoyable.

My colleagues at the URV Mechanical Engineering Department, particularly the ECoMMFIT research group, have my heartfelt thanks for their invaluable collaboration and intellectual exchanges. Your support has significantly enriched my research experience.

To my friends and colleagues at Lab 121, I am incredibly thankful. Your friendship, camaraderie, and willingness to lend a hand when needed have made a significant difference in my PhD journey. I am grateful to be part of such an amazing community.

I extend my appreciation to the jury committee members for their time and constructive critique on my dissertation.

Finally, I acknowledge the financial support provided by the Spanish Ministerio de Ciencia, Innovación y Universidades through grants DPI2016-75791-C2-1-P, RTI2018-100907-A-I00 (MCIU/AEI/FEDER, UE) and PID2020-113303 GB-C21, as

well as by the Generalitat de Catalunya through grant 2017-SGR-1234 and 2021 SGR 00732.

In closing, my deepest gratitude goes out to everyone who has been part of this enriching journey. This work would not have been possible without your support and collaboration. Thank you.

List of contributions

- **Journal articles**
  - Lavrinenko, A., Fabregat A., Pallarès, J.; Comparison between fully resolved and time-averaged simulations of particle cloud dispersion produced by a violent expiratory event, Acta Mechanica Sinica, 38, 721489, DOI:10.1007/s10409-022-09032-x.
  - Lavrinenko, A., Gisbert, F., Pallarès, J., Fabregat, A.; Fully-resolved numerical simulations of the turbulent flow and particle deposition in a cubical cavity with two pairs of differentially heated opposed walls at Rayleigh number 3.6 x 109, International Communications in Heat and Mass Transfer 141(5):106564, DOI: 10.1016/j.icheatmasstransfer.2022.106564.
  - Pallarès, J., Fabregat, A., Lavrinenko, A.,... Cito, S.; Numerical simulations of the flow and aerosol dispersion in a violent expiratory event: Outcomes of the "2022 International Computational Fluid Dynamics Challenge on violent expiratory events", Physics of Fluids 35, 045106 (2023), DOI: 10.1063/5.0143795.
  - Submitted on 04.10.2023: Lavrinenko, A., Fabregat, A., Gisbert, F., Pallarès, J.; Direct Numerical Simulation of pathogen-laden aerosol dispersion in buoyancy-driven turbulent flow within confined spaces, International Communications in Heat and Mass Transfer.
- **Conference contributions**
  - Lavrinenko, A., Fabregat A., Pallarès, J.; Using Direct Numerical Simulations to investigate the dispersion of pathogen-laden aerosols in buoyancy-driven turbulent flows in enclosed spaces, URV 17th Doctoral Day of Nanoscience, material and chemical engieering, May 2022, Tarragona, Spain.
  - Fabregat, A., Lavrinenko, A., Pallarès, J.; Airbone disease transmission and Fluid Dynamics: Direct Numerical Simulations of a violent expiratory event and the dispersion of the resulting droplet cloud, 1st Spanish Fluid Mechanics Conference, June 2022, Cádiz, Spain.

  - Pallarès, J., Fabregat, A., Lavrinenko, A.,... Cito, S.; Outcomes of the "2022 International Computational Fluid Dynamics Challenge on violent expiratory events", URV 18th Doctoral Day of Nanoscience, material and chemical engieering, May 2023, Tarragona, Spain.
  - Pallarès, J., Lavrinenko, A., Cito, S., Vernet, A., Fabregat, A.; Short and long term dispersion of airborne pathogen-laden aerosols expelled in a violent expiratory event, 2nd Spanish Fluid Mechanics Conference, July 2023, Barcelona, Spain.
  - Pallarès, J., Lavrinenko, A., Fabregat, A.; Aerosol dispersion generated by a turbulent natural convection flow in a room-sized two-dimensional square enclosure, 10th International Symposium on Turbulence, Heat and Mass Transfer, September 2023, Rome, Italy.

- **Oral presentations**

  - Fabregat, A., Lavrinenko, A., Pallarès, J.; Using Direct Numerical Simulations to investigate the dispersion of pathogen-laden aerosols in buoyancy-driven turbulent flows in enclosed spaces, 6th International Conference on Turbulence and Interactions, May 2022, Elba Island, Italy.
  - Lavrinenko, A., Fabregat, A., Pallarès, J.; Particle wall deposition in turbulent natural convection flows in enclosed cavities with thermally active walls, From Stokesian suspension dynamics to particulate flows in turbulence, August 2022, Toulouse, France.
  - Lavrinenko, A., Fully-resolved numerical simulations of the turbulent flow, particle deposition and dispersion in cubical cavity with two pairs of differentially heated opposed walls at $Ra = 3.6 \times 10^9$, URV, February 10th, Tarragona, Spain.

Contents

Chapter 1

Introduction

Within Fluid Mechanics field, flows are typically categorized into two types: laminar and turbulent. Laminar flow is characterized by smooth, orderly motion, while turbulent flow is distinguished by its chaotic and irregular changes in pressure and flow velocity.

Turbulent flows are ubiquitous in nature and engineering systems. They span from smaller scales such as arterial blood flow or the movement of exhaled air, to larger scale occurrences including weather patterns and stellar nebulae formations. They are essential in applications related to aerospace, naval, and automotive technologies, as well as in energy production, the transport of oil and gas, water distribution, civil engineering and public health. Turbulence complexity is rooted in the high non-linearity that governs its dynamics. Ability to predict turbulent flows hold key to advancements across multiple fields. We can enhance technologies, improve system efficiencies, and enrich our understanding of our surroundings. Famous Nobel laureate physicist Richard Feynman claimed that turbulence is the most important unsolved problem of classical Physics.

The introduction of particles adds another layer of complexity, resulting in particle-laden turbulent flow. Particles are tiny solid or liquid droplets suspended in the fluid. They can interact with the turbulence, altering the flow structure. Tracking particles in turbulent flows enables the visualization and quantification of turbulent formations, shedding light on its fundamental nature. This understanding plays a crucial role in multiple applications, such as mitigating airborne diseases, preventing the soiling of valuable surfaces, and addressing environmental pollution, and many others.

1.1 Background and Literature Review

In this section, a brief and general overview of the literature related to the topic of this thesis is provided. A detailed description and relevant list of references can be found in the introduction sections of each chapter of the document (2, 3, 4, and 5) which corresponds to journal papers that constitute main body of the thesis.

The advent of modern Fluid Dynamics can be traced back to early 19-th century when pioneers like Claude-Louis Navier and Sir George Gabriel Stokes laid the foundations for the study of viscous fluid flow. Navier launched the discipline in 1822, and Stokes significantly expanded upon it in 1845. Their collective contributions culminated in the well-renowned system of Navier-Stokes equations which describes viscous fluid flow [1, 2].

Both Navier and Stokes played critical roles in advancing our understanding of fluid behavior, and their contributions continue to be foundational in the field. The Navier-Stokes equations remain a central element of research in fluid mechanics and are widely used to model fluid flow in a variety of scientific and engineering applications.

The same year Stokes introduced Stokes Law, which describes the drag force experienced by small spherical particles moving through a viscous fluid [3]. In the late 19-th century Reynolds published results of his experimental work on fluid flows. His seminal research led to the inception of the Reynolds number, serving as a critical predictive tool in flow behavior studies [4]. Building upon this foundational understanding, early explorations into the gravity-induced motion of a sphere in a stationary fluid were undertaken by Basset [5]. This work was later augmented by contributions from Boussinesq and Oseen [6, 7]. Their collective hypothesis postulated that the disturbance generated by the sphere's movement, when Reynolds numbers are sufficiently low, allowed the fluid force on the sphere to be calculated using the results derived from unsteady flow with very low Reynolds number, also known as Stokes flow. Later, Taylor formulated the dispersion theory, which explains how turbulent flows can increase the effective diffusivity of a species, thereby enhancing its dispersion [8]. Wells research in 1934 led to the development of the

Wells curve [9], which predicts the behavior of small droplets after a violent expiratory event. Coughing or sneezing triggers the production of a large number of respiratory droplets, originating from saliva or respiratory mucus, which vary in size, typically ranging from 1 µm to 2 mm. Subsequently, in the mid-20th century, Kolmogorov revolutionized our understanding of turbulent flow dynamics by introducing the energy cascade concept and formulating the energy spectrum [10]. Expanding upon this basis, Tchen [11] extended the investigation of particle-laden flow to a more intricate setting. Initially, he expanded the study to a sphere settling under gravity within a fluid exhibiting unsteady yet uniform flow. He delved further into a more challenging scenarios involving an unsteady and non-uniform flow, aiming to provide insights applicable to turbulent flows. Around the same time, Obukhov further enriched our comprehension of turbulent dispersion with contributions to the understanding of the energy cascade in turbulent flows. He worked on elucidating the transfer of energy from large-scale eddies to smaller-scale eddies in turbulent systems [12]. Meanwhile Batchelor further refined the theories of Kolmogorov, providing understanding of energy spectra, dissipation, and scaling laws in homogeneous turbulence [13].

Then, Corrsin and Lumley [14] critically evaluated Tchen's work [11], noting some inconsistencies in his equation. Despite their critical remarks, the equation proposed by Corrsin and Lumley also faced scrutiny for potentially oversimplifying the influences in the undisturbed flow. Specifically, the equation emphasized the effects of pressure gradients over those of viscous shear stress, when both factors might be of comparable importance. This discrepancy was highlighted by Buevich [15]. He revisited the original Basset-Boussinesg-Oseen equation using a change of reference frame to a coordinate system moving with the particle, he derived a new equation of motion. In a contrasting approach, Riley [16] applied a similar analytical methodology but came to a different conclusion, which seems to align more closely with physical expectations. This concept becomes particularly evident when examining a small sphere, where the size is notably smaller compared to the spatial variations of the undisturbed flow [17]. Pursuing this line of investigation further, Maxey and Riley advanced the development of a motion equation specifically tailored for small particles navigating turbulent flows [17]. This ground-breaking model was designed

to account for the intricate interplay of non-uniform fluid dynamics and the inherent inertia of the particles. In doing so, their work enriched our understanding of particle behaviour in complex systems and further bridged the gap between theory and the physical reality of turbulent particle-laden flows. These cumulative efforts have shaped the study of turbulent particle-laden flows, creating a robust theoretical foundation.

Nazaroff and Cass [18] applied this knowledge and presented an indoor aerosol model that integrates both aerosol size distribution and chemical composition, accommodating for multiple aspects such as ventilation, filtration, deposition, indoor emissions, and coagulation, while also enabling future investigations into gas-to-particle conversion processes. The experimental study of indoor particle transport of Xu et al. [19], who used a room-sized chamber for measurements, aims to provide an accurate understanding of aerosol particle deposition rates and their health implications. Thatcher et al. [20] in their experimental study present an examination of the behavior of airborne particles in indoor environments. The study emphasizes the distinctiveness of indoor settings, especially their larger surface-to-volume ratio, which considerably influences the deposition rates. The authors explore the role of natural convection, and how surface-to-air temperature gradients can induce thermophoretic forces on particles, thereby altering deposition patterns. Results show direct measurement of particle deposition rates under diverse conditions and at multiple locations, offering comprehension for the refinement of surface deposition models and an enhanced understanding of the deposition processes in indoor settings.

The foundation of this thesis is based on the authors mentioned above and recent work of Fabregat and Pallares, who conducted Direct Numerical Simulation (DNS) study on the natural convection flows in cubical cavity with two pairs of opposed walls at different temperatures [21]. Firstly, they aimed to address a gap in the existing literature, specifically targeting the investigation of flow and heat transfer rates for this configuration in the range of $10^6 < Ra \leq 5.4 \times 10^8$. They emphasized the demand for ongoing research in this area.

Further deepening their exploration, they incorporated Exponential-Lagrangian Tracking Schemes (ELTS) into their DNS to investigate the transport and deposition

of airborne particles on solid surfaces, setting the Rayleigh number equal to 5.4×10^8 [22]. The methodology they employed successfully mirrored the experimental conditions previously studied by Thatcher et al. [20], providing valuable data for comparison and further analysis. Additionally, Pallares and Fabregat embarked on the development of a boundary layer model with a specific aim of predicting the deposition rates of airborne particles within a cubic room [23]. Their work provides theoretical tool for predicting the behavior of particulate matter in enclosed spaces, advancing the field of study.

During the tumultuous course of the COVID-19 pandemic, it became increasingly clear that one of the primary modes of transmission for the SARS-CoV-2 virus is airborne. The DNS study of Fabregat et al. [24] provides insights into the short-range transmission of airborne diseases, which is largely facilitated through airborne droplets and aerosols produced when an infected person talks, coughs, or sneezes. Understanding the dynamics of the flow induced by respiratory events is crucial for predicting the dispersion and spread of virus-laden particles. In continuation of this study [25] they highlights the crucial role of airborne particles in the short-term transmission of COVID-19 and other infectious diseases. The dispersion dynamics of these particles are largely influenced by their size and evaporation rates. The larger droplets are mostly dominated by gravity, while smaller aerosol particles, primarily transported via hydrodynamic drag, can stay afloat for extended periods of time. In environments with subsaturated air, the dispersion of these pathogen-laden particles becomes complex due to the evaporation of the water content. Rapid evaporation rates can result in a shift from buoyancy- to drag-dominated dispersion regimes, significantly altering particle dynamics. To study the impact of particle size and evaporation on the evolution of pathogen-laden clouds, the authors conducted a DNS of the first stage of a mild cough, combined with an evaporative Lagrangian particle advection model. The findings indicate that while evaporation effects are unlikely to disrupt the dispersion of particles on the tails of the size distribution, particles of specific sizes (30–40 µm) may exhibit increased residence time and horizontal range under typical ambient conditions. Further to this Pallares and Fabregat developed a model to predict short-term aerosol cloud dispersion, considering factors like intensity, duration, and density difference between carrier and dispersed

phase [26].

1.2 A short description of the work

This dissertation presents an extensive examination of airborne particle transport dynamics within turbulent flows, contributing new insights to our understanding of this complex phenomenon. Doctoral research delves into two relevant study cases: (i) particle propagation during a violent expiratory event, and (ii) turbulent natural convection, dispersion, and deposition of airborne particles within enclosed spaces. The research is divided into two interrelated components, each addressing one of these areas. The conclusions drawn from the research have been compiled into four academic papers, detailed within the introduction chapter in the 1.3 section, and presented in the 2, 3, 4, and 5 chapters of this thesis.

The first area of focus is the short-term short-range dispersion of particles during violent expiratory events. Previous studies of Fabregat et al. [24, 25] suggest a two-stage dispersal process. Initially at the first stage, turbulent particle dispersion is principally driven by the jet/puff flow instigated by the rapid exhalation. Simulations approximate the particle cloud to take the shape of a sphere with a radius of about 0.3 m by the end of this phase [27]. Approximately 2 s post-exhalation, the second stage begins, marked by the dissipation of a substantial fraction of the turbulent kinetic energy due to viscosity. Particle dispersion is then primarily influenced by background ambient air currents, which can be affected by natural factors like temperature gradients within the room or artificial forced convection mechanisms, such as Heating, Ventilation, and Air Conditioning (HVAC) systems and others [28]. Thus, the long-term distribution and mixing properties of the particle clouds are largely contingent upon large-scale ambient flows.

To investigate first stage of violent expiratory event, Unsteady Reynolds-Averaged Navier-Stokes (URANS) simulations were conducted, and the results were compared against the DNS. An URANS simulation was employed to replicate the flow setup used by Fabregat et al. [24, 25], who numerically studied the first stage of the idealized flow resulting from a mild cough. During the URANS simulations, an extensive mesh independent study was performed, which raised several questions

regarding the grid resolutions and turbulence model requirements. These questions eventually led to the organization of an international CFD challenge aimed at addressing these issues titled the "2022 International Computational Fluid Dynamics Challenge on violent expiratory events" organised by University of Rovira i Virgili and University of Udine (Italy). This research initiative aimed to evaluate the effectiveness of different CFD codes, turbulence models and numerical grids in reproducing the short-term flow and short-range dispersion associated with a first stage of typical violent expiratory event. The challenge was divided into two parts, each addressing a critical aspect of the problem. First, to evaluate and compare the performance of different numerical methods and turbulence models in reproducing the predictions of DNS for an unsteady jet flow during an idealized exhalation event. This involves assessing the ability of each combination of method and model to accurately capture the rapid, but short-lived, injection of warm air into a previously still ambient environment (Stage I of the Challenge). Second, to investigate the influence of particle size and evaporation on the dispersion of the aerosol cloud generated during the exhalation event. This includes comparing the simulation results obtained from DNS with the results of the challenge participants. The aim is to quantify the impact of these factors on the dispersion behavior of the particle clouds (Stage II of the Challenge).

In the second part of the thesis we explored the long-term pathogen-laden particle cloud dispersion, when aerosol clouds are advected by large-scale buoyancy-driven flows which are regular for indoor environments. Leveraging DNS coupled with a Lagrangian Particle Tracking (LPT) scheme, the airflow and pathogen-laden particles were modelled within a cubic room with side lengths of approximately 3 m, subjected to a temperature differential of 1.24 K applied to two pairs of opposing differentially heated walls. Analyzing particle trajectories, the spatial dependence of particle cloud mixing time for a given particle size were investigated and compared with established dispersion regimes using the particle relative dispersion and variance of the particle concentration. Furthermore, the turbulent diffusion coefficient from the temporal evolution of the particle relative dispersion was calculated to quantify particle cloud spread and diffusion within the room. The results

from our computationally expensive DNS approach were evaluated against predictions from closed-form models, specifically a novel developed Gaussian model and a semi-analytical model from the literature, to assess their predictive capabilities regarding mixing rates under idealized flow conditions.

In relation to the aforementioned topics, the final chapter of the thesis addresses particle deposition. Thatcher et al. [20] conducted compelling experiments to investigate particle deposition rates on smooth surfaces, focusing on particles ranging from 0.1 to 2.5 µm in size. Reproducing their experimental setup numerically, Fabregat and Pallares [21, 23, 22] conducted investigations using DNS coupled with a LPT scheme to study the hydrodynamics and particle deposition at Rayleigh number 5.4×10^8. Extending the analysis performed by Fabregat and Pallares up to a Rayleigh number of 3.6×10^9, the objective of this chapter is twofold: To assess the validity of the wall-averaged Nusselt number correlation over a broader range of Rayleigh numbers to close existing gap in the literature and to compare the numerical results of the wall-average particle deposition rates with the experimental data reported by Thatcher et al. [20] and the boundary layer solutions presented by Pallares and Fabregat [23].

In chapter 6 of this dissertation conclusions are made, simulation data based analysis provides valuable insights into the complex dynamics of particle transport within turbulent flows, making contributions to the study of turbulent particle-laden flows, particle dispersion, and deposition. The findings presented herein hold implications not only for researchers studying violent expiratory events but also serve as a valuable guideline for modeling such events. Additionally, the results offer crucial initial conditions for simulating of the second stage of violent expiratory event, while the analysis of particle cloud dispersion in enclosed rooms can aid in validating particle cloud mixing time predictions. Furthermore, the deposition results hold practical importance for individuals involved in the development of cost-effective computational methods for predicting particle deposition phenomena and those who are keen on simulating this phenomenon in advanced setups. Overall, this research expands our understanding of particle-laden flows and their applications, paving the way for future advancements in related fields.

In the concluding section of this study, we discuss potential research topics that

could deepen our comprehension of this intricate subject. Future research directions in this field should focus on enhancing our understanding and management of aerosol dynamics during violent expiratory events. Key areas for investigation include the incorporation of realistic anatomy, integration of body movements, and exploration of complex environments. Additionally, investigating the Nusselt number versus Rayleigh Number correlation for enclosed turbulent flow driven by natural convection is essential for model refinement. By pursuing these avenues, we can improve the accuracy and comprehensiveness of our models, leading to better predictions of particle dispersion and deposition. Ultimately, this research has significant implications for public health and safety, enabling the development of effective strategies for mitigating airborne diseases and advancing air filtration methodologies.

1.2.1 Methods and tools

The core of this research lies in the numerical solution of the Navier-Stokes equations. Several methodologies have been used in this process, including Direct Numerical Simulation, Large-Eddy Simulation (LES), and Unsteady Reynolds Averaged Navier-Stokes (URANS). The Computational Fluid Dynamics is essential for understanding multiphase flows, comprising both carrier and dispersed phases.

DNS is a powerful numerical method for solving the Navier-Stokes equations without the need for turbulence models. It resolves the entire range of spatial and temporal scales of turbulence, resulting in highly realistic flow representations. However, due to its significant computational demands, DNS is most suitable for relatively simple flows at moderate Reynolds numbers. While it provides exhaustive and accurate results, its applicability is limited by its high computational cost.

LES is a hybrid approach that combines the benefits of DNS and turbulence modeling. In LES, the large-scale turbulent structures are resolved, while the small-scale structures are modeled. This allows for a more efficient simulation compared to DNS, as only the most energetic eddies are explicitly resolved. LES strikes a balance between accuracy and computational cost, making it suitable for a wide range of turbulent flows.

URANS is another commonly used approach for turbulent flow simulations which today is widely used in engineering. It involves time-averaging the Navier-Stokes equations to obtain a set of equations that can be solved for the time-averaged flow quantities. URANS equations require turbulence models to close the equations, as they introduce additional unknown terms representing turbulent stresses. These turbulence models are based on empirical data and introduce additional level of modeling uncertainty.

Each of these approaches has its strengths and limitations, and their choice depends on the specific characteristics of the flow being simulated, desired results accuracy and the available computational resources.

The research further ventures into the intricacies of multiphase flows, which signify the co-current movement of materials of two or more phases. The complexities embedded in such flows make their characterization and quantification more demanding than those of single-phase flows. A widely employed approach for modeling multiphase flow is the Euler-Lagrange method, where the fluid phase is treated as a continuum, resolved by the Navier-Stokes equations, while the dispersed phase is represented by tracking numerous particles employing a Lagrangian Tracking Scheme with one-way coupling.

This method centralizes on monitoring individual particles as they traverse the fluid flow, offering a detailed view of the particles trajectories, velocities, and accelerations. In the context of particle-laden flows, the one-way coupling approach is a computational technique employed when the influence of particles on the fluid is insignificant. However, the fluid's impact on the particles is paramount. Essentially, it presumes that the fluid flow fields, such as velocity and pressure, determine the particle motion, but the presence of the particles does not modify the fluid flow fields. An additional simplification in our case is that there is no interaction between the particles themselves.

For the DNS our research used NEK5000 [29], an open-source spectral element method (SEM) based solver for the incompressible Navier-Stokes equations. Developed by the Mathematics and Computer Science Division of Argonne National Laboratory, NEK5000 is highly scalable and recognized for its algorithmic performance. The basis functions in SEM are Nth-order tensor-product Lagrange polynomials,

leading to a linear unsteady Stokes problem solved at each time step.

The computational power for these extensive fully-resolved calculations was provided by the Marenostrum4 supercomputer, located at the Barcelona Supercomputing Center. Despite the considerable computational cost of DNS, the capabilities of Marenostrum4 enabled comprehensive DNS, generating substantial data amounts. URANS simulations were carried out using OpenFOAM [30], an open-source toolbox offering various numerical solvers and pre-/post-processing utilities. OpenFOAM includes solvers for mentioned flow conditions, including incompressible, compressible, single and multiphase flows with heat transfer.

Lastly, post-processing of the simulation data obtained from NEK5000 and OpenFOAM was conducted using Python in-house developed code. Data visualization was achieved with Paraview and Visit [31, 32], both open-source software tools, facilitating a comprehensive understanding of the fluid flow dynamics under this study.

1.2.2 Objectives

The general aim of this thesis is to develop a advanced understanding of the transport dynamics of particles within turbulent flows, with a specific focus on violent expiratory events, and distribution of aerosols in enclosed environments with temperature gradients. This involves improving our knowledge on turbulence modeling, computational fluid dynamics, particle transport, as well as comparing and validating various models and numerical results with experimental data. One of the study's ultimate goal is to provide valuable insights and recommendations for improving the predictability of turbulent particle-laden transport modeling.

The overarching objectives of this thesis can be summarized as follows:

1. **Investigation of turbulent particle transport modeling in violent expiratory event:** The primary aim is to discern the variances in the trajectories of thermal puffs and particle clouds introduced by modeling the turbulent transport using a $k-\epsilon$ model. This objective focuses on addressing the challenges posed by URANS due to the transient nature of the flow during a cough event and the rapid decay of turbulence intensity once the exhalation ceases. This part of the study will strive

to shed light on the balance between computational requirements and accuracy in predicting exhaled particle cloud dynamics.

2. **Analysis of an international CFD challenge results of simulations of the flow in violent expiratory events:** This objective revolves around an international CFD challenge to evaluate the proficiency of different modeling approaches in reproducing the dynamics of a initial stage of prototypical violent expiratory event. This challenge aims to bring together different methodologies and computational tools, and hence, the goal is to analyze and compare the results submitted by the participants who used different CFD codes, computational grids and turbulence models. Study provides foundation for efficient and accurate modelling of turbulent jet particle-laden flows.

3. **Advanced analysis of pathogen-laden particle cloud dispersion in enclosed spaces:** The third objective is to asses aerosol mixing capabilities, focusing on the long-term particle transport (second stage of a violent expiratory event), particularly when the dispersion particle clouds is advected by large-scale buoyancy-driven flow. Using DNS coupled with LPT, the aim is to model airflow and pathogen-laden particles within an enclosed environment. The study intends to examine the spatial dependence of the mixing time for the particle clouds and quantify the dispersion characteristics, providing valuable insights into the dispersion of aerosols in indoor environment. This objective seeks to provide enriched understanding of turbulent aerosol dispersion and also validate Gaussian models against results derived from the DNS. A new Gaussian model, based on an instantaneous aerosol point source, is used to compute particle concentrations within a cubical room experiencing large-scale recirculating flow. This then is compared to mixing times calculated using variance of the particle concentration from the DNS results, and against predictions from a semi-analytical model proposed by Lau et al. [33].

4. **Evaluation of Wall-Averaged Nusselt Number correlation and particle deposition rates in cubical cavity:** The final objective is to extend the analysis of previous studies of particle deposition on thermally active walls in in the cubical cavity up to a Rayleigh number of 3.6×10^9, with the aim of validating the wall-averaged Nusselt number correlation and comparing the numerical results of wall-average particle deposition rate with experimental and theoretical results. This part of the

research will contribute significantly to our understanding of particle behavior and deposition under varying conditions in enclosed room.

1.3 Overview of thesis

The doctoral thesis consists of four research papers that serve as core content of the thesis. Each paper represents an independent investigation of turbulent airborne particle transport phenomena. Each paper follows a structured format, beginning with a comprehensive introduction featuring relevant references to establish context and background for the research. The introduction sets the stage for the subsequent components of the paper. Following the introduction, each paper presents mathematical and physical model used in the study. This section delves into intricate details concerning the computational domain, the physical model, and includes equations and properties crucial to understand the research. Moving forward, the papers provide a detailed account of the results, showcasing the outcomes of simulations conducted as part of the study. This section offers insights and data derived from the study. Lastly, each paper concludes by summarizing the key findings and main highlights of the investigation. This concluding section provides a concise overview of the research significance and its contribution to the broader field of study. In this way, the doctoral thesis compiles four distinct but interrelated studies, each equipped with a comprehensive structure designed to facilitate understanding and engagement with the research.

Below are presented short summary of each chapter of the thesis.

- Chapter 1: This initial chapter provides a comprehensive introduction, including an in-depth review of the existing literature relevant to the study. It further outlines a brief summary of the undertaken work, elucidates the methodologies and tools employed, and details the principal objectives of this thesis.

- Chapter 2: Comparison between fully resolved and time-averaged simulations of particle cloud dispersion produced by a violent expiratory event.

  This study involves a comparative analysis of Direct Numerical Simulation results of Fabregat et al. [24, 25], and those derived using Unsteady Reynolds

Averaged Navier-Stokes (URANS) equations with a $k-\epsilon$ turbulence model. In both scenarios, the dispersed phase is modeled as spherical Lagrangian particles under the assumption of one-way coupling. Generally, the URANS model successfully captures the upward movement of lighter particles with diameters under 64 µm, driven by the drag exerted by the buoyant puff created when warm exhaled air enters a cooler quiescent environment. Both DNS and URANS concur that particles of 64 µm and larger tend to follow parabolic trajectories as a result of gravitational forces. Results suggests that computational meshes with finer resolution tends to give better results.

A grid independence analysis is carried out to evaluate the impact of enhanced mesh resolution on the statistical behavior of the particle cloud as the flow develops. Findings suggest that chosen model tends to overestimate the horizontal displacement of particles smaller than 64 µm, while it underestimates the displacement for particles larger than 64 µm.

- Chapter 3: Numerical simulations of the flow and aerosol dispersion in a violent expiratory event: Outcomes of the "2022 International Computational Fluid Dynamics Challenge on violent expiratory events"

  This article offers a comprehensive discussion on the outcomes of the "2022 International Computational Fluid Dynamics Challenge on Violent Expiratory Events." This challenge sought to evaluate the efficacy of various computational codes and turbulence models in reproducing the airflow generated by a typical rapid exhalation and the resulting aerosol cloud dispersion. A shared flow setup was provided, upon which seven research teams from different countries conducted a total of 12 numerical simulations of the first stage of idealized violent expiratory event. These simulations employed Unsteady Reynolds Averaged Navier-Stokes equations, Large-Eddy Simulations, or hybrid (URANS-LES) techniques. Each team's results were compared to one another and benchmarked against a Direct Numerical Simulation of the identical flow and ensemble average of 13 LES simulations. The DNS outcomes served as a reference to discern the deviations introduced by each modeling approach. A

total of 12 simulations considering the dispersion of both evaporative and non-evaporative particle clouds were executed using URANS and LES.

Most of the models exhibited decent predictive capability regarding the shape and the horizontal and vertical extents of the buoyant thermal cloud caused by the warm exhalation into a cooler, initially quiescent ambient environment. However, vertical turbulent mixing was generally underestimated, predominantly by URANS-based simulations, regardless of the specific turbulence model used, and to a lesser degree, by LES. When compared to the DNS, both methodologies overpredicted the horizontal range covered by the clouds of small particles (less than 32 µm), which tends to remain suspended within the thermal cloud long after the flow injection has ceased.

- Chapter 4: Using Direct Numerical Simulations to investigate the dispersion of pathogen-laden aerosols in buoyancy-driven turbulent flows in enclosed spaces.

  This study investigates the capability of ambient air currents in an idealized cubic enclosed room for mixing and dispersing an aerosol cloud generated by an exhalation event, using Direct Numerical Simulations. The turbulent flow in the computational domain, representing a closed room with sides of approximately 3 m, is driven by natural convection. By imposing a temperature difference of $\Delta T = 1.24$K between two pairs of diferentially opposite walls, and with the resulting flow occurs at a Rayleigh number of 3.6×10^9 with a Prandtl number of 0.7. This flow is characterized by a dominant large-scale recirculation pattern, with an average air velocity of $0.02\text{m}\,\text{s}^{-1}$, which is typical of background air currents in indoor environments.

  The initial aerosol distribution is modeled by randomly seeding particles within a sphere of radius 0.3 m, which are tracked using a Lagrangian scheme for up to 1.4×10^3 s or $\sim$23 min. Employing relative dispersion of particles clouds and variance of particle concentration to quantify the level of mixing, the results indicate that particle clouds near walls disperse faster than those initially located near the room center, attributable to the enhanced turbulent intensity and large advection velocities generated within the wall boundary layers.

Furthermore, a new analytical model for aerosol cloud dispersion in the enclosed cubic room is developed and its results are compared with the dispersion model from the literature and the DNS. Although closed form models have limited capacity to predict the mixing rate due to the highly inhomogeneous turbulence distribution within the room, they can in some instances provide reasonable estimations of the time required to reach fully mixed conditions in the room.

Overall, particles ranging from 0.1 to 2.5 µm become homogeneously distributed within the first ∼500 s after the release. Both analytical models tend to underestimate time required for reaching fully-mixed conditions compared to the DNS.

- Chapter 5: Fully-resolved numerical simulations of the turbulent flow and particle deposition in a cubical cavity with two pairs of differentially heated opposed walls at Rayleigh number 3.6×10^9.

  The turbulent dispersion and deposition of airborne solid, smooth, spherical particles are investigated using DNS. The computational model replicates the experimental conditions of previously reported measurements [20] within a cubical cavity filled with air and differentially heated opposing walls.

  In this model, the trajectory of each particle is influenced by a balance between five forces: hydrodynamic drag, buoyancy, lift, thermophoresis, and Brownian motion. The major factors affecting particle deposition largely depend on particle size, the solid-gas density ratio, and the dynamics within the thermal and momentum boundary layers near solid surfaces.

  The current results suggest an extension of previous correlations between the wall-averaged Nusselt number and the Rayleigh number within a range from 10^7 to 5.4×10^8 to the Rayleigh number 3.6×10^9. Furthermore, numerical predictions of particle deposition rates on thermally active and smooth surfaces align well with both experimental data and analytical boundary layer solutions for particle sizes varying from 0.1 µm to 2.5 µm in diameter.

These particle sizes allow for the examination of different particle deposition regimes, ranging from those controlled by thermophoresis (0.1 µm) to those dominated by gravitational forces (2.5 µm).

- Chapter 6: This final chapter summarizes the main findings of the research, concluding the thesis. It also proposes potential avenues for future exploration, thereby laying the groundwork for subsequent research in this field.

UNIVERSITAT ROVIRA I VIRGILI
NUMERICAL SIMULATIONS OF PARTICLE TURBULENT DISPERSION AND
DEPOSITION WITH IMPLICATIONS FOR THE SPREADING OF AIRBORNE DISEASES
Akim Lavrinenko

Chapter 2

Comparison between fully resolved and time-averaged simulations of particle cloud dispersion produced by a violent expiratory event

Springer

Acta Mechanica Sinica

CrossMark click for updates

• RESEARCH PAPER •

Acta Mech. Sin., Vol. 38, 721489 (2022)
https://doi.org/10.1007/s10409-022-09032-i

Comparison between fully resolved and time-averaged simulations of particle cloud dispersion produced by a violent expiratory event

Akim Lavrinenko*, Alexandre Fabregat, and Jordi Pallares

Departament d'Enginyeria Mecánica, Universitat Rovira i Virgili, Spain, Av. Països Catalans, Tarragona 26, 43007, Spain

Received January 5, 2022; accepted January 30, 2022; published online April 25, 2022

In this work we compare the DNS results (Fabregat et al. 2021, Fabregat et al. 2021) for a mild cough already reported in the literarure with those obtained with a compressible URANS equations with a k-ϵ turbulence model. In both cases, the dispersed phase has been modelled as spherical Lagrangian particles using the one-way coupling assumption. Overall, the URANS model is capable of reproducing the observed tendency of light particles under 64 μm in diameter to rise due to the action of the drag exerted by the buoyant puff generated by the cough. Both DNS and URANS found that particles above 64 μm will tend to describe parabolic trajectories under the action of gravitational forces. Grid independence analysis allows to qualify the impact of increasing mesh resolution on the particle cloud statistics as flow evolves. Results suggest that the k-ϵ model overpredicts the horizontal displacement of the particles smaller than 64 μm while the opposite occurs for the particles larger than 64 μm.

CFD, Covid-19, DNS, URANS, Lagrangian particle tracking, Cough, Aerosol dispersion

Citation: A. Lavrinenko, A. Fabregat, and J. Pallares, Comparison between fully resolved and time-averaged simulations of particle cloud dispersion produced by a violent expiratory event, Acta Mech. Sin. **38**, 721489 (2022), https://doi.org/10.1007/s10409-022-09032-i

1. Introduction

Throughout history, mankind had to endure several pandemics that have cost many human lives and profoundly affected economic and social spheres on a global scale. In today's global world, the COVID-19 pandemic has had an enormous impact on our lives and has posed a major challenge to public health systems around the world. As of mid-2021 there have been approximately 200 million confirmed cases and just over 4 million deaths [1].

The flow physics plays a central role in the spreading of the infection that occurs when pathogen-laden droplets are spewed into the air when an infected person breathes, talks, coughs or sneezes [2]. Computational fluid dynamics (CFD) has been extensively used to shed some light on the factors that control the ability of these fluid particles to disperse in the environment after being released during respiratory events [3-11].

Mittal et al. [12] pointed out the existing scientific gaps in our understanding of the transmission pathways of respiratory diseases and the strategies for mitigating it. The airflow produced by violent respiratory events contains an average of approximately 25000 particles, as reported by Duguid [13]. Depending on their size and the underlying flow hydrodynamics, these pathogen-laden particles are capable of remaining afloat and disperse by the action of the background air motion enabling disease transmission. The World Health Organization (WHO) and the US Centers for Disease Control and Prevention (CDC) officially acknowledged inhalation of virus-laden aerosols as the main transmission route for SARS-CoV-2 [14, 15].

It is known that different factors such as ambient air humidity and velocity and temperature affect the dispersion and distance travelled by exhaled particles. Wells [16] was one of the first who studied how air humidity and droplet size influences droplet deposition time. Xie et al. [17] and

*Corresponding author. E-mail address: akim.lavrinenko@urv.cat (Akim Lavrinenko)
Executive Editor: Cristian Marchioli

later Chong et al. [18] continued Wells studies. Pendar and Páscoa [19] reported a detailed analysis of the transport characteristics and fluid dynamics for saliva droplets spewed during a sneeze in an indoor environment using a fully-coupled Eulerian-agrangian method. They concluded that the horizontal range of the particle cloud strongly depends on the ambient air conditions. Abkarian et al. [20] modeled a human cough using Large Eddy simulation (LES) with the Lagrangian particle approach in order to analyze flows during breathing and speaking considering the impact of phonetic features. They concluded that virus transmission is enhanced during rapid and excited speech, typical of social gatherings and singing events. The time spent in front of another person is a major factor, too: they recommend speakers to keep a distance of 2 m or more between them for conversations longer than 30 s. Bourouiba et al. [21] experimentally studied coughs and concluded that the turbulent hydrodynamics strongly affects the spatial range of the particle cloud. Dbouk and Drakakis et al. [22] reported that the region of influence of the particle cloud produced by a sneeze under windy conditions is 2-4 times larger than that in the absence of background flow. Their results suggest that, in open spaces, wind can enhance the transport of aerosols far beyond the 2-m separation, a distance considered as safe in many social distancing guidelines. In addition, human physiological factors may also affect the dispersion of the particle cloud. Fontes et al. [23] used Detached Eddy simulation (DES) to study a cough with different saliva properties and different geometries of the nasal and buccal passages. They suggested that differences in the anatomy of the nose and throat have a dramatic impact on the particle spray characteristics. More recently, and on the DNS front, Diwan [24] simulated the hydrodynamics evolution of the first 27.5 s of a dry cough with an in-house code using a mesh with 2.15 billion cells. The authors, however, provided limited results that could be readily used in a validation against URANS. Fabregat et al. [25, 26] also used DNS and Lagrangian particle tracking (LPT) to simulate the initial 1.67 s of a mild cough with evaporating and non-evaporating particles between 4 and 256 μm in diameter.

In this work, an unsteady compressible RANS simulation is used to repeat the exact same flow set-up used by Fabregat et al. [25,26], who numerically investigate the idealized flow produced by mild cough, and compare the results with the DNS reported by these authors. In Ref. [26], it is shown that for for the selected initial conditions, flow setup and computational domain, the evaporation of the particles does not affect significantly particle cloud trajectory. Current study goal is to determine the deviations of the thermal puff and particle cloud trajectories introduced by modeling the turbulent transport using a k-ϵ model. Notably, the transient nature of the flow poses a challenge for URANS due to the transition from laminar to turbulent regimes as the air injection accelerates at the beginning of the cough event and also, later on, due to the turbulence intensity rapid decay once the exhalation has ceased.

All in all, COVID-19 has received a massive response from the research community in wide range of areas. On the CFD field, the need for reliable and computationally affordable methodologies to predict pathogen-laden particles dispersion is still an on-going challenge. This study should shed some light on the trade-off between CPU requirements and accuracy in predicting the dispersion of the aerosol cloud and results may be of interest for those who study numerically jet flows and particle dispersion and modelers who need benchmark results [27]. Also, results may be valuable, as initial conditions, for those interested in simulations of the long term dispersion of pathogen laden aerosols.

2. Physical and mathematical model

The numerical simulation of a violent expiatory event resembling a mild cough is carried out using OpenFoam with the reactingParcelFoam solver. This is a transient solver for compressible, turbulent flow equipped with a reacting multiphase particle module and surface film modelling [28]. This solver has been used to replicate the flow set-up used in Fabregat et al. [25, 26] who used DNS to investigate both the hydrodynamics and particle dispersion in idealized environments. Figure 1 shows a sketch of the computational domain with boundary conditions and coordinate system. The cough is modelled as a transient jet flow of air at constant temperature (34°C) with linearly increasing inlet velocity from 0 m s^{-1} up to 4.8 m s^{-1} at 0.15 s and then a linearly decreasing velocity to 0 m s^{-1} at 0.4 s. The air flow is ejected into a quiescent environment with a temperature of 15°C. Respiratory aerosols are modelled as solid spherical Lagrangian particles continuously ejected with the exhaled air over the duration of the exhalation. To facilitate the comparison of particle dispersion between the DNS in Fabregat et al. [26] and the URANS simulations, we considered here $n = 7$ different particle diameters in the range $2^{(j+1)}$ μm with $j = 1, 2, ..., n$. The exhaled air and the accompanying particles are injected through an inlet of circular section of 2 cm in diameter (see Fig. 1). The motion of the aerosol particles, assumed Lagrangian and spherical, is obtained by solving the set of ordinary differential equations governing their position and velocity. All particle sizes are ejected simultaneously during exhalation. Air is considered to be ideal gas with physical properties calculated using "Janaf polynomials" [29].

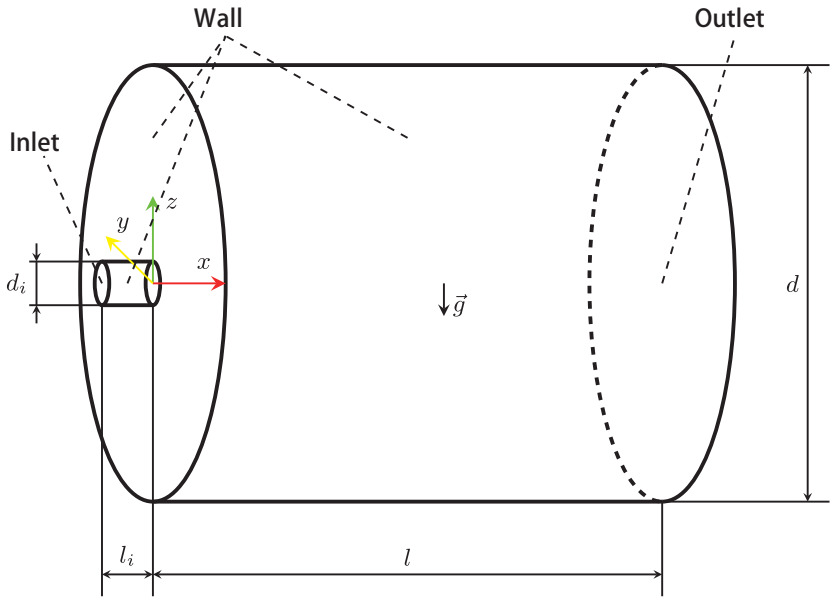

Figure 1 Sketch of the computational domain, l = 1.6 m, d = 1.0 m, l_i = 0.04 m, d_i = 0.02 m. The dimensions of the domain are the same as for the DNS of Fabregat et al. [26]

2.1 Carrier flow transport equations

ReactingParcelFoam solves numerically the system of density weighted time averaged Navier-Stokes equations [30]. The system including the continuity, the momentum and the energy equation [31], which can be written as

$$\frac{\partial \rho}{\partial t} + \frac{\partial}{\partial x_j}(\rho u_j) = 0, \tag{1}$$

$$\frac{\partial}{\partial t}(\rho u_i) + \frac{\partial}{\partial x_j}\left(\rho u_i u_j - \mu_{\text{eff}}\frac{\partial u_i}{\partial x_j}\right) = -\frac{\partial p}{\partial x_i} + \rho g \delta_{i3}, \tag{2}$$

$$\frac{\partial}{\partial t}(\rho h + \rho k) + \frac{\partial}{\partial x_j}\left(\rho u_j h + \rho u_j k - \alpha_{\text{eff}}\frac{\partial h}{\partial x_j}\right) = \frac{\partial p}{\partial x_j} + \rho u_j g \delta_{i3}. \tag{3}$$

In Eqs. (1)-(3), u_i is the i-th component of the density weighted time averaged velocity field in the x_i direction, p is pressure, t is time, u' is the fluctuating part of the velocity, δ_{i3} is the Kronecker delta, ρ is the air density, g is the gravitational acceleration, h is the density weighted time averaged enthalpy, k is kinetic energy, μ_{eff} is the effective viscosity (viscous + turbulent) α_{eff} is the effective thermal diffusivity (diffusive + turbulent).

2.2 Turbulence model

The standard k-ϵ turbulence model for compressible fluid in openFoam 8 has been used [32]. The turbulent kinetic energy dissipation rate and the turbulent kinetic energy are shown in Eqs. (4) and (5) respectively.

$$\frac{\partial}{\partial t}(\rho\epsilon) + \frac{\partial}{\partial x_i}(\rho u\epsilon) - \frac{\partial^2}{\partial x_i^2}(\rho D_\epsilon \epsilon)$$
$$= C_1 \rho G \frac{\epsilon}{k} - \left[\left(\frac{2}{3}C_1 - C_{3,RDT}\right)\rho\frac{\partial}{\partial x_i}u\epsilon\right] - \left(C_2\rho\frac{\epsilon}{k}\epsilon\right)$$
$$+ S_\epsilon + S_{\text{fvOptions}}, \tag{4}$$

where G is turbulent kinetic energy production rate due to the anisotropic part of the Reynolds-stress tensor, D_ϵ is effective diffusivity for ϵ, C_1 and C_2 are model coefficients , $C_{3,RDT}$ is rapid-distortion theory compression term coefficient (Table 1), S_ϵ is internal source term for ϵ and $S_{\text{fvOptions}}$ is source terms introduced by fvOptions dictionary for ϵ.

$$\frac{\partial}{\partial t}(\rho k) + \frac{\partial}{\partial x_i}(\rho u k) - \frac{\partial^2}{\partial x_i^2}(\rho D_\epsilon k)$$
$$= \rho G - \left(\frac{2}{3}\rho\frac{\partial}{\partial x_i}uk\right) - \left(\rho\frac{\epsilon}{k}k\right) + S_k + S_{\text{fvOptions}}, \tag{5}$$

where S_k is internal source term for the k and $S_{\text{fvOptions}}$ is source terms introduced by fvOptions dictionary for k. Turbulence model coefficients are listed in Table 1.

Table 1 Default model coefficients

Coefficient	Value
C_μ	0.09
C_1	1.44
C_2	1.92
$C_{3,RDT}$	0.0
δ_k	1.0
δ_ϵ	1.3

2.3 Dispersed phase transport equations

A particle p is defined by the position of its center $\hat{x}$, its diameter $\hat{d}$, its velocity $\hat{u}_i$ and its density $\hat{\rho}$. For the dispersed phase, the particle motion is solved by integrating the force balance, which can be written in a Lagrangian frame [33]:

$$\frac{\partial \hat{x}_i}{\partial t} = \hat{u}_i, \tag{6}$$

$$\hat{m}\frac{\partial \hat{u}_i}{\partial t} = F_{d,i} + F_{g,i}\delta_{i3}, \tag{7}$$

where $\hat{m} = \frac{\hat{\rho}\hat{d}^3\pi}{6}$ is particle mass, $\hat{u}_i$ is particle velocity, $F_{d,i}$ is the particle drag force, $F_{g,i}$ is apparent weight.

Then spherical particle drag force is

$$F_{d,i} = \hat{m}_i\frac{u_i - \hat{u}_i}{\hat{\tau}}. \tag{8}$$

The relaxation time ($\hat{\tau}$) of the particles is the time it takes for a particle to respond to changes at the local flow velocity, and it is given by [33]

$$\hat{\tau} = \frac{4}{3}\frac{\hat{\rho}\hat{d}}{\rho C_d|u_i - \hat{u}_i|}. \tag{9}$$

The apparent weight is

$$F_{g,i} = (\hat{\rho} - \rho)g_i. \tag{10}$$

The drag coefficient C_d is a function of the particle Reynolds number ($\widehat{Re}$), which is defined as [33]

$$\widehat{Re} = \frac{\rho\hat{d}|u_i - \hat{u}_i|}{\mu}, \tag{11}$$

where μ is the dynamic viscosity of the fluid.

$$C_d = \begin{cases} \dfrac{24}{\widehat{Re}}, & \text{if } \widehat{Re} < 1, \\ \dfrac{24}{\widehat{Re}}(1 + \dfrac{3}{16}\widehat{Re}^{0.687}), & \text{if } 1 < \widehat{Re} < 5, \\ \dfrac{24}{\widehat{Re}}(1 + 0.15\widehat{Re}^{0.687}), & \text{if } 5 < \widehat{Re} < 1000, \\ 0.44, & \text{if } \widehat{Re} > 1000. \end{cases} \tag{12}$$

2.4 Computational grid

Seven different grid resolutions have been considered with the number of cells ranging between 1.8×10^5 and 1.7×10^7. Mesh is generated using the OpenFoam utility called blockMesh, which generates structured hexagonal meshes. The mesh resolution has been increased along the jet axis where larger gradients are expected. Mesh is also refined near the inlet and coarsened progressively along the x axis direction. As an example, Fig. 2 shows a mesh slice at $y = 0$ illustrating the grid cell distribution. Figure 2a shows the entire domain and Fig. 2b a detailed view near the inlet.

Table 2 lists the different cases, with the mesh details and computational cost. Meshes 1 and 2 simulations were carried out using on 8 core Intel(R) Core(TM) i7-6700 CPU @ 3.40GHz while mesh 3 to 7 used 24 core Intel Processor (Haswell, IBRS) 2.3 GHz.

3. Results

3.1 Grid-Independence test

The mesh resolution effect is illustrated in Fig. 3a-g that shows the instantaneous temperature field at $t = 1.5$ s sliced at $y = 0$ for each mesh listed in Table 2. Figure 3h shows, for comparison, the instantaneous temperature field from the DNS by Fabregat et al. [25] at the same time. The colorbar of the temperature field is shown at the bottom of Fig. 3. Results indicate that coarse meshes limit the dispersion of the puff resulting in higher values of temperature along the plume axis. As resolution increases, the temperature field becomes more complex exhibiting richer fine scale structures associated with enhanced mixing, shorter horizontal penetration and lower maximum temperatures.

Figure 4 shows the horizontal (a) and vertical (b) thermal field centroid coordinates (blue lines), the variance (red lines) and the size of the hot puff (black lines) for each mesh in Table 2 at $t = 1.5$ s. The thermal field centroid and variance have been computed as the first and second moment using Eqs. (13) and (14) respectively. The horizontal puff size is determined as the maximum value of the x-coordinate where temperature is above the background unperturbed value. Analogously, the vertical puff size is computed as the difference between the maximum and minimum values of the y-coordinate above which temperature is larger than that corresponding to the unperturbed environment. For comparison purposes, dashed lines indicate the DNS predictions of the thermal puff size, centroid location and variance using the corresponding colors.

$$\tilde{x}_i = \frac{\int_V x_i T \mathrm{d}V}{\int_V T \mathrm{d}V}, \tag{13}$$

$$\tilde{\sigma}_i = \frac{\int_V (x_i - \tilde{x}_i)^2 T \mathrm{d}V}{\int_V T \mathrm{d}V}. \tag{14}$$

In Eqs. (13) and (14), $\tilde{x}_i$ and σ_i are first and second moments (centroid and variance) in each direction i, V is the volume of the computational domain, T is temperature field and x_i is the horizontal or vertical coordinate.

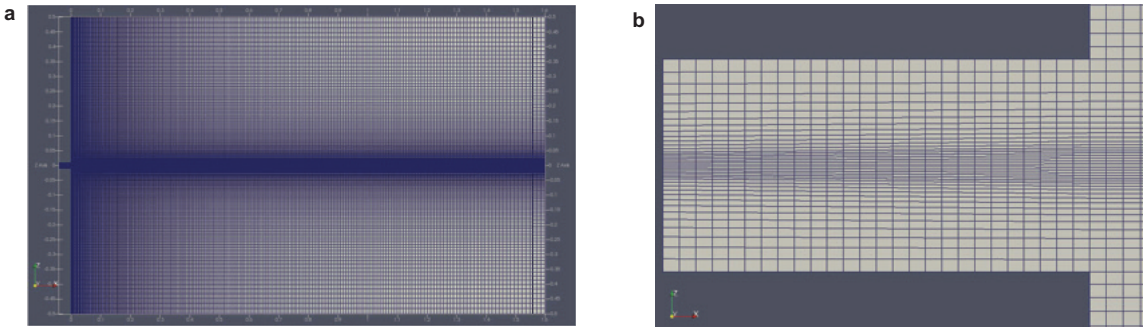

Figure 2 Computational domain slice at $Y = 0$, Mesh 3 (see Table 2). **a** Whole domain; **b** inlet pipe.

Table 2 Mesh details and simulation time for the mesh independence study. CPU hours are calculated for simulation time equal to t=1.5 s. In parenthesis, the used CPU configuration is specified where 1 stands for Intel(R) Core(TM) i7-6700 CPU@3.40GHz and 2 for 24 core Intel Processor (Haswell, IBRS) 2.3 GHz. Min cell is the cube root of minimal cell volume and max cell is the cube root of maximal cell volume, Avg non-ortho is average mesh non-orthogonality.

Mesh ID	Cell count ($\times 10^6$)	CPU-hours	Min cell (m $\times 10^{-4}$)	Max cell (m $\times 10^{-2}$)	Max skewness	avg non-ortho
Mesh 1	0.18	3.49×10^2(1)	6.61	5.12	0.65	2.99
Mesh 2	0.51	4.41×10^3(1)	4.40	3.61	0.69	3.20
Mesh 3	1.0	3.22×10^3(2)	3.27	2.79	0.72	3.31
Mesh 4	3.0	2.92×10^4(2)	2.32	1.96	0.75	3.2
Mesh 5	6.0	2.19×10^4(2)	1.87	1.60	0.76	3.21
Mesh 6	10.0	9.29×10^4(2)	1.56	1.34	0.77	3.22
Mesh 7	17.0	2.66×10^5(2)	1.28	1.12	0.77	3.24

Results in Fig. 4 show that the values of puff size (black lines) only settle when the mesh resolution is above that used in Mesh 5, namely, 6 million cells. In contrast to the thermal puff sizes, horizontal and vertical centroid coordinates (in blue) exhibit a slight tendency to keep decreasing as the resolution increases. The variance of the thermal field, used as a proxy for the thermal puff horizontal and vertical widths, are found to reach a plateau when resolution 1 million cells.

In comparison to the DNS values in Ref. [25], URANS results for both metrics intended to measure the horizontal range attained by the penetrating plume, namely the thermal puff size and the variance, seems to slightly overpredict the DNS results. The larger horizontal centroid coordinate obtained with URANS indicates that this approach tends also to predict a further penetration of the thermal field. All in all, these results suggest that the URANS simulation underpredicts the horizontal turbulent mixing for this flow configuration. Notably, results in Fig. 4b show that URANS underpredicts the vertical thermal puff extent while both the centroid and variance predictions are relatively close to those obtained in the DNS.

3.2 Main results

A snapshot of the particle cloud at the end of the URANS simulation (t = 1.7 s) is shown in Fig. 5 for Mesh 3 (a), Mesh 6 (b) and Mesh 7 (c). Each color represents a particle size ranging from red (4 μm) to magenta (256 μm). At t = 1.7 s almost all the large particles with the diameters of 256 and 128 μm have reached the bottom boundary of the computational domain. On the other hand, particles with diameters of 4 and 16 μm show ascending trajectories due to the updrafting buoyant puff while intermediate sizes of 32 and 64 μm remain afloat while describing slightly descending trajectories. Increasing mesh resolutions from Meshes 3, 6 and 7 leads to a richer particle cloud topology as a results of the finer scales that emerge when the flow hydrodynamics is better resolved. Notably though, the general features and relative positions of every particle size cloud remain pretty similar despite the one order of magnitude difference in the number of cells.

The mesh resolution effect on the particle cloud dispersion is better observed in the temporal evolution of the particle positions projected along the y axis shown in Fig. 6. Each snapshot shows the particle positions (for all sizes) at times t = 0.2 s (a), t = 0.4 s (b), t = 1.0 s (c) and t = 1.7 s (d). Blue, red and green colors correspond to three different selected grid resolutions, namely Meshes 3, 6 and 7, respectively (see Table 2).

Results suggest that as the mesh resolution and time increase, the particle cloud dispersion is enhanced and axial cloud penetration along the axial direction decrease. The signature of the finer flow features that emerge as resolution increases is clearly observed in the green cloud that exhibits

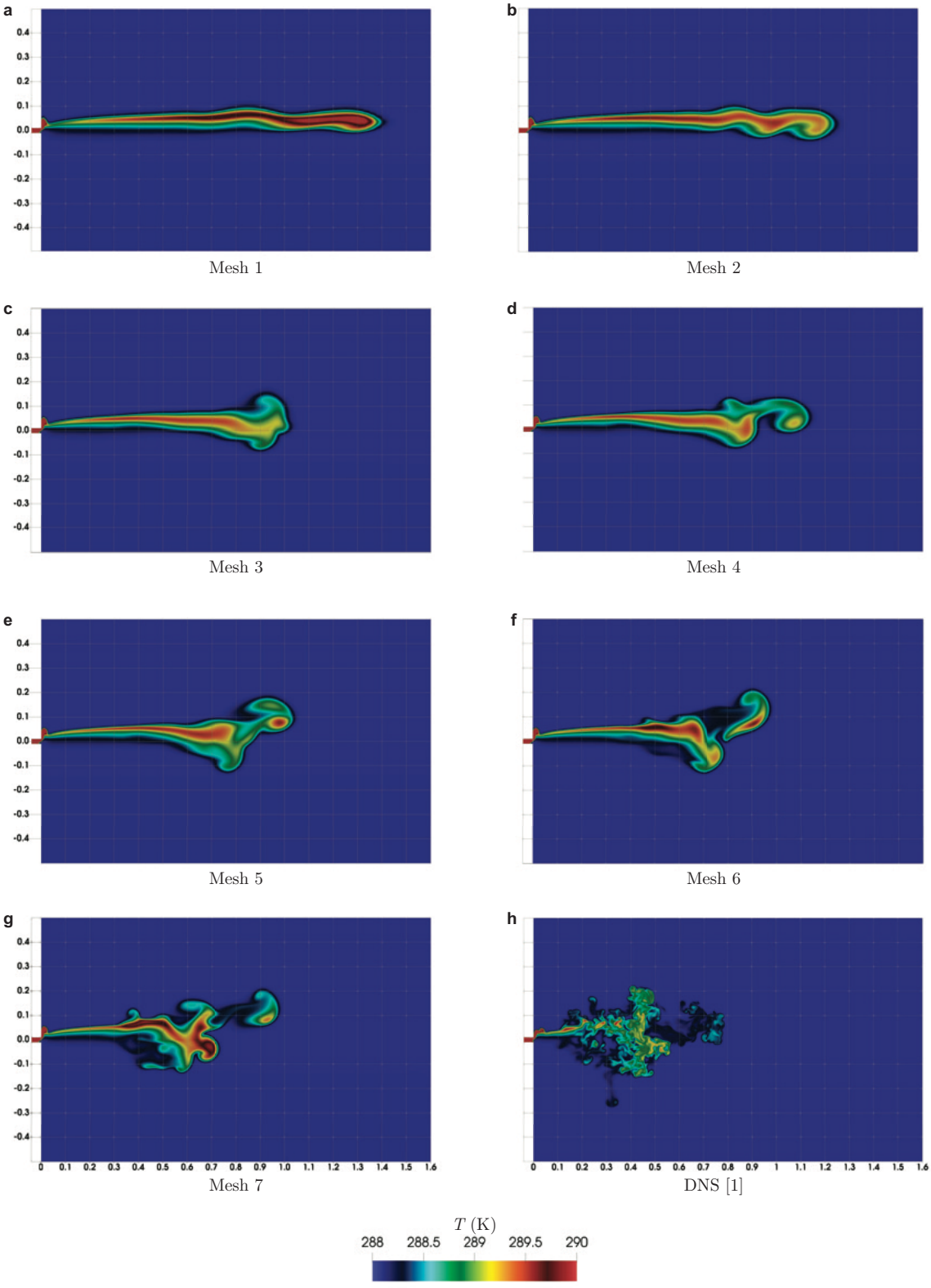

Figure 3 Instantaneous contours of temperature at $Y = 0$ and at $t = 1.5$ s (for mesh resolution details see Table 2)

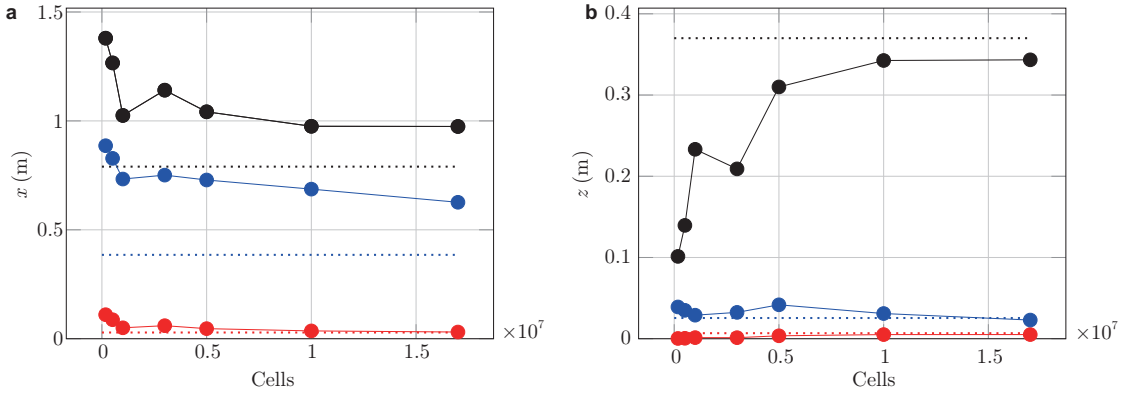

Figure 4 Horizontal **a** and vertical **b** puff size (black), centroid position (blue) and variance (red) at t = 1.5 s as a function of the mesh resolution. Dashed line indicate DNS results from Fabregat et al. [25].

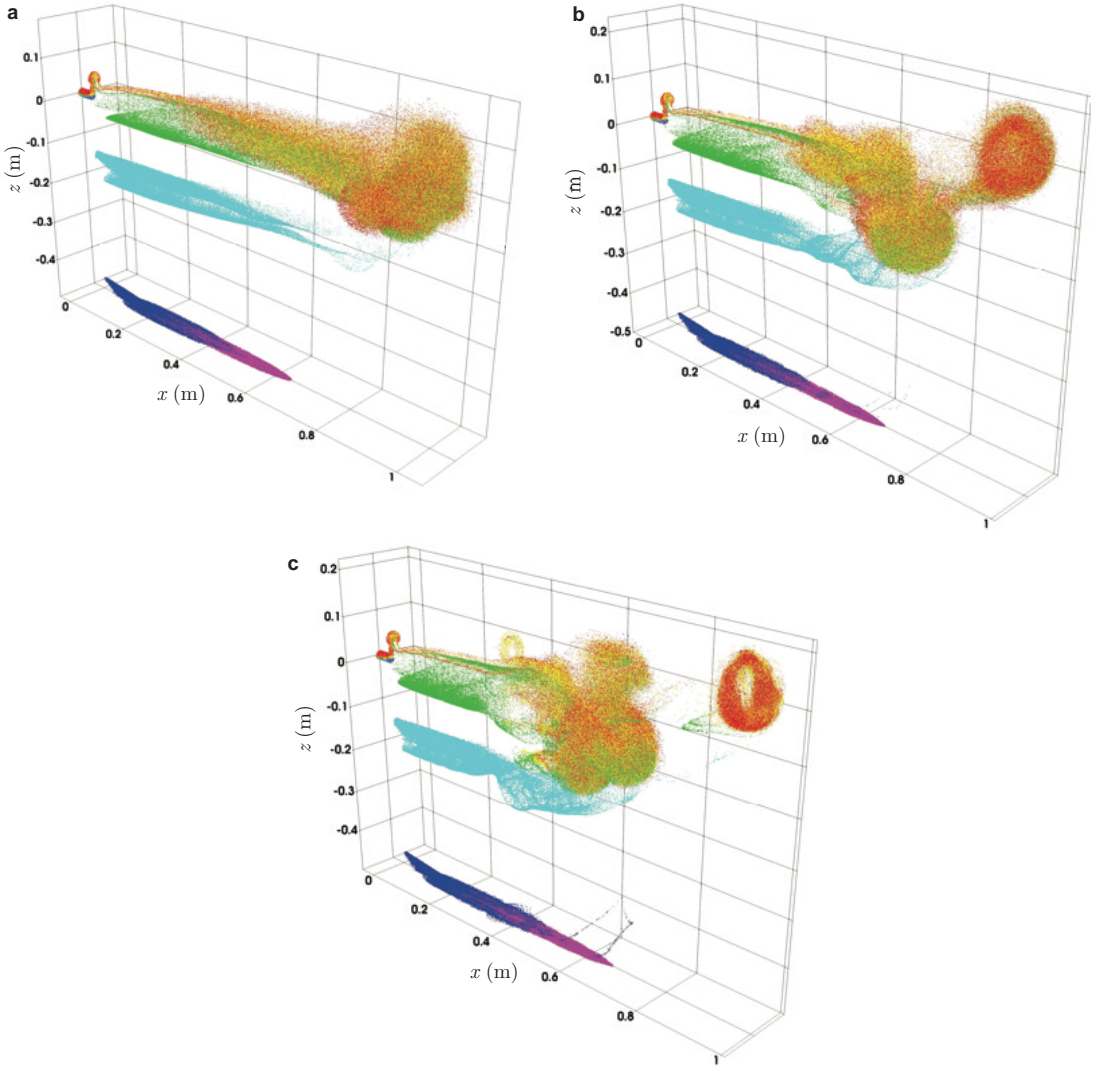

Figure 5 Snapshot of the particle cloud at t = 1.7 s, for Mesh 3 **a**, Mesh 6 **b** and Mesh 7 **c**. Colors indicate particle diameter: red 4 μm, orange 8 μm, yellow 16 μm, green 32 μm, cyan 64 μm, blue 128 μm, magenta 256 μm.

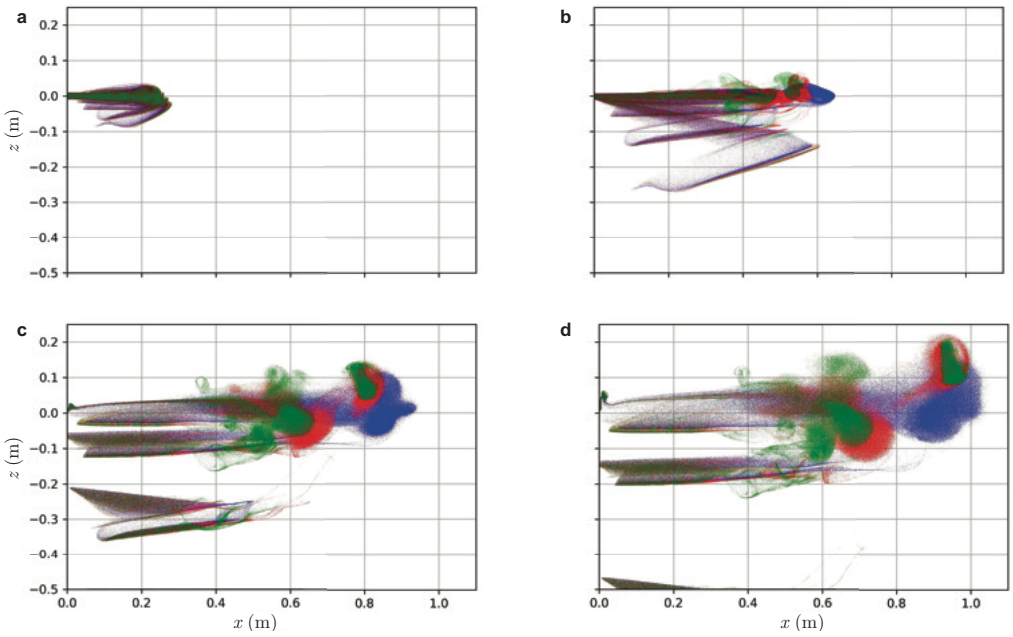

Figure 6 Snapshots of particle clouds at t = 0.2 s **a**, t = 0.4 s **b**, t = 1.0 s **c** and t = 1.7 s **d** produced by simulations with different mesh resolution. Blue, red and green colors represent Meshes 3, 6 and 7, respectively (for mesh details see Table 2).

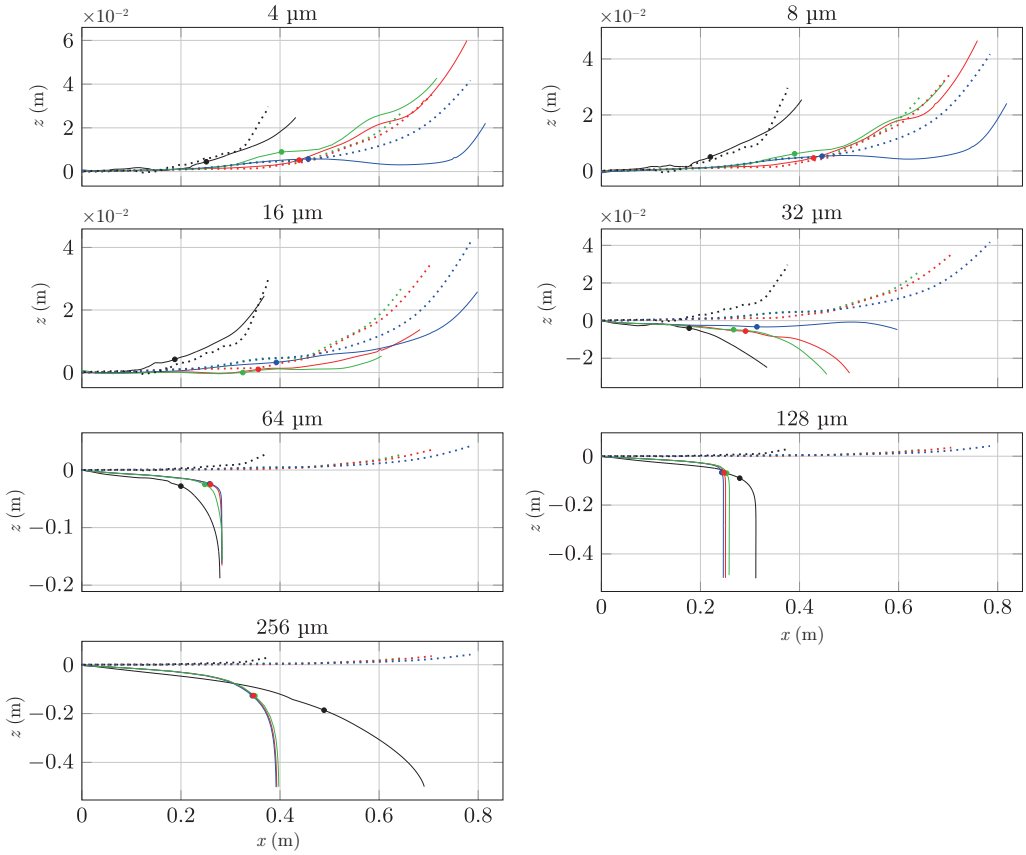

Figure 7 Trajectories of the particle cloud and puff centroids. Lines represents particle cloud trajectory and dashed lines thermal puff trajectory. DNS results are plotted in black. Blue, red and green denotes URANS with Meshes 3, 6 and 7, respectively. The markers in the trajectories of the particle cloud indicate the particle cloud centroid position at the end of the injection (t = 0.4 s).

more convoluted and complex distribution of particle positions in comparison to smaller cell count meshes.

The trajectories of the centroid of the thermal field (dashed line) and the particle cloud (solid line) are shown in Fig. 7. DNS predictions by Fabregat et al. [25, 26] are plotted in black and the present URANS simulations are plotted in blue, red and green for Meshes 3, 6 and 7 respectively. Dot markers indicate the end time of the air injection (t = 0.4 s). The centroid trajectory of the particle cloud is determined as the average coordinates of all airborne particles after discarding those that deposited on the inlet pipe walls. Thermal puff trajectory is calculated using Eq. (13) at each time step.

The transport of the particles between 4 and 16 μm in diameter is dominated by hydrodynamic drag. As a result, the trajectory of the centroid exhibits a vertical deflection imposed by the vertical rising motion of the buoyant puff engulfing them. On the other hand, the particles larger than 64 μm in diameter are dominated by gravitational effects and exhibit a quasi-ballistic trajectories. For lighter particles with diameters from 4 μm to 16 μm URANS overpredicts the travel distance almost by factor of two. The travel distance of the particles with diameter 32 and 64 μm is close to that predicted by DNS. Particles with diameter 64 μm have closest trajectory to the DNS result. URANS underpredicts the travel distance compared to the DNS for particles with diameters 128 and 256 μm. For the latter, the average distance traveled by particles is almost twice smaller.

Figures 8 and 9 show the time evolution of the horizontal and vertical mean velocity of particle cloud over time for each particle size. DNS results are shown in black while

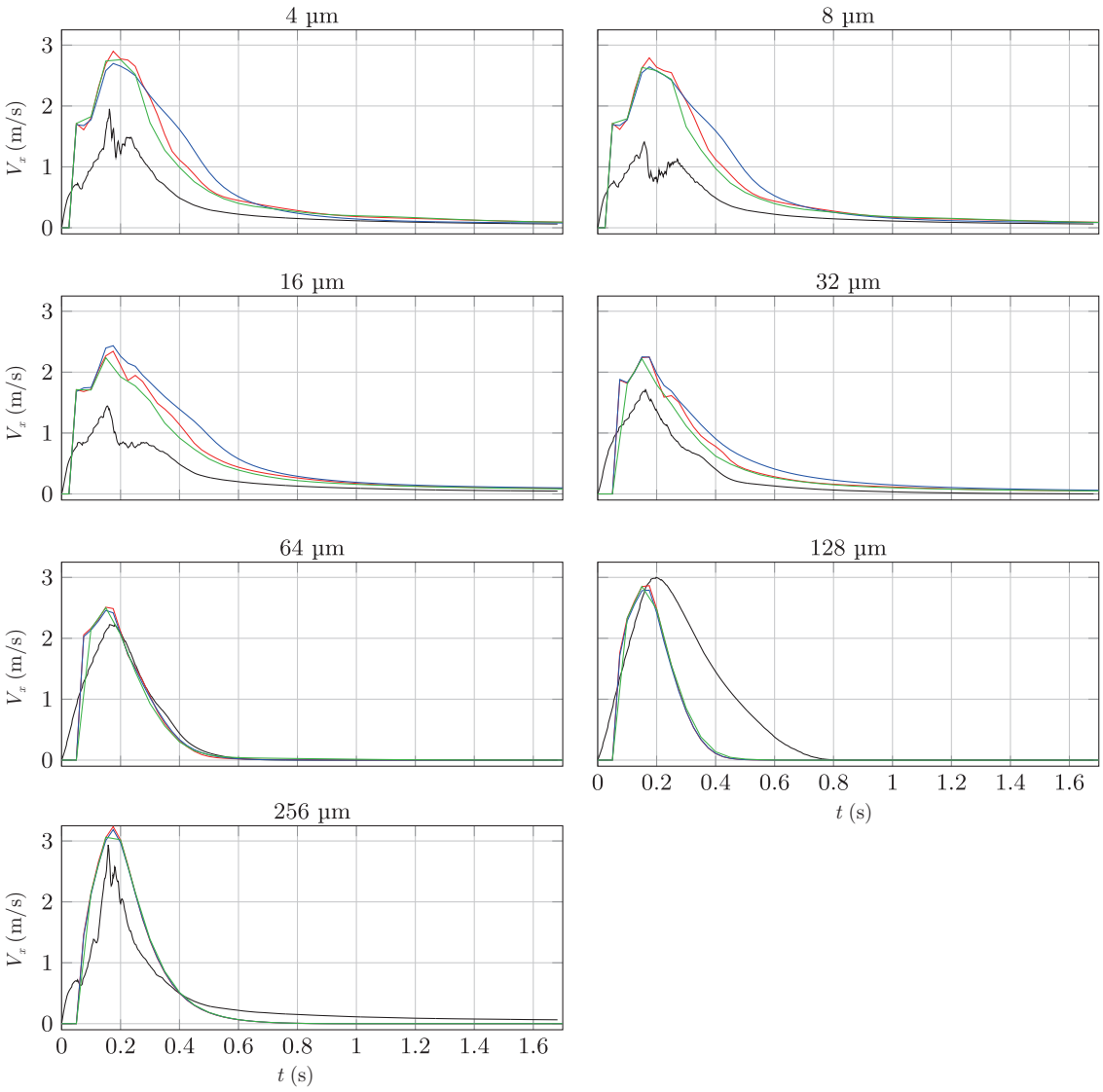

Figure 8 Horizontal velocity of particle cloud over time. Black, blue, red and green line indicates DNS, Meshes 3, 6 and 7, respectively.

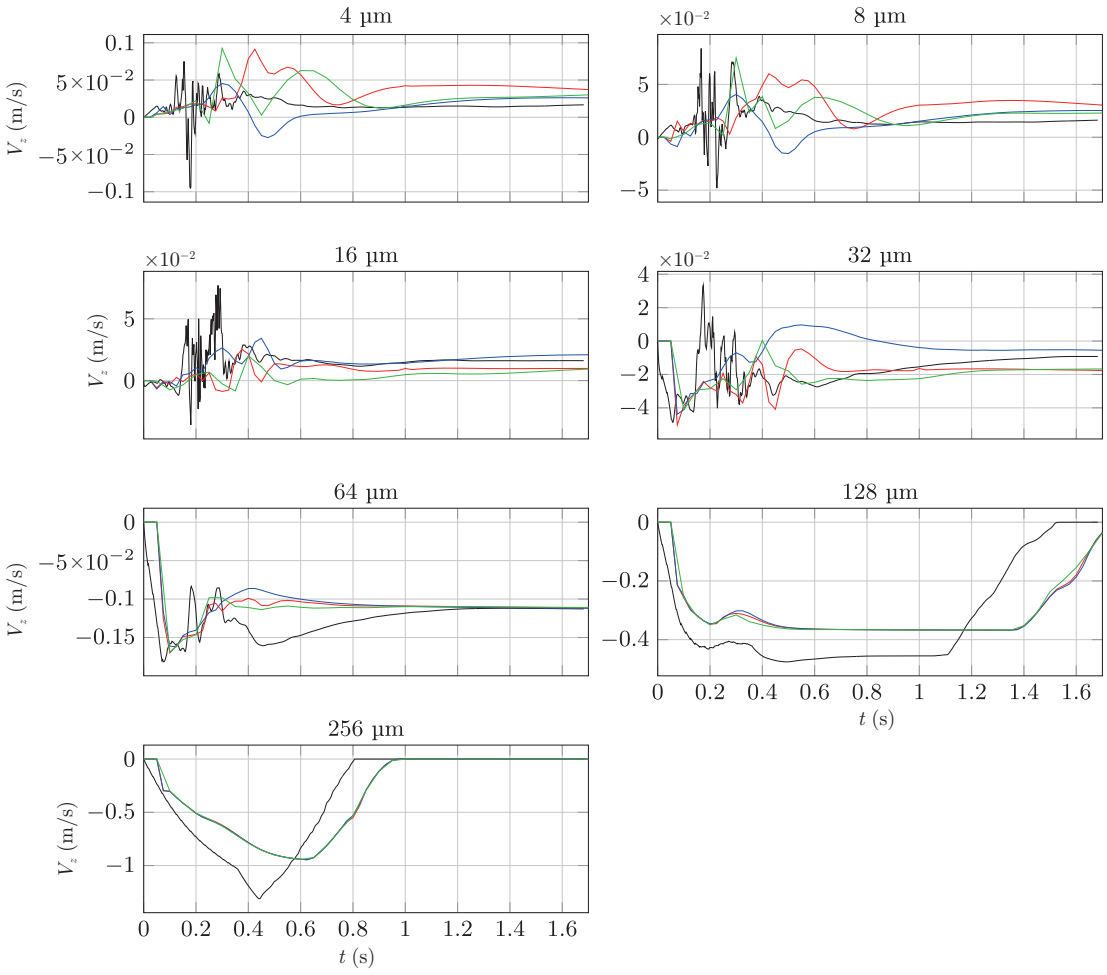

Figure 9 Vertical velocity of particle cloud over time. Black, blue, red and green line indicates DNS, Meshes 3, 6 and 7, respectively.

blue, red and green colors correspond URANS results with Meshes 3, 6 and 7 respectively. In URANS simulations particles leave inlet pipe after t=0.05 s therefore velocity increases not from the beginning of the injection because particles in the inlet pipe are not taken into consideration. In the DNS particles are released at X = 0.0 m [26]. In Fig. 9, when the mean particle cloud velocity is 0 m s^{-1} indicates that all particles has fallen to the bottom boundary of the computational domain. Figure 8 shows that, in comparison to DNS, URANS tends to overpredict the horizontal particle velocity for diameters under 64 µm resulting in larger horizontal ranges as shown in Fig. 7. Regarding particles of 64 µm, URANS and the DNS predictions of horizontal velocity and range are very similar. In contrast, URANS is found to underpredict the horizontal spread of particles with diameter of 128 µm regardless of the mesh resolution. URANS horizontal velocity predictions for the largest particles of 256 µm are in agreement to the DNS results. However, the URANS cloud centroid trajectory departs significantly from the DNS result.

Particles with diameters from 4 µm to 32 µm in Fig. 9 have higher vertical velocities in case of URANS. Vertical velocity of particles with diameter 64 µm converge with the DNS at t = 1.2 s. Both 128 and 256 µm particles vertical mean velocities are slightly lower in case of URANS and as a result particles reach the bottom boundary later as shown in Fig. 7.

4. Conclusion

In this study we used unsteady Reynolds-Averaged Navier-Stokes (URANS) equations to numerically simulate an idealized mild cough modelled as a transient injection of warm air into an initially quiescent colder environment. The rapid air exhalation is accompanied by the injection of spherical particles intended to represent the aerosols spewed into the air when a person coughs. By comparison to existing DNS databases [25] for the exact same flow set-up, we concluded

that URANS is fairly capable of reproducing the general features of the flow hydrodynamics and provide moderately good estimates of the aerosol cloud dispersion. This is relevant given the complex and transient nature of the flow characterized by (i) a laminar to turbulent regime transition during the accelerated air injection and (ii) the rapid turbulence intensity decay once the exhalation has ceased.

Mesh independence analysis allowed to quantify the effect of the cell count on the flow hydrodynamics which, in turn, dominates the particle cloud dispersion specially when the particles are small enough and drag dominates their transport. The impact of the emergence of finer flow features as the mesh resolution increases affecting the hydrodynamics and the turbulent mixing intensity has been quantitatively investigated using several metrics including the thermal field and particle cloud centroid position and variance. Specifically, we found that, as hydrodynamics are better resolved, the trajectory of the particle cloud centroid for diameters in the 4 μm to 32 μm range are closer to those reported in the DNS database [26]. Due to its ability to leave the thermal puff due to gravitational effects, particles above 32 μm in diameter are found to be insensitive to mesh resolution. However, for the meshes considered, the relative positions of every particle size cloud remain pretty similar despite the one order of magnitude difference between the coarsest and finest grids. URANS is found to overpredict the travelled distance of the particles with diameters from 4 μm to 32 μm and otherwise for particle diameters above 64 μm.

This work was supported by Spanish Ministerio de Ciencia, Innovación y Universidades (Grants Nos. RTI2018-100907-A-I00 and PID2020-113303GB-C21), and the Generalitat de Catalunya (Grant No. 2017-SGR-1234).

1 Coronavirus cases, https://www.worldometers.info/coronavirus/coronavirus-cases/.
2 V. Stadnytskyi, C. E. Bax, A. Bax, and P. Anfinrud, The airborne lifetime of small speech droplets and their potential importance in SARS-CoV-2 transmission, Proc. Natl. Acad. Sci. USA **117**, 11875 (2020).
3 A. A. Aliabadi, S. Rogak, S. Green, and K. Bartlett, in Cfd simulation of human coughs and sneezes: A study in droplet dispersion, heat, and mass transfer: Proceedings of the ASME International Mechanical Engineering Congress and Exposition (IMECE), Vancouver, 2010.
4 C. Chen, and B. Zhao, Some questions on dispersion of human exhaled droplets in ventilation room: answers from numerical investigation, Indoor Air **20**, 95 (2010).
5 J. Redrow, S. Mao, I. Celik, J. A. Posada, and Z. Feng, Modeling the evaporation and dispersion of airborne sputum droplets expelled from a human cough, Building Environ. **46**, 2042 (2011).
6 C. Paz, E. Suárez, and J. Vence, CFD transient simulation of the cough clearance process using an Eulerian wall film model, Comput. Methods BioMech. BioMed. Eng. **20**, 142 (2017).
7 G. Kou, X. Li, Y. Wang, M. Lin, Y. Zeng, X. Yang, Y. Yang, Z. Gan, Cfd simulation of airflow dynamics during cough based on ct-scanned respiratory airway geometries, Symmetry **10**, 595 (2018).
8 Z. Li, H. Wang, X. Zhang, T. Wu, and X. Yang, Effects of space sizes on the dispersion of cough-generated droplets from a walking person, Phys. Fluids **32**, 121705 (2020), arXiv: 2010.13348.
9 B. Zhang, G. Guo, C. Zhu, Z. Ji, and C. H. Lin, Transport and trajectory of cough-induced bimodal aerosol in an air-conditioned space, Indoor Built Environ. **30**, 1546 (2021).
10 H. Ge, L. Chen, C. Xu, and X. Cui, Large-eddy simulation of droplet-laden cough jets with a realistic manikin model, Indoor Built Environ. 1420326X2110322 (2021).
11 J. Wang, M. Alipour, G. Soligo, A. Roccon, M. De Paoli, F. Picano, and A. Soldati, Short-range exposure to airborne virus transmission and current guidelines, Proc. Natl. Acad. Sci. USA **118**, 2105279118 (2021).
12 R. Mittal, R. Ni, and J. H. Seo, The flow physics of COVID-19, J. Fluid Mech. **894**, F2 (2020), arXiv: 2004.09354.
13 J. Duguid, The numbers and the sites of origin of the droplets expelled during expiratory activities, Edinburgh Med. J. **52**, 385 (1945).
14 Coronavirus disease (covid-19): How is it transmitted? https://www.who.int/news-room/q-a-detail/coronavirus-disease-covid-19-how-is-it-transmitted.
15 Scientific brief: Sars-cov-2 transmission, https://www.cdc.gov/coronavirus/2019-ncov/science/science-briefs/sars-cov-2-transmission.html.
16 W. F. Wells, On air-borne infection, Am. J. Epidemiol. **20**, 611 (1934).
17 X. Xie, Y. Li, A. T. Y. Chwang, P. L. Ho, and W. H. Seto, How far droplets can move in indoor environments—revisiting the Wells evaporation—falling curve, Indoor Air **17**, 211 (2007).
18 K. L. Chong, C. S. Ng, N. Hori, R. Yang, R. Verzicco, and D. Lohse, Extended lifetime of respiratory droplets in a turbulent vapor puff and its implications on airborne disease transmission, Phys. Rev. Lett. **126**, 034502 (2021), arXiv: 2008.01841.
19 M. R. Pendar, and J. C. Páscoa, Numerical modeling of the distribution of virus carrying saliva droplets during sneeze and cough, Phys. Fluids **32**, 083305 (2020).
20 M. Abkarian, S. Mendez, N. Xue, F. Yang, and H. A. Stone, Speech can produce jet-like transport relevant to asymptomatic spreading of virus, Proc. Natl. Acad. Sci. USA **117**, 25237 (2020), arXiv: 2006.10671.
21 L. Bourouiba, E. Dehandschoewercker, and J. W. M. Bush, Violent expiratory events: On coughing and sneezing, J. Fluid Mech. **745**, 537 (2014).
22 T. Dbouk, and D. Drikakis, On coughing and airborne droplet transmission to humans, Phys. Fluids **32**, 053310 (2020).
23 D. Fontes, J. Reyes, K. Ahmed, and M. Kinzel, A study of fluid dynamics and human physiology factors driving droplet dispersion from a human sneeze, Phys. Fluids **32**, 111904 (2020).
24 S. S. Diwan, S. Ravichandran, R. Govindarajan, and R. Narasimha, Understanding transmission dynamics of COVID-19-type infections by direct numerical simulations of cough/sneeze flows, Trans Ind. Natl. Acad. Eng. **5**, 255 (2020).
25 A. Fabregat, F. Gisbert, A. Vernet, S. Dutta, K. Mittal, and J. Pallarès, Direct numerical simulation of the turbulent flow generated during a violent expiratory event, Phys. Fluids **33**, 035122 (2021).
26 A. Fabregat, F. Gisbert, A. Vernet, J. A. Ferré, K. Mittal, S. Dutta, and J. Pallarès, Direct numerical simulation of turbulent dispersion of evaporative aerosol clouds produced by an intense expiratory event, Phys. Fluids **33**, 033329 (2021).
27 J. Pallares, and A. Fabregat, A model to predict the short-term turbulent indoor dispersion of small droplets and droplet nuclei released from coughs and sneezes, Indoor Built Environ. 1420326X2110600 (2022).
28 Openfoam api guide reactingparcelfoam solver, https://www.openfoam.com/documentation/guides/latest/doc/guide-applications-solvers-lagrangian-reactingParcelFoam.html.
29 J. N. e. a. Bahram Haddadi, Christian Jordan. Openfoam basic training: Tutorial eleven, reactingfoam, 2015, https://www.cfd.at/sites/default/files/tutorials/2014_OFoam_Tut_Example.
30 Favre averaged navier-stokes equations, https://www.cfd-online.com/

Wiki/Favre_averaged_Navier-Stokes_equations.
31 J. Zhang, Modifying coalChemistryFoam for dense gas-solid simulation: Proceedings of CFD with OpenSource Software, 2018, edited by H. Nilsson, http://dx.doi.org/10.17196/OS_CFD#YEAR_2018.
32 k-epsilon turbulence model, https://www.openfoam.com/documentation/guides/latest/doc/guide-turbulence-ras-k-epsilon.html.
33 J. Xu, Modification of stochastic model in Lagrangian tracking method: Proceedings of CFD with OpenSource Software, 2016, edited by H. Nilsson, http://www.tfd.chalmers.se/~hani/kurser/OS_CFD_2016.

粒子云扩散完全解析和时间平均模拟的比较

Akim Lavrinenko, Alexandre Fabregat, Jordi Pallares

摘要 本文将现有文献中轻度咳嗽的直接数值模拟(DNS)结果与k-ϵ模型的可压缩非定常雷诺平均N-S (URANS)方程得到的结果进行了比较. 两种情况均采用单向耦合假设, 将分散相模拟为球形拉格朗日粒子. URANS模型能够再现轻粒子(粒径小于64 μm)的上升趋势, 这归因于咳嗽所产生浮力的阻力作用. 通过分析DNS和URANS的模拟结果发现, 在重力作用下, 大于64 μm的粒子倾向于描述抛物线轨迹. 网格独立性分析允许随着流动的发展, 确定网格分辨率的增加对粒子云统计数据的影响. 结果表明, k-ϵ模型过度预测了直径小于64 μm颗粒的水平位移而对于大于64 μm颗粒的预测则相反.

UNIVERSITAT ROVIRA I VIRGILI
NUMERICAL SIMULATIONS OF PARTICLE TURBULENT DISPERSION AND
DEPOSITION WITH IMPLICATIONS FOR THE SPREADING OF AIRBORNE DISEASES
Akim Lavrinenko

Chapter 3

Numerical simulations of the flow and aerosol dispersion in a violent expiratory event: Outcomes of the "2022 International Computational Fluid Dynamics Challenge on violent expiratory events"

Physics of Fluids

Numerical simulations of the flow and aerosol dispersion in a violent expiratory event: Outcomes of the "2022 International Computational Fluid Dynamics Challenge on violent expiratory events"

Cite as: Phys. Fluids **35**, 045106 (2023); https://doi.org/10.1063/5.0143795
Submitted: 26 January 2023 • Accepted: 10 March 2023 • Accepted Manuscript Online: 11 March 2023 • Published Online: 03 April 2023

Jordi Pallares, Alexandre Fabregat, Akim Lavrinenko, et al.

Physics of Fluids ARTICLE scitation.org/journal/phf

Numerical simulations of the flow and aerosol dispersion in a violent expiratory event: Outcomes of the "2022 International Computational Fluid Dynamics Challenge on violent expiratory events"

Cite as: Phys. Fluids **35**, 045106 (2023); doi: 10.1063/5.0143795
Submitted: 26 January 2023 · Accepted: 10 March 2023 ·
Published Online: 3 April 2023

Jordi Pallares,[1] Alexandre Fabregat,[1,a)] Akim Lavrinenko,[1] Hadifathul Akmal bin Norshamsudin,[2] Gabor Janiga,[2] David F. Fletcher,[3] Kiao Inthavong,[4] Marina Zasimova,[5] Vladimir Ris,[5] Nikolay Ivanov,[5] Robert Castilla,[6] Pedro Javier Gamez-Montero,[6] Gustavo Raush,[6] Hadrien Calmet,[7] Daniel Mira,[7] Jana Wedel,[8] Mitja Štrakl,[9] Jure Ravnik,[9] Douglas Fontes,[10] Francisco José de Souza,[11] Cristian Marchioli,[12] and Salvatore Cito[1]

AFFILIATIONS

[1]Departament d'Enginyeria Mecànica, Universitat Rovira i Virgili, Av. Països Catalans, 26 43007-Tarragona, Spain
[2]Otto von Guericke Universität Magdeburg, Magdeburg, Germany
[3]School of Chemical and Biomolecular Engineering, The University of Sydney, Sydney, Australia
[4]Mechanical and Automotive Engineering, School of Engineering, RMIT University, Bundoora, Victoria 3083, Australia
[5]Higher School of Applied Mathematics and Computational Physics, Peter the Great St. Petersburg Polytechnic University, 29 Polytechnicheskaya str., St. Petersburg 195251, Russia
[6]CATMech-Fluid Mechanics Department, Universitat Politècnica de Catalunya, C/Colom, 1-11, 08222 Terrassa, Spain
[7]Barcelona Supercomputing Center (BSC), Plaça Eusebi Güell, 1-3, 08034 Barcelona, Spain
[8]Institute of Applied Mechanics, University of Erlangen Nuremberg, Erlangen, Germany
[9]Faculty of Mechanical Engineering, University of Maribor, Smetanova 17, SI-2000 Maribor, Slovenia
[10]Engineering Program, Westmont College, 955 La Paz Rd., Santa Barbara, California 93108, USA
[11]School of Mechanical Engineering, Federal University of Uberlândia, Uberlândia 38400-902, Brazil
[12]Department of Engineering and Architecture, University of Udine, Via delle scienze 208, 33100 Udine, Italy

[a)]**Author to whom correspondence should be addressed:** alexandre.fabregat@urv.cat

ABSTRACT

This paper presents and discusses the results of the "2022 International Computational Fluid Dynamics Challenge on violent expiratory events" aimed at assessing the ability of different computational codes and turbulence models to reproduce the flow generated by a rapid prototypical exhalation and the dispersion of the aerosol cloud it produces. Given a common flow configuration, a total of 7 research teams from different countries have performed a total of 11 numerical simulations of the flow dispersion by solving the Unsteady Reynolds Averaged Navier–Stokes (URANS) or using the Large-Eddy Simulations (LES) or hybrid (URANS-LES) techniques. The results of each team have been compared with each other and assessed against a Direct Numerical Simulation (DNS) of the exact same flow. The DNS results are used as reference solution to determine the deviation of each modeling approach. The dispersion of both evaporative and non-evaporative particle clouds has been considered in 12 simulations using URANS and LES. Most of the models predict reasonably well the shape and the horizontal and vertical ranges of the buoyant thermal cloud generated by the warm exhalation into an initially quiescent colder ambient. However, the vertical turbulent mixing is generally underpredicted, especially by the URANS-based simulations, independently of the specific turbulence model used (and only to a lesser extent by LES). In comparison to DNS, both approaches are found to overpredict the horizontal range covered by the small particle cloud that tends to remain afloat within the thermal cloud well after the flow injection has ceased.

Physics of Fluids ARTICLE scitation.org/journal/phf

I. INTRODUCTION

The Coronavirus Disease 2019 (COVID-19) pandemic has revealed the need for a better understanding of the flow physics that govern the airborne transmission of infectious diseases via pathogen-laden aerosols, such as Severe Acute Respiratory Syndrome (SARS), human influenza H1N1, avian influenza (H5N1), and tuberculosis. In response to such a need, Computational Fluid Dynamics (CFD) tools have been massively used to predict the short-term short-range flow and particle dispersion produced by expiratory events to investigate the underlying physical mechanisms and to predict the risk of infection 1 or 2 s after exhalation. Given the complexity of the flow and the huge range of parameters to be explored, expensive Direct Numerical Simulations (DNS) are rarely affordable and Reynolds Averaged Navier–Stokes (RANS)- or Large-Eddy Simulations (LES)-based approaches are most often used. When this is the case, literature results show a significant scattering in the predictions, indicating that no general consensus has been achieved yet on the optimal (if any) modeling approach.

The outbreak of the COVID-19 pandemic in 2020 has dramatically boosted the number of research papers in which CFD is used to investigate aspects of the physical mechanisms of the virus transmission. As an example, a Scopus search conducted at the end of October 2022 for articles with the words "CFD" and "COVID" or "SARS" in the title, in the keyword list, or in the abstract yielded 306 papers with 26 entries in 2020, 99 in 2021, and 141 in 2022. Some of these articles have been collected in special issues, including "Flow and the virus" in Physics of Fluids (2021), "Numerical and experimental investigation of airborne pathogen transmission, and associated heat and mass transfer processes" in International Communications in Heat and Mass Transfer (2021), "COVID-19 and indoor environment" in Indoor Air (COVID-19 and indoor environment, 2022), "Prevention and control of COVID-19 transmission in the indoor environment" in Indoor and Built Environment (Xu and Yu, 2022), or "CFD and COVID-19" in International Journal of Computational Fluid Dynamics (Saad, 2021). It is not the objective of this introduction to exhaustively review the different studies published in the literature so the interested reader is referred directly to these special issues for more details. Also, recent reviews on the role of CFD for modeling aerosol pathogen transmission can be found in Peng *et al.* (2020), Mohamadi and Fazeli (2022), Sheikhnejad *et al.* (2022), and Rayegan *et al.* (2022), among others.

CFD has been used to investigate the flow and the particle dispersion released during expiratory events under different situations and conditions. Simulations of the short-term, short-range dispersion have been conducted to determine the range and shapes of the flow ejection and of the particle cloud a few seconds after the end of an isolated cough or sneeze or after a sequence of violent expiratory events (Abkarian *et al.*, 2020; Diwan *et al.*, 2020; Pendar and Páscoa 2020; Chong *et al.*, 2021; Fabregat *et al.*, 2021a; 2021b; Liu *et al.*, 2021; Trivedi *et al.*, 2021; and Wang *et al.*, 2021). These simulations usually considered the ejection of warm fluid into a quiescent colder ambient and results have been used, first, to establish specific short-term safety distances and, second, to impose initial conditions for long-term simulations of the cloud dispersion within forced or naturally ventilated spaces. Long-term, long-range dispersion in specific indoor ventilated scenarios has been also simulated to investigate the effect of the background air flow on the turbulent dispersion of the aerosol cloud in a wealth of different indoor scenarios, such as classrooms (Foster and Kinzel, 2021; Narayanan and Yang, 2021), hospitals (Arjmandi *et al.*, 2022), offices (Yu *et al.*, 2018; Bhat *et al.*, 2022), halls (Shao and Li, 2020), general ventilated spaces (Zhang *et al.* 2021), cars (Arpino *et al.*, 2022; Mathai *et al.*, 2022), buses (Duchaine *et al.*, 2021; Ho and Binns, 2021; and Zhang *et al.*, 2021), airliner cabins (Yang *et al.*, 2018; Talaat *et al.*, 2021), restaurants (Ho, 2021; Liu *et al.* 2021; and Wu *et al.* 2021), elevators (Dbouk and Drikakis, 2021), and parkings (Nazari *et al.*, 2021).

To simulate aerosol dispersion, DNS, LES, the numerical solution of the Unsteady Reynolds-Averaged Navier–Stokes equations (URANS), and hybrid URANS-LES methods have been used. These three techniques can be understood as three different levels of modeling to simulate turbulent flows. While DNS solves directly for all spatial and temporal scales, LES models the effect of the turbulent scales smaller than the grid on the larger scales that are explicitly solved by the computational grid. URANS-based simulations are based on a higher level of turbulence modeling, since they numerically solve the Unsteady Reynolds Averaged equations with models for the closure terms (Pope, 2000). Although some DNS have been reported in the literature so far (Diwan *et al.*, 2020; Chong *et al.*, 2021; and Fabregat *et al.* 2021a), generally, LES have been preferred for predictions of the short-term dispersion because of the relatively small computational costs it requires (Abkarian *et al.*, 2020; Pendar and Páscoa, 2020; Calmet *et al.*, 2021; Liu *et al.*, 2021; and Wang *et al.* 2021). On the other hand, URANS, and to a lesser extent LES coupled with hybrid methods, has been used to simulate the long-term dispersion, which usually involves larger computational domains and longer simulations times compared to the short-term dispersion.

In this paper, we focus our attention on the effect of the turbulence modeling and of the numerical methods used in the simulations for the prediction of the short-term dispersion of an isolated violent expiratory event. The warm and relatively humid flow ejection into a typically colder and drier ambient usually lasts less than 1 s (Gupta *et al.*, 2009; Tang *et al.*, 2013) and has a maximum Reynolds number of order 10^4 (Bourouiba, 2021). During the flow injection, a new turbulent jet is formed, with a penetration length from the source that scales with time as $t^{1/2}$ (Chaudhuri *et al.*, 2020). When the flow injection ceases, the jet evolves into a turbulent buoyant puff, with a time scaling of $t^{1/4}$ as the turbulence progressively decays (Scorer, 1997). This transient turbulence level is challenging for simulations because many turbulence models for URANS or some subgrid-scale models for LES exhibit a decrease in their performance when dealing with decaying unsteady turbulent flows with buoyancy effects. This is especially true when the flow progressively relaminarizes during the puff stage. Aerosol particles are expelled during the flow injection, and most simulations found in the literature track the particle dispersion following individual evaporating or non-evaporating solid spherical particles by means of Lagrangian methods assuming low particle volume fraction ($\phi \sim 10^{-5}$ Duguid, 1946) and, consequently, neglecting the particle collisions and adopting the one-way coupling between the phases. Coalescence and breakup phenomena are also neglected in almost all the available studies. The rationale behind this choice is that none of these mechanisms is well understood yet for the specific problem of pathogen-laden droplets transported in an ambient air flow (Zhou and Zou, 2021). This implies uncertainty in the modeling and (expected) high variability in the simulated results.

Physics of Fluids ARTICLE scitation.org/journal/phf

The larger inertial particles expelled during the exhalation follow quasi-ballistic trajectories that are almost independent of the flow, whereas small and less inertial particles tend to remain afloat within the wake of the decaying new jet and the frontal puff, even when they are larger than the Kolmogorov scale (Pourfattah *et al.*, 2021). The Lagrangian tracking of these small particles is also challenging when using turbulence or subgrid-scale models because their trajectories are more sensitive to the surrounding flow conditions and to the local velocity. In these cases, random-walk models, tuned according to the local level of turbulence, may be used to account for the effect of the modeled fluctuations on the particle trajectory (Mofakham and Ahmadi, 2020).

The usual grid distribution strategy adopted in the simulations that are reported in the literature concentrates the mesh elements toward the flow inlet and near the growing shear layers of the new jet flow. This strategy produces skewed mesh elements that can affect the convergence of the numerical solution and may reduce its accuracy. Also, the use of a relatively coarse mesh away from the source can influence the dynamics of the frontal puff and the capability of LES to capture the decaying turbulent flow due to excessive filtering. These complex flow features of the spatially and temporally evolving flow associated with a violent expiratory event make the construction of the grid also challenging since one needs to correctly capture the time evolutions of the turbulent intensities in different regions of the flow. The application of Adaptive Mesh Refinement (AMR) techniques can have advantages to capture with enough spatial resolution, flow structures that appear at different times and at different locations along the computational domain. At the same time, however, we remark that AMR may affect the comparison between different simulations, which is what we aim to do in this paper. For example, AMR can make it more difficult to directly identify the limitations of a turbulence model because AMR dynamically adjusts the mesh resolution in different parts of the domain based on the local solution features, thus masking some of the deficiencies of a specific turbulence model. The turbulence model may appear to perform better in some regions of the domain simply because the mesh has been refined in those areas and not because the model is more accurate.

The relevance that the prediction of the risk of transmission of infectious diseases via pathogen-laden aerosols has, together with the complexity of the simulations of the flow and particle dispersion generated in a violent expiratory event, motivated the organization of this international CFD challenge, which was launched in October 2021. The aim of the challenge is to assess the accuracy with which the different modeling approaches can reproduce the dynamics of a prototypical violent expiratory event. In this paper, we compare and analyze the different results submitted by the participants, who used different CFD codes and different turbulence modelization (LES, URANS, and Hybrid), and we summarize the outcomes. In Sec. II, we thus present the framework of the Challenge, and we describe the main characteristics of the codes, meshes, and numerical methods used by the different participants. The results are presented, compared, and discussed in Sec. III, and the final conclusions of the study and recommendations are outlined in Sec. IV.

II. CHALLENGE FRAMEWORK AND PROBLEM DEFINITION

The objective of the challenge, organized by the members of Universitat Rovira i Virgili (Spain) and University of Udine (Italy), is to evaluate the ability of different CFD codes and different turbulence models to reproduce the short-term flow and the particle short-range dispersion that characterizes a prototypical violent expiratory event, which has a duration of 0.4 s (typical of a mild cough expelled in an indoor environment) and is dominated by the inertia of the air injection, such that the dispersion process is assumed to be essentially independent of the background air currents produced by a forced or natural ventilation system. Specifically, the Challenge aims at addressing two tasks: (1) assess the ability of each combination of numerical method and turbulence modeling used for the simulation to reproduce predictions of DNS of the unsteady jet flow of an idealized exhalation event, characterized by the rapid, but limited in time injection of warm air into an initially quiescent ambient (stage I of the Challenge); (2) estimate the impact of the particle size and evaporation on the dispersion of the aerosol cloud, generated in the exhalation event, and compare the results with the predictions obtained combining DNS of the flow with a one-way coupling Lagrangian tracking scheme (stage II of the Challenge). Each team was free to carry out just one or both tasks. However, since the transmission of airborne diseases depends on the dispersion of pathogen-laden particles, the teams were strongly encouraged to address both.

To prevent bias among participants, the challenge was planned as a blind test. The participants had no information about choices made by the other teams before the deadline for the data submission and the file exchange between the participants and the organizers was made through a private Google Drive folder for each team. The DNS data published in Fabregat *et al.* (2021a; 2021b), which were already available prior to the challenge, were suggested as a reference. The data requested had to be sent in ASCII or binary vtk files to facilitate the post-processing and visualization steps, which were performed using the open-source multi-platform ParaView software (Paraview, 2022).

The physical model, the computational domain, and the boundary conditions proposed for the challenge were the same as those used by Fabregat *et al.* (2021a; 2021b). The interested reader is referred to these two publications for information about the specific set of physical parameters selected for the simulation. Figure 1 shows the cylindrical computational domain and the frame of reference. The dimensions of the cylindrical computational domain were $H = 1.60$ and $D = 1.00$ m, and the flow inlet consisted of a cylindrical pipe (mimicking the oral cavity) with axial length $H_p = 0.04$ m and diameter $d = 0.02$ m. The Cartesian coordinate system uses (x, y, z) as the spanwise, vertical, and streamwise directions with the origin located on the symmetry axis and placed at the downstream end of the inlet pipe. Gravity acts in the negative y direction (see Fig. 1).

To facilitate the transition to turbulence, a Gaussian bump of height $H_d = 0.001$ m and width $\sigma = 0.002$ m centered at $z = -0.01$ m was placed inside the inlet pipe (see inset in Fig. 1). The exhalation event was modeled as an unsteady air injection at 34 °C into an initially quiescent environment at 15 °C. The air injection velocity (w) was assumed to be uniform at the inlet circular section and followed a saw tooth profile equal to zero at $t = 0$, then linearly increasing up to a maximum value of $w = 4.8$ m/s at $t = 0.15$ s, and finally linearly decreasing back to $w = 0$ at $t = 0.4$ s. The physical properties of the air were assumed to be constant except for the linear density variation with temperature, which only was taken into account in the vertical momentum equation, according to the Boussinesq approximation. The values for viscosity, density, thermal conductivity, heat capacity,

Physics of Fluids ARTICLE scitation.org/journal/phf

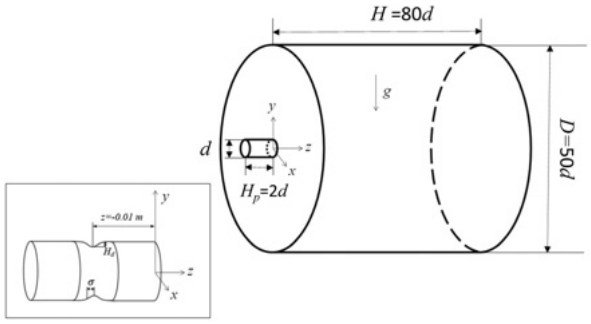

FIG. 1. Physical model and the system of reference. The inset shows a zoom of the inlet. Outflow boundary conditions are imposed at the far field z = H and at the large cylindrical surface.

and the thermal expansion coefficient were, respectively, $\mu = 1.95 \times 10^{-5}$ Pa s, $\rho_0 = 1.22$ kg/m^3, $k = 0.0277$ W/m K, $Cp = 1010$ J/kg K, and $\beta = 3.36 \times 10^{-3}$ K^{-1}. The constant pressure or outflow boundary conditions were prescribed at the far field exit ($z = H$) and at the lateral cylindrical surface $(D/2)^2 = x^2 + y^2$ for $0 < z < H$. At the surface $z = 0$, $(D/2)^2 > x^2 + y^2 > (d/2)^2$ and at the cylindrical inlet pipe wall, non-slip boundary conditions had to be used. Uniform Dirichlet boundary conditions were imposed at the pipe inlet ($z = -H_d$) according to the time evolution of the air injection velocity described above. This yields $u = 0$, $v = 0$, and $w = w(t)$. All the boundary surfaces were assumed to be adiabatic except for the circular inlet where a constant uniform Dirichlet condition for the temperature, namely, $T = 34\,^\circ$C, had to be prescribed. Each team was free to select the boundary values for the relevant turbulence quantities at the circular inlet. The physical time covered by the simulations was also prescribed and set equal to $t = 1.60$ s.

For stage II, we considered seven different spherical particle diameters: 4, 8, 16, 32, 64, 128, and 256 μm. Particles had to be released continuously at the inlet with the same velocity of the surrounding fluid over the entire duration of the exhalation ($t \leq 0.4$ s). Each team was free to decide how to model the evaporation of the aqueous fraction of the particles. If included, the minimum allowable diameter due to evaporation had to be one-third of the initial value, as in Fabregat *et al.* (2021b). This corresponds to evaporating droplets laden with a 3% volume fraction of nonvolatile matter (Wang *et al.*, 2021). Exhaled and ambient air relative humidities were taken as 85% and 65%, respectively. The physical properties of the particles were assumed to be those of water at ambient temperature ($\rho_p = 1000$ kg/m^3, $k_p = 0.606$ W/m K, $Cp_p = 4180$ J/kg K), whereas a value $\Delta H_v = 2.257 \times 10^6$ J/kg was selected for the enthalpy of evaporation.

The deliverables for stage I were vtk files, which are readable with ParaView (2022), with 2D instantaneous scalar fields on the symmetry plane $x = 0$ at three different times: at $t = 0.25$ s, during the exhalation, at $t = 0.40$ s, corresponding to the end of the flow injection and at $t = 1.50$ s, about 1 s after the exhalation. Each file contained the temperature (°C), the axial (horizontal) velocity component (m/s), and the vertical velocity component (m/s).

For stage II, each team was requested to submit seven ASCII files, one for each particle size with the time evolutions of the position of the centroid of the particle cloud and the sizes of the cloud, for a total of five columns of data: time (s), z coordinate of the particle cloud centroid (c_z), y coordinate of the particle cloud centroid (c_y), streamwise width of the particle cloud (σ_z), and vertical width (σ_y) of the particle cloud. The coordinates of the centroid and the widths of the cloud are defined as follows:

$$c_y = \frac{\sum_{i=1}^{n} y_i}{n}, \quad c_z = \frac{\sum_{i=1}^{n} z_i}{n} \tag{1}$$

and

$$\sigma_y = \sqrt{\frac{\sum_{i=1}^{n} (y_i - c_y)^2}{n}}, \quad \sigma_z = \sqrt{\frac{\sum_{i=1}^{n} (z_i - c_z)^2}{n}} \tag{2}$$

with n the total number of tracked particles for a given diameter.

An international call for participation in the Challenge was released in October 2021, and initially 16 teams from around the world showed interest and asked for information about the instructions to contribute. Six months later at the deadline for data submission (May 1, 2022), seven teams submitted the requested results. The results obtained by each team were presented and discussed during an online workshop held on June 27, 2022. Table I shows, in alphabetical order, the list of teams that submitted a complete set of data for stage I, and their country of origin.

In total, 11 different simulations were submitted for stage I. Table II summarizes the list of teams, in random order, and the details of their simulations. Each simulation is identified by an alphanumeric code, reported in the last column of Table II. This code classifies each team with a randomly assigned letter (A–G) followed by an integer representing the simulations performed by that team (the integer is increased in the case of multiple simulations by a single team) and a further letter: U for a URANS-based simulation, L, for LES or H, for hybrid URANS-LES method. Finally, a Roman numeral is used to indicate the stage the simulation refers to (I or II).

Table II shows that three teams performed the simulations with commercial codes: two teams (A and D) with Ansys Fluent and one team (F) with STAR-CCM+. The open-source OpenFOAM solver was used by two teams (C and G), whereas the two remaining teams (B and E) used their own in-house codes. Note that team B considered the low-Mach version of the transport equations (Le Quéré *et al.*, 2005) without

TABLE I. Affiliation of the participating teams. Alphabetical order.

Barcelona Supercomputing Center	Spain
Westmont College-Federal University of Uberlândia	USA-Brazil
Otto von Guericke Universität Magdeburg	Germany
Peter the Great St. Petersburg Polytechnic University	Russia
RMIT University-The University of Sydney	Australia
Universitat Politècnica de Catalunya	Spain
University of Maribor-University of Erlangen Nuremberg	Slovenia-Germany

Physics of Fluids ARTICLE scitation.org/journal/phf

TABLE II. Stage I: Summary of the simulations' details.

Team	Code	Turbulence	Spatial discretization	Temporal discretization	Grid	Boundary conditions	Code
A	Ansys Fluent v19.3 (Ansys Inc., 2022)	URANS k-ε	Finite volume, second order	Implicit, second order, $\Delta t = 10^{-5}$ s	0.6×10^6 hexahedral	Turbulence intensity 5% Turbulent viscosity ratio 10	A1-U-I
		URANS k-ε RNG					A2-U-I
		URANS k-ω SST					A3-U-I
		LES WMLES S-Ω ($Pr_t = 0.85$)			35×10^6 polyhedral	Vortex method	A4-L-I
B	Alya-HPC mechanics (Vázquez *et al.*, 2016)	LES of low-Mach equations (Vreman, 2004) ($Pr_t = 0.7$)	Finite element, second order	Explicit. $\Delta t = 4.4 \times 10^{-6}$ s	46×10^6 tetrahedral/ prism	Laminar inlet	B1-L-I
C	OpenFOAM v8 and v9 (OpenFoam, 2022)	URANS: k- ω SST	Finite volume, second order	Adaptative $3.5 \times 10^{-4} \leq \Delta t \leq 2\ 10^{-3}$ s	6.2×10^6 hexahedral ($792 \times 243 \times 36$)[a]	$k = 0.0864\ m^2/s^2$ $\omega = 387\ s^{-1}$	C1-U-I
D	Ansys Fluent v2021R2 (Ansys Inc., 2022)	Hybrid: SBES, SST-LES with WALE	Finite volume, second order	Bounded second order implicit. $\Delta t = 10^{-5}$ s for $t < 0.8$ s $10^{-5} \leq \Delta t \leq 10^{-4}$ s for $t > 0.8$ s	20×10^6 poly-hexcore	Turbulence intensity 5% Turbulent viscosity ratio 10	D1-H-I
E	UNSCYFL3D (Fontes *et al.*, 2019)	URANS two-layer k-ε	Finite volume, second order	Implicit, second order $\Delta t = 5 \times 10^{-4}$ s	0.68×10^6 hexahedral ($120 \times 110 \times 52$)[a]	$k = 10^{-8}\ m^2/s^2$ $\varepsilon = 10^{-8}\ m^2/s^3$	E1-U-I
F	STAR-CCM+ 2020.1 and 2021.3 (Siemens, 2022)	URANS: SST k-ω model	Finite volume, second order	Second order implicit, $\Delta t = 10^{-3}$ s	1.6×10^6 hexahedral ($366 \times 120 \times 56$)[a]	Turbulence intensity 1% Turbulent viscosity ratio 10	F1-U-I
		LES: WALE model ($Pr_t = 0.9$)		PISO unsteady. $\Delta t = 10^{-5}$ s	14.2×10^6 hexahedral ($602 \times 274 \times 136$)[a]	Laminar inlet	F2-L-I
G	OpenFOAM v7 (OpenFoam, 2022)	Hybrid: k-ω-SST DES	Finite volume, second order	Implicit, $6 \times 10^{-6} \leq \Delta t \leq 6 \times 10^{-4}$ s	30×10^6 hexahedra, polyhedra	Variable turbulence intensity and k as a function of the inlet Re number	G1-H-I

[a]Number of elements: axial × radial × angular.

Physics of Fluids ARTICLE scitation.org/journal/phf

the buoyancy term in the vertical momentum equations. All the simulations were carried out with second-order finite volume codes, except for those of team B, which used a code based on a second-order finite element technique for spatial discretization. Of the 11 simulations, 6 were based on the numerical solution of the URANS equations, 3 used the LES technique, and 2 used a URANS-LES hybrid methods. It should be noted that for the physical model considered in the Challenge, the role of the URANS in these hybrid methods is limited to the region near the non-slip wall of the cylindrical inlet with the Gaussian bump (see Fig. 1). Most of the teams performed the time-marching procedure with implicit schemes and the time-steps used for the URANS-based simulations ranged approximately from 10^{-3} s to 10^{-5} s, while the LES and hybrid URANS-LES simulations were carried out with time steps in the range 10^{-5}–10^{-6} s. Participants were asked to select the mesh resolution according to a test of grid independence. The resulting grids were preferably constituted by hexahedra and polyhedral volumes. URANS-based simulations were carried out with a number of grid elements ranging from 0.6×10^6 to 6.2×10^6, while the number of elements for LES and hybrid methods ranged from 14.2×10^6 to 46×10^6 elements.

Five teams submitted the requested data for stage II and the details of the Lagrangian tracking methods used by each team are indicated in Table III, together with the identifying code assigned to each simulation. For stage II, the code's last integer indicates if evaporation is (1) or is not (0) accounted for. As can be seen from Table III, evaporation was considered in 3 simulations out of a total of 12 simulations of the particle dispersion submitted under different conditions. In seven of these simulations, the flow was computed by solving the URANS equations while there are three simulations in which LES was used and only one was run using a hybrid method. All the teams presented results for the seven selected particle diameters. Particle tracking was performed considering a force balance that included the drag force, the gravity and buoyancy forces, and a turbulent dispersion force or a subgrid-scale random walk for URANS or LES, respectively.

III. RESULTS AND DISCUSSION

In this section we present, compare and discuss the results obtained by the teams, starting from stage I (jet flow) in Subsections III A and III B and ending with stage II (particles) in Subsection III C.

A. Instantaneous thermal and velocity fields (stage I)

The teams submitted the instantaneous thermal and velocity fields in the symmetry plane $x = 0$ at three different times ($t = 0.25$, $t = 0.4$, and $t = 1.5$ s). We recall that the prototypical exhalation prescribed as inlet flow reaches the maximum velocity at $t = 0.15$ and ends at 0.4 s (see Sec. II). We grouped the results provided by the teams using URANS in Figs. 2 and 3, and the results provided by either LES or hybrid methods in Figs. 4 and 5. Figures 2 and 4 show the non-dimensional temperature contours, whereas Figs. 3 and 5 show the contours of the axial (z) component of the velocity vector in physical units. The non-dimensional temperature is defined as $\theta = (T - T_o)/(T_i - T_o)$, where T_i is the temperature of the flow at injection ($T_i = 34\,^\circ$C) and T_o is the background temperature ($T_o = 15\,^\circ$C). This yields $\theta = 0$ at the far-field and $\theta = 1$ at the flow

TABLE III. Stage II: Summary of the simulations' details.

Team	Turbulence	Evaporation	Forces	Number of particles	Numerical method	Code
A	URANS	No	Drag, gravity, discrete random walk model	13 800 for each diameter	Lagrangian tracking Runge–Kutta method	A1-U-II-0
						A2-U-II-0
						A3-U-II-0
	LES			Diameters: 4, 8, 16, 32, 64, 128, and 256 μm		A4-L-II-0
C	URANS	No	Drag, gravity, turbulent dispersion (stochasticDispersionRAS)	13 800 for each diameter	Lagrangian tracking. Euler implicit.	C1-U-II-0
				Diameters: 4, 8, 16, 32, 64, 128, and 256 μm released in half of the inlet cross section	Interpolation method: Linear weighted interpolation using cell values.	
E	URANS	No	Drag, gravity, turbulence dispersion force	5600 for each diameter Diameters: 4, 8, 16, 32, 64, 128, and 256 μm	Lagrangian tracking scheme: Analytical scheme, interpolation method for fluid velocity: Second order	E1-U-II-0
F	URANS	No	Drag, gravity, turbulence dispersion force	13 800 for each diameter	Lagrangian tracking.	F1-U-II-0
		Yes		Diameters: 4, 8, 16, 32, 64, 128, and 256 μm released at x = 0, y = 0, and z = 0.	Second order tracking integration and interpolation.	F1-U-II-1
	LES	No				F2-L-II-0
		Yes				F2-L-II-1
G	Hybrid URANS-LES	No	Drag, gravity, turbulent dispersion (stochasticDispersionRAS)	27 738 for each diameter	Lagrangian tracking. Euler implicit.	G1-H-II-0
		Yes		Diameters: 4, 8, 16, 32, 64, 128, and 256 μm	Interpolation method: Linear weighted interpolation using cell values.	G1-H-II-1

Physics of Fluids ARTICLE scitation.org/journal/phf

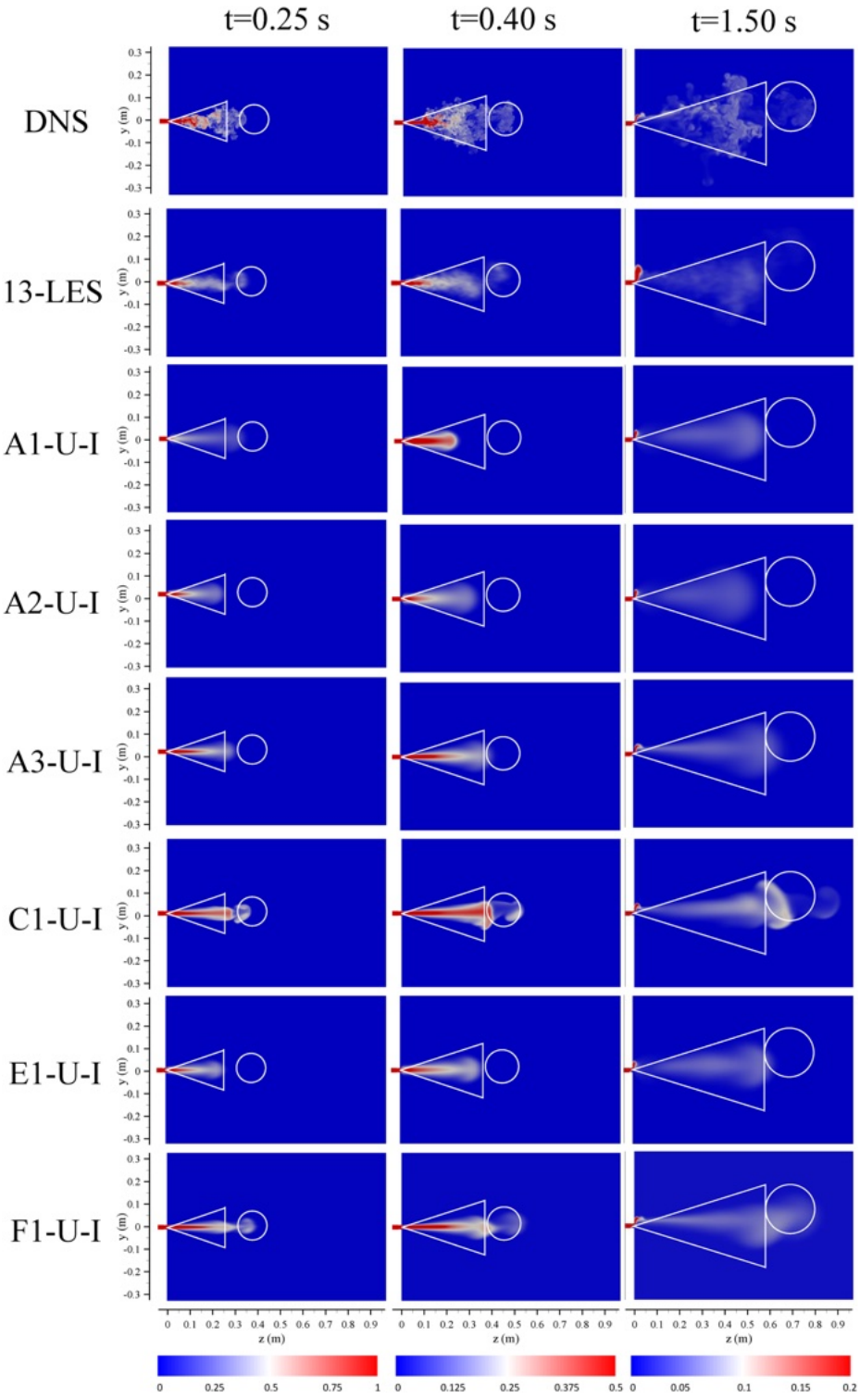

FIG. 2. Contours of instantaneous non-dimensional temperature at $t = 0.25$, $t = 0.4$, and $t = 1.5$ s for the URANS simulations. The predictions of the DNS and the ensemble average of the 13 LES are included at the top of the figure for comparison purposes.

Physics of Fluids ARTICLE scitation.org/journal/phf

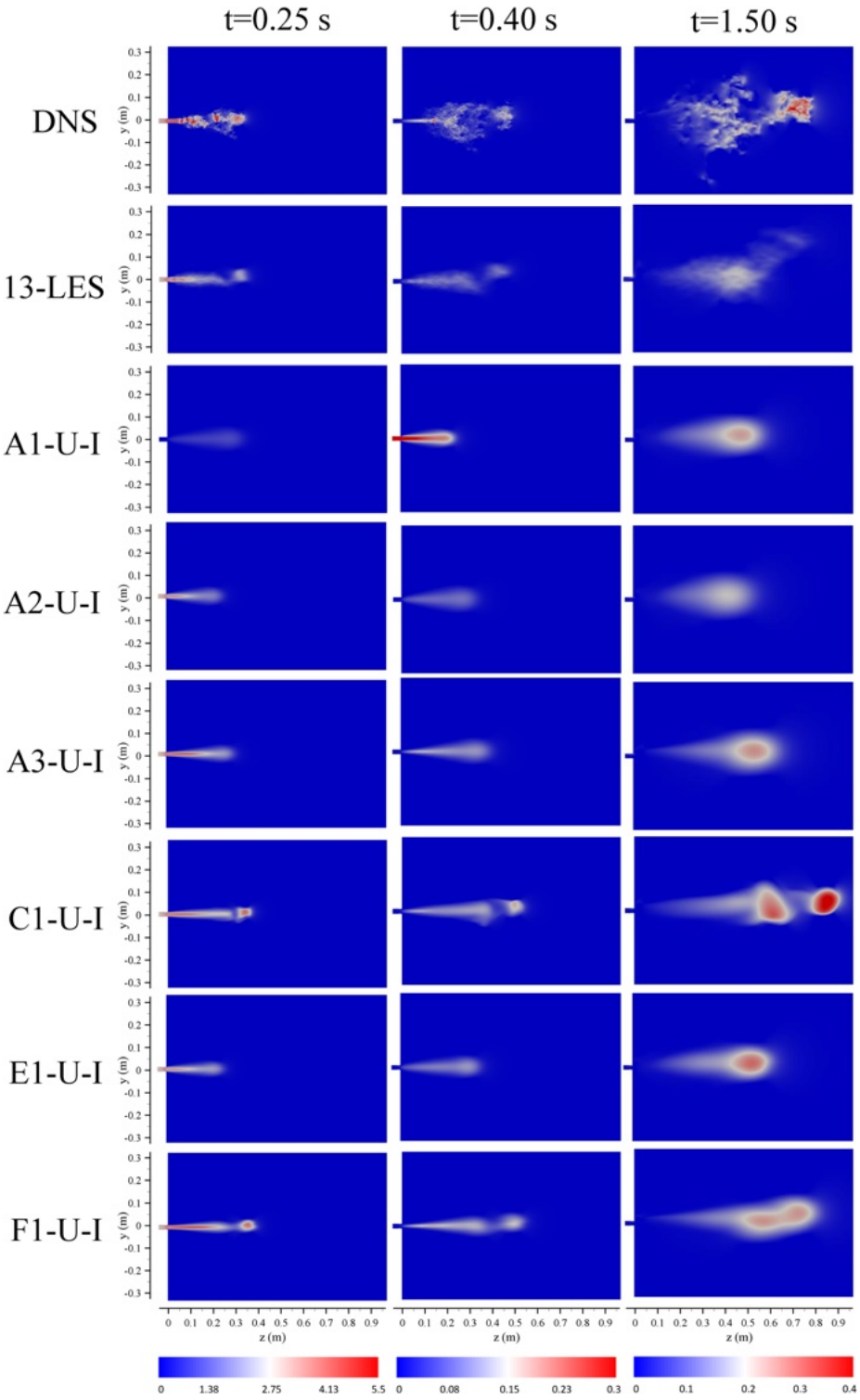

FIG. 3. Contours of instantaneous axial component of the velocity vector (m/s) at $t =$ 0.25, $t =$ 0.4, and $t =$ 1.5 s for the URANS simulations. The predictions of the DNS and the ensemble average of the 13 LES are included at the top of the figure for comparison purposes. Note that the velocity scale is different for the three times.

Physics of Fluids ARTICLE scitation.org/journal/phf

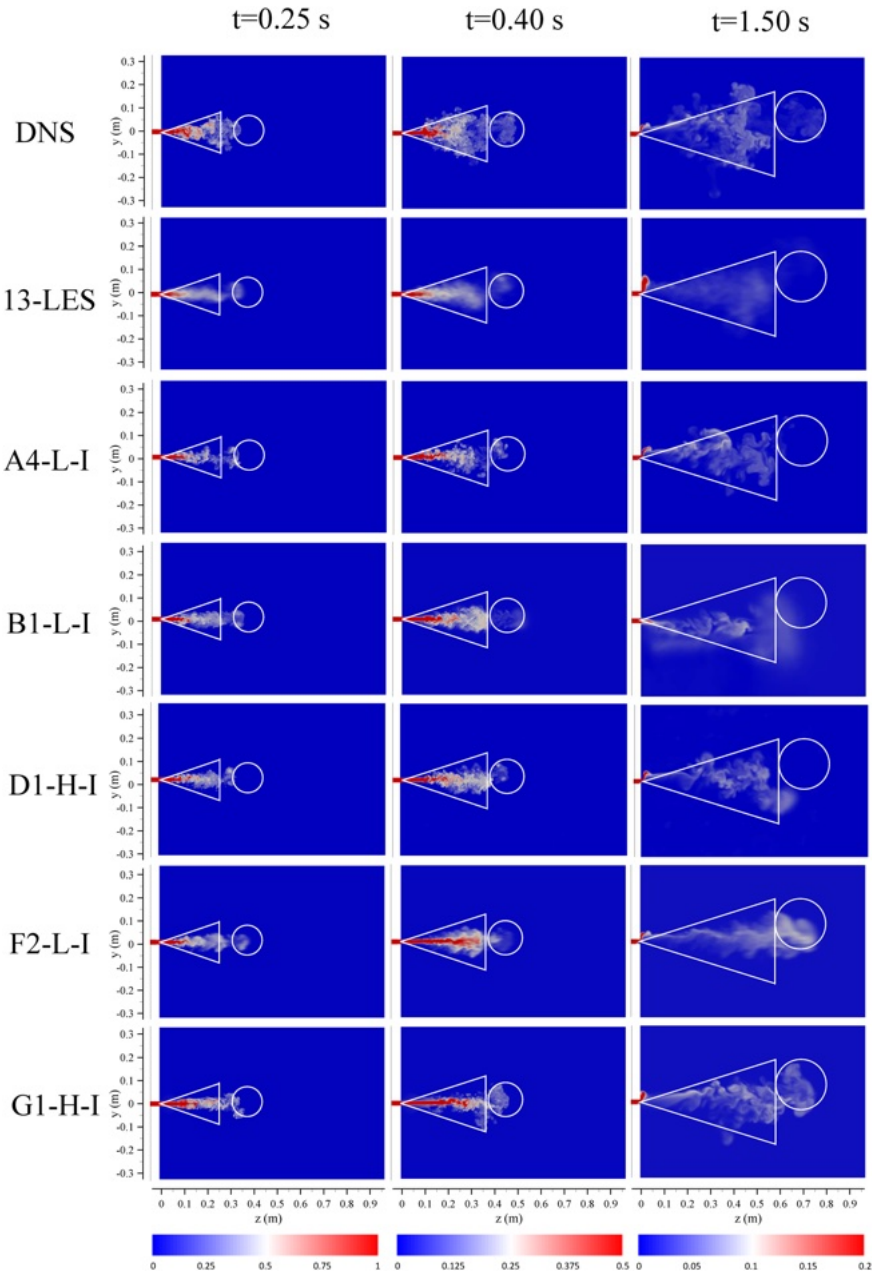

FIG. 4. Contours of instantaneous non-dimensional temperature at $t =$ 0.25, $t =$ 0.4, and $t =$ 1.5 s for the LES and hybrid simulations. The predictions of the DNS and the average of the 13 LES are included in the first and second top rows of the figure for comparison purposes.

inlet. The code used to identify each simulation, indicated in the last column of Table II, is shown to the left of the panels of Figs. 2–4.

A DNS or LES of a given turbulent flow represents a single realization of the flow, and the variability between the instantaneous fields of different realizations can be determined by performing different simulations with slightly different boundary conditions (Trivedi *et al.*, 2021). In the panels in the second row of Figs. 2–5, we included, for comparison purposes, the average temperature and axial velocity contours of 13 independent LES of the flow carried out by the organizers with different inlet velocity boundary conditions. In these 13 LES, only the flow dispersion was simulated. The details of these simulations are described in the Appendix. The average temperature and axial velocity contours can be compared directly with the corresponding fields predicted by the URANS simulations, shown in Figs. 2 and 3, because the

Physics of Fluids ARTICLE scitation.org/journal/phf

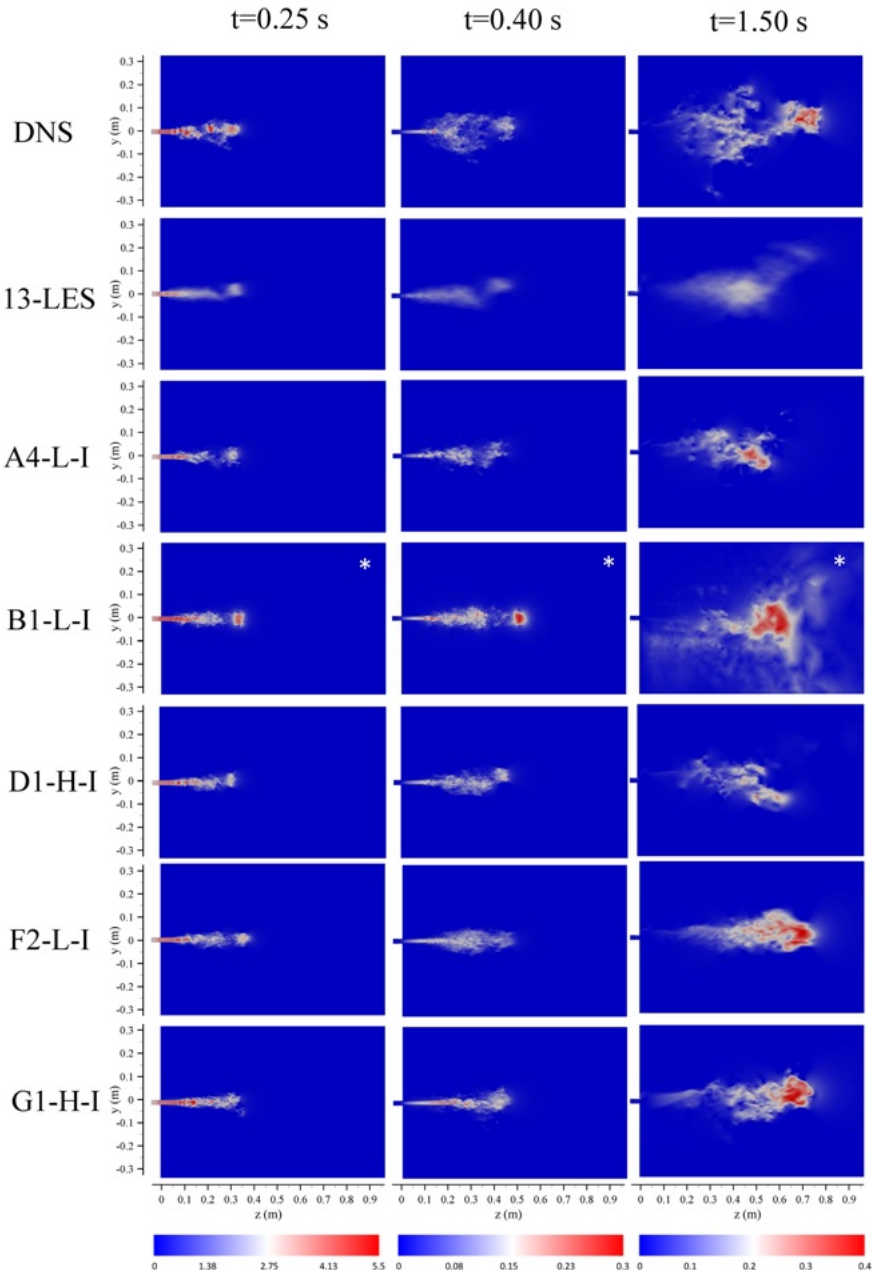

FIG. 5. Contours of instantaneous axial component of the velocity vector (m/s) at $t = 0.25$, $t = 0.4$, and $t = 1.5$ s for the LES and hybrid simulations. Note that the velocity scale is different for the three times. The predictions of the DNS and the average of the 13 LES are included in the first and second top rows of the figure for comparison purposes. (*) The plots corresponding to team B show the modulus of the velocity vector.

URANS predictions can be considered as equivalent to the ensemble averaged fields of many different flow realizations. This allows to estimate the variability of the different realizations of the same turbulent flow. In all the figures, the instantaneous contours of the DNS reported by Fabregat *et al.* (2021a) are included on the top row for comparison purposes.

The theoretical shapes of the envelope of the thermal cloud, estimated using the models of Scorer (1997) and Richards (1968), and applied to violent expiratory events in Pallares and Fabregat (2022), have been superimposed to the temperature contours in Figs. 2 and 4. The model developed by Scorer (1997) to obtain the time-evolution of the front of the new jet predicts an envelope with a quasi-conical shape with an elliptical cross section. At the plane $x = 0$, the contour of the envelope corresponds to the white triangular shape shown in Figs. 2 and 4. The position and radius of the frontal spherical thermal puff

Physics of Fluids ARTICLE scitation.org/journal/phf

(Richards, 1968) is indicated in these figures with a white circle. The theoretical triangular and circular envelopes frame well the instantaneous thermal puff of the DNS shown in the top three panels of Fig. 2, especially for $t = 0.4$ and $t = 1.5$ s. Note that the flow injection, that lasts up to 0.4 s, is still active at $t = 0.25$ s, and the frontal quasi-spherical puff, completely formed only when the flow injection ceases, is not fully developed.

The six predictions of the thermal cloud by the URANS-based simulations at $t = 0.25$, 0.5, and 1.5 s are shown in Fig. 2. Note that the vertical dispersion of the jet obtained with these simulations is smaller than the theoretical one, indicated by the triangular shapes, and the one predicted by the DNS. The positions of the frontal quasi-spherical thermal puff at $t = 0.4$ s and $t = 1.5$ s are very well captured by the simulations C1-U-I and F1-U-I, while the other simulations (A1-U-I, A2-U-I, A3-U-I, and E1-U-I) underpredict to some extent the range and the vertical displacement of the frontal thermal puff. The reason for these improved predictions of the thermal puff dynamics has to do mainly with the grid resolution: The C1-U-I and F1-U-I simulations were run on meshes of 6.2×10^6 and 1.6×10^6 elements, respectively, whereas the A1-U-I, A2-U-I, A3-U-I, and E1-U-I simulations used coarser meshes of about 0.6×10^6 elements. Comparing the predictions of simulations A3-U-I and C1-U-I, both carried out with the k-ω-SST model against the predictions of simulations A1-U-I and A2-U-I, carried out with k-ε models (see Table II), it can be seen that the specific turbulence model has a very limited impact on the prediction of the position and extension of the frontal thermal puff. Similar conclusions can be obtained by comparing the predictions of the axial velocity component plotted in Fig. 3. In this case, simulations performed with finer meshes (C1-U-I and F1-U-I) better reproduce the range of DNS instantaneous velocity contours, which are characterized by higher vertical dispersion when compared to URANS simulations. It is also remarkable that simulation F1-U-I shows a frontal region of high velocity that is detached from the thermal cloud and is qualitatively similar to that found in the DNS (see Fig. 3).

We also remark here that the instantaneous axial velocity was not reported by team B (B1-L-I); therefore, Fig. 5 shows the modulus of the instantaneous velocity for this team. At $t = 0.25$ and $t = 0.4$ s, all the LES show very similar temperature and velocity contours. As for the URANS-based simulations (cases A1-U-I to F1-U-I in Figs. 2 and 3), it is evident that the vertical dispersion of the jet is slightly underestimated with respect to the DNS, but both the range and the extension of the frontal thermal puff are well reproduced in all the cases. At $t = 1.5$ s, simulations F2-L-I and G1-H-I exhibit intense velocity activity in the frontal thermal puff, as observed in DNS too (see Fig. 5). This can be also appreciated in Fig. 4, where the range of the thermal cloud of these two simulations appears larger than the LES range. The comparison of the characteristics of these two simulations with those of the remaining simulations shown in Table II does not reveal a clear reason for this difference in terms of mesh resolution, inlet velocity conditions, or SGS model. It can be probably attributed to the stochasticity of the different realizations of the same turbulent flow. In fact, Trivedi *et al.* (2021) reported a relatively large variability in the range of the thermal cloud in different realizations (see, for example, Fig. 2 of Trivedi *et al.*, 2021). Also, as it will be shown in Subsection III B, the variability found in the horizontal range of the thermal cloud at $t = 1.5$ s among the different LES shown in Fig. 4 is compatible with the values of the horizontal size of the thermal cloud of the 13 independent LES.

B. Position and size of the thermal cloud (stage I)

Similarly to the definitions of the position of the centroid and sizes of the particle clouds, given by Eqs. (1) and (2), the position of the centroid (provided by the coordinates c_{Ty}, c_{Tz}) and size (provided by the widths σ_{Ty}, σ_{Tz}) of the thermal cloud can be defined as

$$c_{Ty} = \frac{\int_V y\theta\, dV}{\int_V \theta\, dV}, \quad c_{Tz} = \frac{\int_V z\theta\, dV}{\int_V \theta\, dV} \tag{3}$$

and

$$\sigma_{Ty} = \sqrt{\frac{\int_V (y - c_{Ty})^2 \theta\, dV}{\int_V \theta\, dV}}, \quad \sigma_{Tz} = \sqrt{\frac{\int_V (z - c_{Tz})^2 \theta\, dV}{\int_V \theta\, dV}}. \tag{4}$$

Figures 6 and 7 show, respectively, the predictions of the vertical (y) and axial (z) locations of the centroid of the thermal cloud at $t = 0.25$, $t = 0.4$, and $t = 1.5$ s. The triangles in these figures indicate the vertical and horizontal extensions of the cloud as the position of the centroid plus-minus the corresponding width ($c_{Ty} \pm \sigma_{Ty}$ and $c_{Tz} \pm \sigma_{Tz}$), whereas the circles indicate the locations of the centroids. The predictions of the DNS and those of the averaged 13 LES are shown with lines. The gray regions in Figs. 6 and 7 mark the variability of the 13 LES within two times the standard deviation of the position of the centroid of the thermal cloud. The variability of the dimensions of the cloud is also indicated with shaded regions. According to this, 95% of the different instantaneous positions and sizes of the thermal cloud resulting from different realizations of the same turbulent flow should fall in these shaded areas. It should be noted that this variability only applies to LES since the solution of the URANS equations directly gives the ensemble-averaged flow and temperature fields, corresponding to a large number of different realizations of the flow.

As shown in Figs. 6(a) ($t = 0.25$) and 6(b) ($t = 0.4$ s), the center location and the size of the thermal cloud are mostly well predicted by the LES and URANS-based simulations. At larger times [Fig. 6(c)], the uncertainty of the predictions increases. For the three times considered, the vertical location of the centroid resulting from the URANS-based simulations, plotted with red symbols at the bottom of the panels, agrees well with those of the DNS and the 13 LES, but the widths of the thermal cloud are underpredicted especially at $t = 1.50$ s. At this time, the variability of the vertical sizes of the thermal cloud, defined as $2\sigma_{Ty}$, is relatively small among the URANS predictions, which ranges between 0.07 (A1-U-I) and 0.08 m (C1-U-I). These values are about 50% smaller than those corresponding to the DNS (0.15) and the 13 LES (0.12 m), indicating a reduced turbulent vertical mixing due to the use of turbulence models in the URANS simulations. In these cases, the effect of buoyancy in the transport equations of the turbulent kinetic energy and of the dissipation is to enhance/suppress turbulence in unstable/stable stratified regions of the flow. However, it is known that these models show some deficiencies in the predictions of the spread rates of vertical plumes (Kuma and Dewan, 2014) and buoyant horizontal jets (Alfaifi *et al.*, 2019).

Physics of Fluids ARTICLE scitation.org/journal/phf

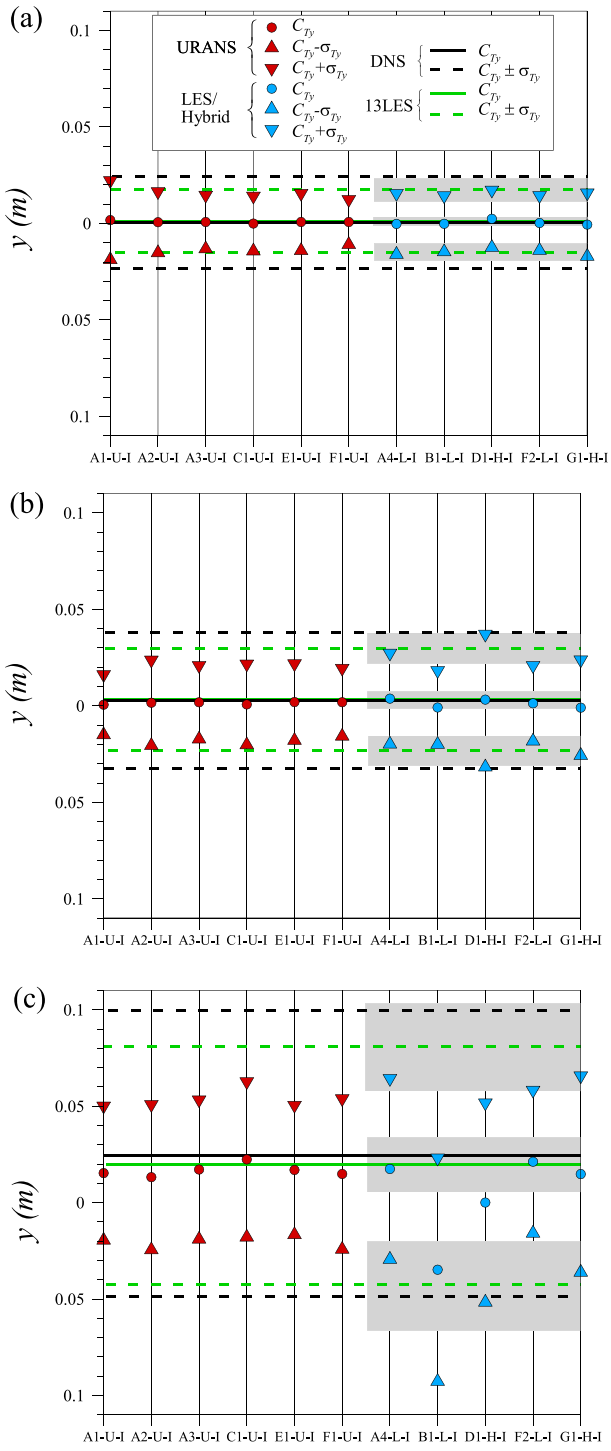

FIG. 6. Vertical positions of the centroid [c_{Ty}, see Eq. (3)] and vertical sizes [σ_{Ty}, see Eq. (4)] of the thermal cloud at (a) $t = 0.25$, (b) $t = 0.4$, and (c) $t = 1.50$ s.

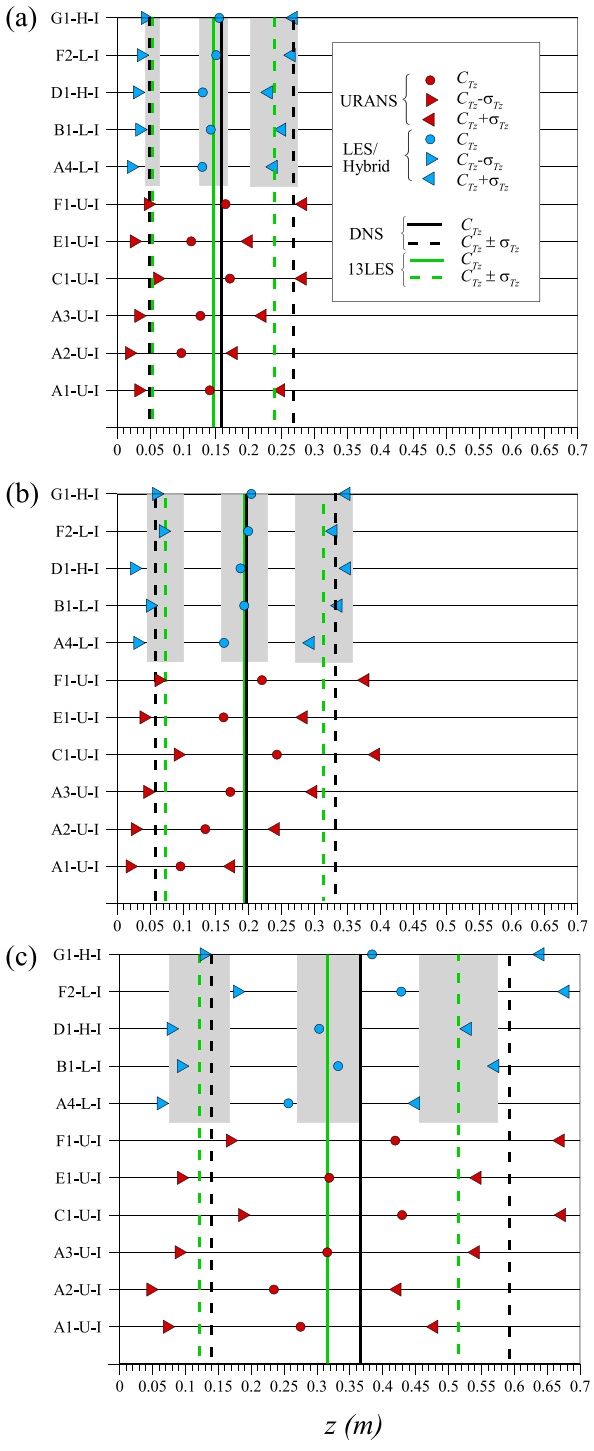

FIG. 7. Axial positions of the centroid [c_{Tz}, see Eq. (3)] and horizontal sizes [σ_{Tz}, see Eq. (4)] of the thermal cloud at (a) $t = 0.25$, (b) $t = 0.4$, and (c) $t = 1.50$ s.

Physics of Fluids ARTICLE scitation.org/journal/phf

The position of the centroid of the thermal cloud predicted by LES, plotted at the top of the panels of Fig. 6 with blue symbols, falls within the variability of the 13 LES for $t = 0.25$ s [Fig. 6(a)] and $t = 0.4$ s [Fig. 6(b)]. At $t = 1.5$ s, there are two simulations (B1-L-I and D1-H-I) that predict vertical positions of the centroid below $y = 0$. The inspection of the instantaneous temperature distribution provided by the simulation B1-L-I at $t = 1.5$ s (Fig. 4) shows that the hot ascending plume near the coordinates origin, formed by the hot fluid remaining in the inlet pipe after the flow injection has ceased, is not reproduced in this case. Also, it can be seen that, at $t = 1.5$ s, the temperature distribution is in fact shifted toward $y < 0$, because, in this simulation, the buoyancy term was not considered in the vertical momentum equation. Although not as pronounced, the instantaneous distribution of the simulation D1-H-I also shows this shift. In this case, the position of the centroid and the vertical size of the thermal cloud are within or very close to the variability of the 13 LES. Figure 6(c) shows that the other LES (A4-L-I, F2-L-I and G1-H-I) predict vertical sizes of the thermal cloud that fall within the variability of the 13 LES.

The axial positions and the horizontal sizes of the thermal cloud are plotted in Fig. 7. In general, the URANS-based simulations, shown in the bottom portion of each panel, predict smaller axial ranges of the thermal cloud (i.e., larger horizontal positions of the centroid) when performed with finer meshes (C1-U-I and F1-U-I, see Table II), as

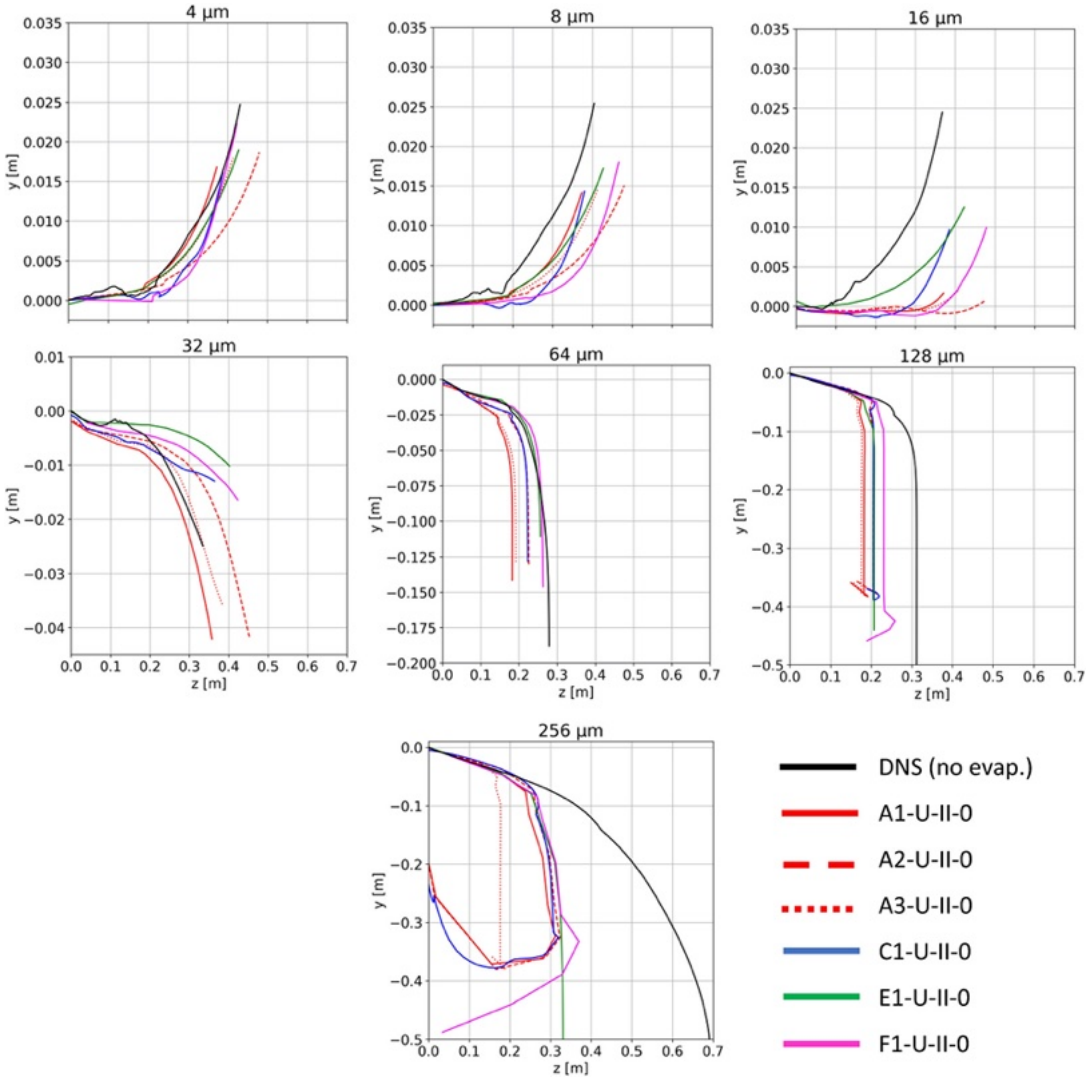

FIG. 8. Trajectories of non-evaporative particle clouds predicted by the URANS-based simulations.

Physics of Fluids ARTICLE scitation.org/journal/phf

compared to coarser simulations (A1-U-I, A2-U-I, A3-U-I, and E1-U-I) at the three times considered. At $t = 1.5$ s [Fig. 7(c)], the variability of the horizontal position of the centroid for the URANS-based simulations lays between 0.24 (A2-U-I) and 0.42 m (C1-U-I) with the predictions of the DNS, yielding $c_{Tz} = 0.36$ m and the 13 LES, yielding $c_{Tz} = 0.32$ m. The horizontal extension, defined as $2\sigma_{Tz}$, ranges between 0.5 (F1-U-I) and 0.38 m (A2-U-I) with that of the DNS being 0.45 m and that of the 13 LES being 0.39 m. This indicates that, in general, at large times, the horizontal size of the thermal cloud is well captured by the URANS-based simulations, while a large scatter is observed in the prediction of the horizontal position of the centroid. This scatter depends on the combination of the grid resolution and the turbulence model used. The results suggest that, regardless of the turbulence model used (see Table II), finer meshes allow the thermal cloud to extend over each larger horizontal distances.

The estimations of the position and sizes of the thermal cloud produced by LES are plotted using blue symbols at the top of the panels of Fig. 7. At $t = 0.25$ [Fig. 7(a)] and $t = 0.4$ s [Fig. 7(b)], the predictions lay close or within the variability of the 13 LES, which is indicated by the gray areas. At larger times [$t = 1.5$ s, Fig. 7(c)], the different LES exhibit larger variability in terms of the centroid position and horizontal sizes of the thermal cloud. The horizontal extensions range between 0.39 (A4-L-I) and 0.51 m (G1-H-I). These values compare well with DNS, which yields $2\sigma_{Tz} = 0.45$ m and the 13 LES, which yield $2\sigma_{Tz} = 0.39$ m. The centroid position exhibits a significant larger variability, but its predictions are anyway close to those of DNS

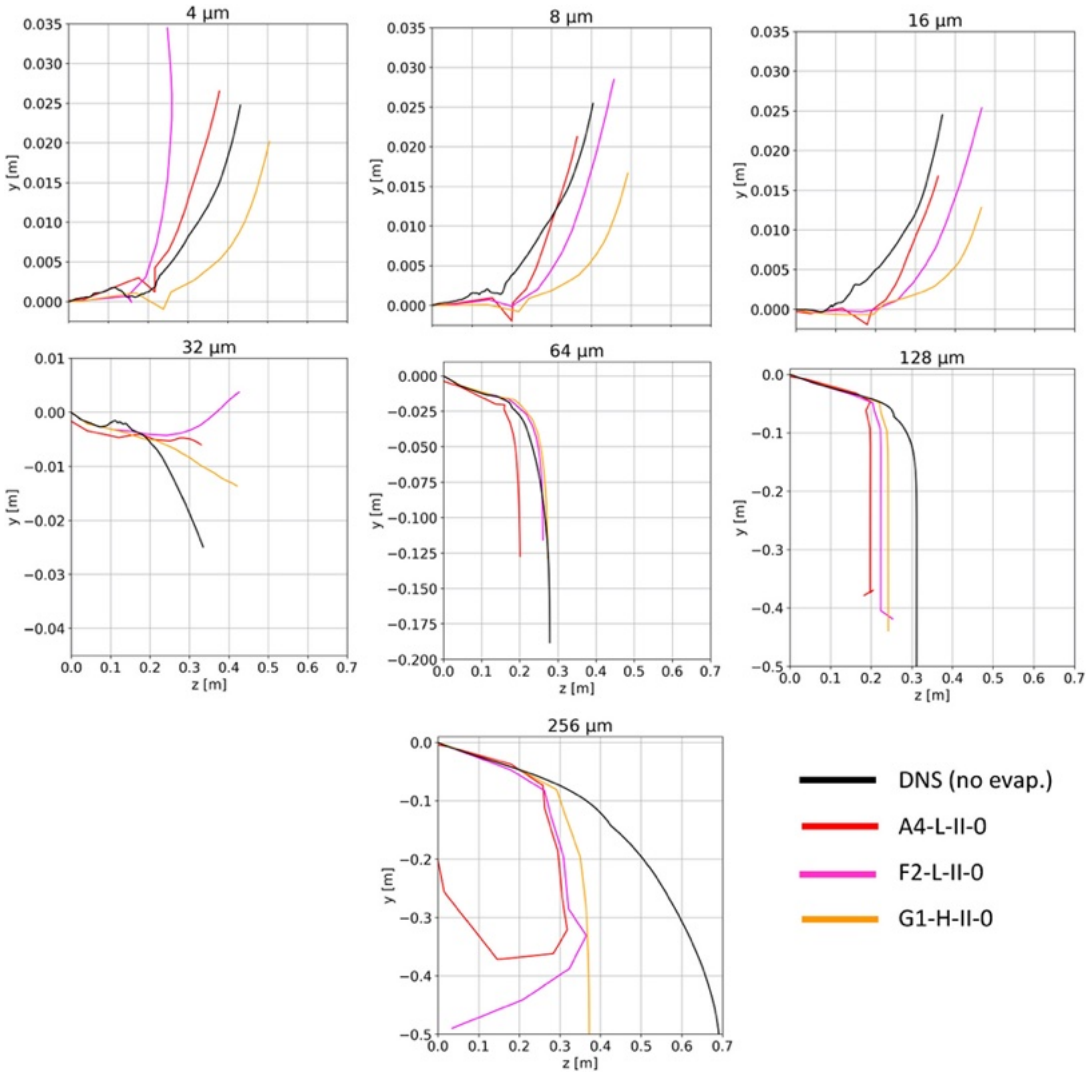

FIG. 9. Trajectories of non-evaporative particle clouds predicted by LES.

Physics of Fluids ARTICLE scitation.org/journal/phf

and the 13 LES, especially for simulations D1-H-I and B1-L-I, which lay within the variability of the 13 LES, indicated with gray areas in Fig. 7(c). According to the information shown in Table II, these differences in the axial position of the centroid of the thermal cloud at $t = 1.5$ s can be attributed to the inherent variability of different realizations of the same turbulent flow combined with the use of different grid resolutions (note that for the LES, these range between meshes of 14.2×10^6–46×10^6 elements). Overall, the results show that the variability of the different predictions, especially those relative to the horizontal position and to the extension of the thermal cloud, increases with time and simulations at larger times ($t > 1.5$ s) can show significant differences, up to some tens of centimeters.

C. Particle clouds (stage II)

In this subsection, we compare and discuss the results concerning the centroid trajectories and the particle cloud size for seven different diameters (4, 8, 16, 32, 64, 128, and 256 μm). Table II summarizes the different cases for stage II, which include nine simulations that consider non-evaporative particles (6 URANS and 3 LES/Hybrid) and three simulations with evaporative particles (1 URANS and 2 LES/Hybrid).

Figures 8 and 9 show, respectively, the trajectories of the centroids of the non-evaporative particle clouds for the URANS-based simulations and for the LES, together with the predictions of the DNS. The corresponding trajectories for evaporative particles are plotted in Figs. 10 and 11.

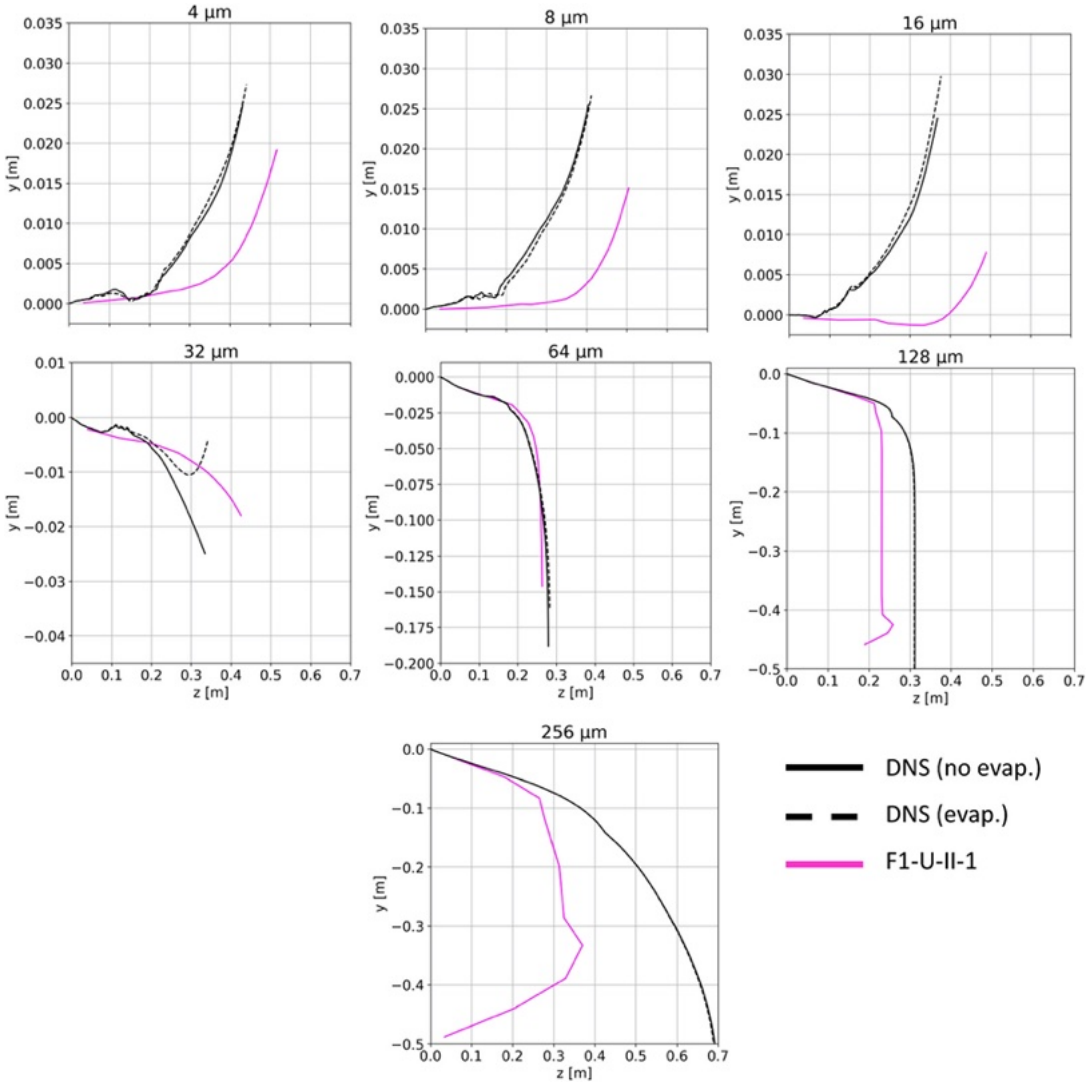

FIG. 10. Trajectories of evaporative particle clouds predicted by the URANS-based simulations.

Physics of Fluids ARTICLE scitation.org/journal/phf

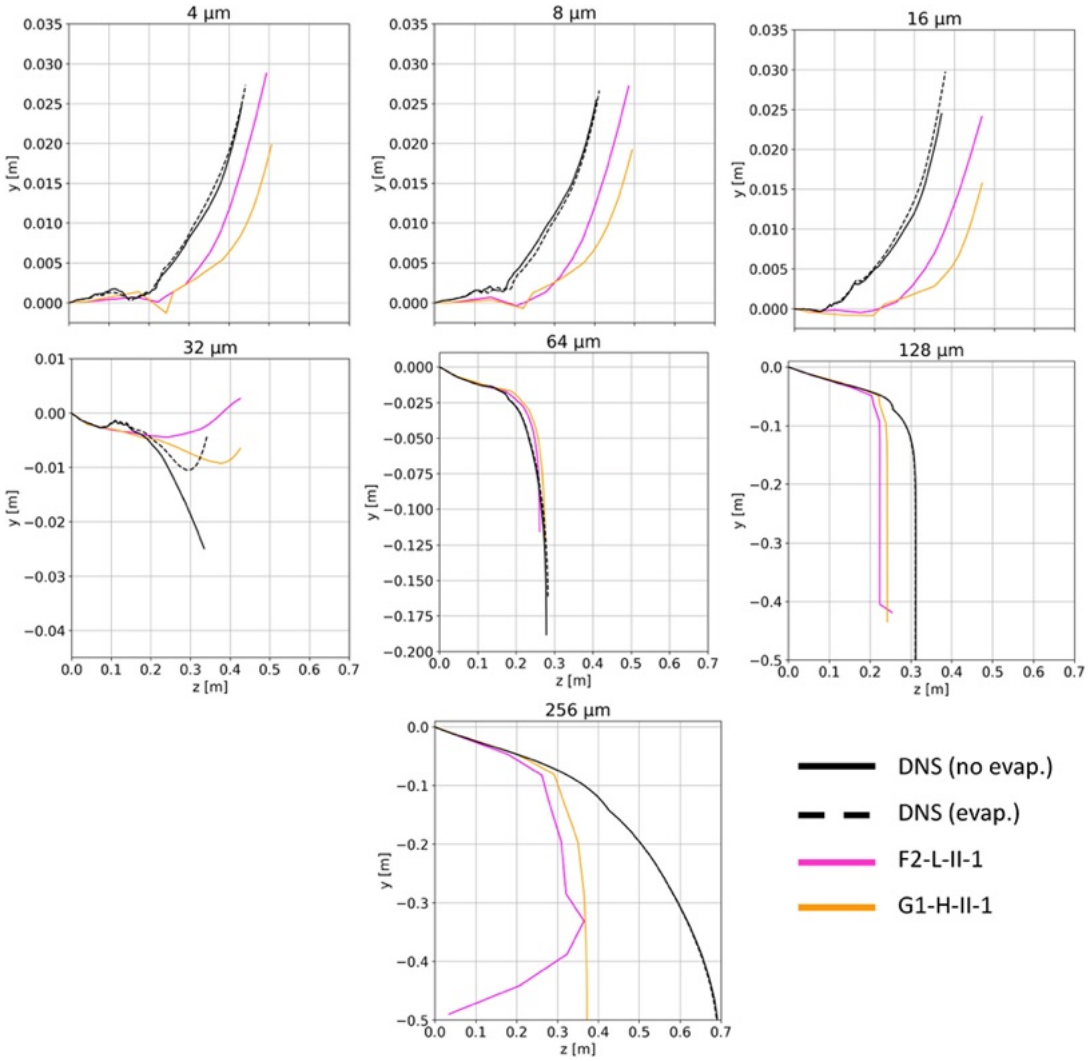

FIG. 11. Trajectories of evaporative particle clouds predicted by the by LES.

Figure 8 (URANS) shows that cloud centroid trajectories for the small particles (4, 8, and 16 μm, top-row panels the figure) mostly remain afloat within the thermal puff and progressively increase their axial range, departing from the DNS result as their size increases. This is also observed for the evaporative particles, as shown in the top panel of Fig. 10 (URANS). A similar trend is also depicted in Figs. 9 and 11 corresponding to the predictions of LES.

This increased axial range for the evaporative and non-evaporative particles with diameters 8 and 16 μm, with respect to the DNS, can be attributed to the reduced vertical span of the thermal puff predicted by the URANS-based and LES simulations in comparison with the DNS (see, for example, the vertical sizes of the thermal puff at $t = 0.4$ s and $t = 1.5$ s in Fig. 6). The reduced vertical size of the thermal puff is associated with less vertical mixing and higher axial fluid velocities that transport particles of increasing inertia (4, 8, and 16 μm) to progressively larger axial positions as they remain afloat within the thermal puff.

The comparison of the top panels of Figs. 8 (URANS) and 9 (LES) shows that the axial spread of the particle centroid predicted by LES is reduced with respect to the DNS. This agrees with the enhanced vertical mixing within the thermal cloud that LES is able to reproduce in comparison with the URANS-based simulations, thus resulting in a wider thermal cloud, as shown in Fig. 6.

For the smaller particle sizes (4, 8, and 16 μm), the URANS predictions (Fig. 8) do not exhibit a clear trend based on the specific turbulent model. For example, the results for cases A1-U-II-0, A2-U-II-0, and E1-U-II-0, computed with the k-ε models, notably differ from those reported for cases A3-U-II-0, C1-U-II-0, and F1-U-II-0, which

Physics of Fluids ARTICLE scitation.org/journal/phf

used the k-ω models. Specifically, both groups of simulations predicted very similar cloud trajectories with small variability, potentially explained by differences in the mesh resolutions. Compare, for example, the DNS with cases A3-U-II-0 and C1-U-II-0 performed with the k-ω models but with 0.6×10^6 and 6.2×10^6 elements.

The trajectory of the cloud centroid for the particles with size 32 μm strongly depends on the evaporation of the particles. As indicated by the DNS trajectories shown in Figs. 8–11, the 32 μm particles remain afloat at $t = 1.5$ s if evaporation is considered but tend to fall if evaporation is not considered. This trend is generally well captured by URANS and LES, except for the cases F2-U-II-0 (see Fig. 9) and F1-U-II-1 (see Fig. 10).

According to the DNS, the larger particles with diameters 64, 128, and 256 μm tend to fall with essentially the same trajectory irrespectively of the evaporation. For some cases (for example, A1-U-II-0, A2-U-II-0, or C1-U-II-0 in Fig. 8), the trajectories of the cloud centroid for the 256 μm particles show backward trajectories (i.e., toward the plane $z = 0$ plane) at large times. This is probably caused by the fact that, at large times, particles that have reached the bottom of the computational domain are excluded from the calculation of the centroid, which takes into account only the remaining particles injected at the end of the exhalation (which are freely falling relatively close to the inlet pipe). This effect can explain the departure from the DNS of the trajectories of the clouds for particles with the largest diameters (128 and 256 μm). However, for these cases, the trajectories of the centroid at small times (namely, close to the flow injection) compare well with those provided by DNS.

Contrary to what is observed for smaller particles, the URANS-based simulations tend to underestimate the axial range of the particle cloud centroids for particles with quasi-ballistic trajectories (e.g., those with diameter equal to 64 μm or larger). This may be due to the reduced vertical size of the thermal cloud predicted by the URANS-based simulations, which would explain why these relatively massive particles tend to leave the thermal cloud earlier than in DNS.

The vertical and horizontal positions of the cloud centroid as well as its size for the case of non-evaporative and evaporative particles with diameters 4 and 32 μm at $t = 0.4$ and $t = 1.5$ s are shown in Figs. 12 and 13. For reference, the DNS predictions of the particle clouds (green lines) and the DNS predictions of the centroid and sizes of the thermal cloud (black lines) are also included. We selected these two specific particle diameters, out of the seven values considered, to illustrate the effect of the different numerical approaches on the predictions when particles remain afloat within the thermal puff for large times. In Figs. 12 and 13, the data corresponding to the non-evaporative particles are plotted on panels (a-0) to (d-0), while the data of the evaporative particles are shown in panels (a-1) to (d-1).

Figure 12 shows that the DNS predictions of the vertical position of the centroids of the particles, which tend to fall due to of gravity, are below the centroids of the thermal cloud, which tend to rise due to buoyancy. In general, the predictions of the vertical position of the

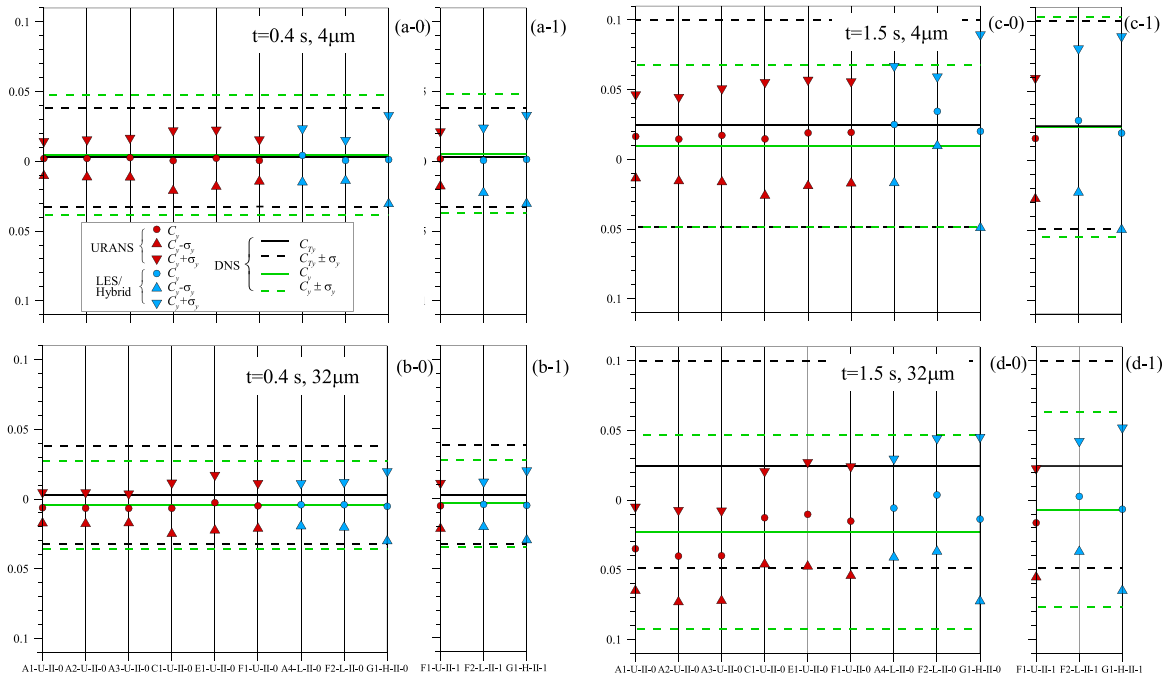

FIG. 12. Vertical positions of the centroids [c_y, see Eq. (1)] and vertical sizes [σ_y, see Eq. (2)] of the non-evaporative and evaporative particle clouds. (a-0) Non-evaporative and (a-1) evaporative clouds of particles of 4 μm at $t = 0.4$ s. (b-0) Non-evaporative and (b-1) evaporative clouds of particles of 32 μm at $t = 0.4$ s. (c-0) Non-evaporative and (c-1) evaporative clouds of particles of 4 μm at $t = 1.5$ s. (d-0) Non-evaporative and (d-1) evaporative clouds of particles 32 μm at $t = 1.5$ s. The centroid [c_{Ty}, see Eq. (3)] and vertical size [σ_{Ty}, see Eq. (4)] of the thermal cloud is indicated in black lines for comparison.

Physics of Fluids ARTICLE scitation.org/journal/phf

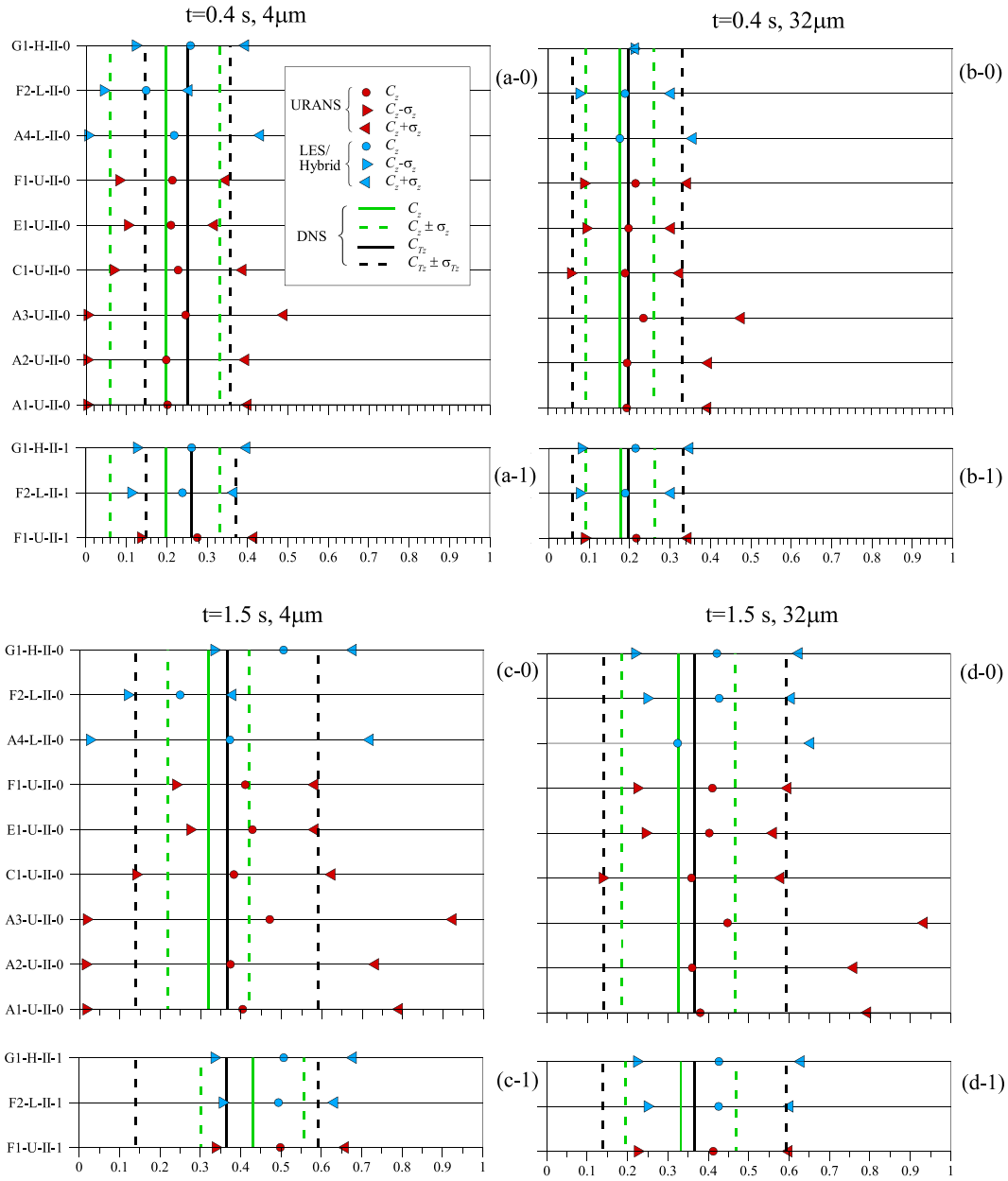

FIG. 13. Horizontal positions of the centroids [c_y, see Eq. (1)] and horizontal sizes [σ_y, see Eq. (2)] of the non-evaporative and evaporative particle clouds. (a-0) Non-evaporative and (a-1) evaporative clouds of particles of 4 μm at $t = 0.4$ s. (b-0) Non-evaporative and (b-1) evaporative clouds of particles of 32 μm at $t = 0.4$ s. (c-0) Non-evaporative and (c-1) evaporative clouds of particles of 4 μm at $t = 1.5$ s. (d-0) Non-evaporative and (d-1) evaporative clouds of particles 32 μm at $t = 1.5$ s. The centroid [c_{Tz}, see Eq. (3)] and vertical size [σ_{Tz}, see Eq. (4)] of the thermal cloud is indicated in black lines for comparison.

centroid of the non-evaporative particle clouds (panels a-0, b-0, c-0, and d-0) are very similar among the different cases, including URANS-based simulations and LES, and in agreement with DNS, especially at short times (i.e., at $t = 0.4$ s). However, the predictions of the vertical sizes of the particle clouds are systematically underpredicted in comparison with the DNS. A similar trend has been found and discussed in Subsection III B when comparing the vertical sizes of the thermal cloud shown in Fig. 6. The effect of evaporation on the

Physics of Fluids ARTICLE scitation.org/journal/phf

vertical position of the centroid of the particle cloud appears to be very limited, as it can be seen by comparing the cases A1-U-II-0 with the case A1-U-II-1 corresponding to URANS-based simulations or the case F2-L-II-0 with the case F2-L-II-1 for LES. As predicted by DNS, the vertical size of the particle cloud is, in general, increased if evaporation is considered, especially for 4 μm particles at $t = 1.5$ s.

The horizontal extensions of the non-evaporative and evaporative clouds of particles with diameters 4 and 32 μm are plotted in Fig. 13. As expected, the DNS results indicate that the position of the centroid is generally located at a smaller axial position compared to the centroid of the thermal cloud. At $t = 0.4$ s, the URANS and LES predictions for the non-evaporative particles are close to the DNS results with a maximum difference, of about 0.05 m only. At larger times, the predictions exhibit a larger scatter and the maximum differences increase up to about 0.15 m. Both URANS-based simulations and LES perform similarly when compared with DNS. The horizontal size of the particle clouds is, in general, closer to the DNS results for the LES. URANS-based simulations obtained with coarser meshes (A1-U-II-0, A2-U-II-0, and A3-U-II-0) tend to overpredict the size of the cloud in comparison with simulations performed using finer meshes (C1-U-II-0, E1-U-II-0, and F1-U-II-0).

IV. CONCLUSIONS

In this paper, we presented and discussed the results of a collaborative study, carried out by seven research teams within the framework of an international Computational Fluid Dynamics (CFD) challenge. Each participating team was asked to numerically simulate the short-term short-range flow and resulting particle dispersion generated by a prototypical violent expiratory event consisting in a short injection of hot fluid into a colder, initially quiescent, ambient. The results reported by each team have been compared against two reference cases, including a single realization provided by a Direct Numerical Simulation (DNS) and an averaged ensemble of 13 independent Large-Eddy Simulations (LES). The information obtained from these predictions is relevant for two reasons. First, to establish measures oriented to the minimization of risk infection of diseases transmitted by pathogen-laden aerosols expelled during expiratory events. Second, to generate realistic initial conditions for simulations of the long-term long-range flow and particle dispersion in indoor and outdoor scenarios. The seven research teams have performed a total of 11 simulations of the same flow configuration, but with different meshes and turbulence modeling approaches. Six simulations are based on the numerical solution of the Unsteady Reynolds Averaged Navier–Stokes (URANS) equations and five are based on the LES approach. The dispersion of both evaporative and non-evaporative particles with diameters ranging from 4 to 256 μm has also been considered resulting in 12 simulations in total (7 based on the solution of the URANS equations and 5 based on the LES approach).

Overall, the URANS-based and the LES simulations correctly predict the vertical and horizontal mixing of the new jet formed during the flow injection ($0 \leq t \leq 0.4$ s). At later times, of the order of 1 second after the flow injection has ceased ($t \approx 1.5$ s), the vertical mixing of the thermal puff is, in general, underpredicted by both approaches with vertical sizes of the thermal cloud about 50% smaller than in DNS for URANS and 30% for LES. A larger variability in the predictions of the horizontal sizes of the thermal cloud is observed, but in general, both URANS and LES compare similarly well with the reference data. For the flow conditions considered, the specific turbulence model used for the URANS simulations has a very limited impact on the prediction of the position and extension of the frontal thermal puff. However, the use of finer meshes for the URANS-based simulations allows the thermal cloud to extend over larger horizontal distances, resulting in a better agreement with the DNS.

The trajectory and size of the particle clouds predicted by the DNS are, in general, well reproduced both by URANS-based and LES simulations. For the flow conditions simulated here, the cloud centroid exhibits wider axial ranges and lower vertical displacements than the DNS in the case of particles that remain afloat (4, 8, and 16 μm). These differences are more evident for the larger (16 μm) particles and for the URANS-based simulations. Their occurrence can be also connected to the under-predicted vertical mixing of the thermal puff discussed above. The 32 μm particles tend to remain afloat if evaporation is considered but tend to fall otherwise. For the specific flow, thermal and humidity conditions considered in this study, this trend is generally well reproduced by the different approaches. For the larger particles (64, 128, and 256 μm), which tend to follow quasi-ballistic trajectories and are less correlated with the local field compared to the smaller particles, the URANS and LES predictions are closer to the DNS.

ACKNOWLEDGMENTS

This study was funded by the Spanish Ministerio de Ciencia, Innovación y Universidades through the Grant Nos. PID2020-113303GB-C21 and RTI2018-100907-A-I00 (MCIU/AEI/FEDER) and by the Generalitat de Catalunya through the Grant No. 2017-SGR-1234. M.Z., V.R., and N.I. acknowledge the Super-Computer Center (SCC) «Polytechnic» for providing computational resources. J.W., M.Š., and J.R. would like to thank the valuable insight given by professors Paul Steinmann and Matjaž Hriberšek and the financial support of the Deutsche Forschungsgemeinschaft, Germany under Project No. STE 544/58-2 and the Slovenian Research Agency under Project No. P2-0196.

AUTHOR DECLARATIONS

Conflict of Interest

The authors have no conflicts to disclose.

Author Contributions

Jordi Pallares: Conceptualization (equal); Funding acquisition (equal); Resources (equal); Supervision (equal); Validation (equal); Visualization (equal); Writing – original draft (equal); Writing – review & editing (equal). **Nikolay Ivanov:** Data curation (equal); Investigation (equal); Validation (equal); Writing – review & editing (equal). **Robert Castilla:** Data curation (equal); Investigation (equal); Validation (equal); Writing – review & editing (equal). **Pedro Javier Gamez-Montero:** Data curation (equal); Investigation (equal); Validation (equal); Writing – review & editing (equal). **Gustavo Raush:** Data curation (equal); Investigation (equal); Validation (equal); Writing – review & editing (equal). **Hadrien Calmet:** Data curation (equal); Investigation (equal); Validation (equal); Writing – review & editing (equal). **Daniel Mira:** Data curation (equal); Investigation (equal); Validation (equal); Writing – review & editing

Physics of Fluids ARTICLE scitation.org/journal/phf

(equal). **Jana Wedel:** Data curation (equal); Investigation (equal); Validation (equal); Writing – review & editing (equal). **Mitja Štrakl:** Data curation (equal); Investigation (equal); Validation (equal); Writing – review & editing (equal). **Jure Ravnik:** Data curation (equal); Investigation (equal); Validation (equal); Writing – review & editing (equal). **Douglas Fontes:** Data curation (equal); Investigation (equal); Validation (equal); Writing – review & editing (equal). **Alexandre Fabregat:** Conceptualization (equal); Data curation (equal); Investigation (equal); Supervision (equal); Validation (equal); Writing – original draft (equal); Writing – review & editing (equal). **Francisco Jose de Souza:** Data curation (equal); Investigation (equal); Visualization (equal); Writing – review & editing (equal). **Cristian Marchioli:** Conceptualization (lead); Methodology (equal); Resources (equal); Supervision (equal); Validation (equal); Visualization (equal); Writing – original draft (equal); Writing – review & editing (equal). **Salvatore Cito:** Conceptualization (lead); Methodology (equal); Resources (equal); Supervision (equal); Validation (equal); Visualization (equal); Writing – original draft (equal); Writing – review & editing (equal). **Akim Lavrinenko:** Conceptualization (equal); Data curation (equal); Investigation (equal); Validation (equal); Visualization (equal); Writing – original draft (equal); Writing – review & editing (equal). **Hadifathul Akmal bin Norshamsudin:** Data curation (equal); Investigation (equal); Validation (equal); Writing – review & editing (equal). **Gábor Janiga:** Data curation (equal); Investigation (equal); Validation (equal); Writing – review & editing (equal). **David F. Fletcher:** Data curation (equal); Investigation (equal); Validation (equal); Writing – review & editing (equal). **Kiao Inthavong:** Data curation (equal); Investigation (equal); Validation (equal); Writing – review & editing (equal). **Marina Zasimova:** Data curation (equal); Investigation (equal); Validation (equal); Writing – review & editing (equal). **Vladimir Ris:** Data curation (equal); Investigation (equal); Validation (equal); Writing – review & editing (equal).

DATA AVAILABILITY

The data that support the findings of this study are available from the corresponding author upon reasonable request.

APPENDIX: DETAILS ON LES ENSEMBLE

In this Appendix, we describe the details of the LES performed to estimate the flow variability between instantaneous fields of different realizations. We performed 13 LES of the flow dispersion, without considering the particles, with the same boundary conditions as those indicated in Sec. II but adding different small perturbations to the time evolution of the inlet velocity. Figure 14 shows the time evolutions of the inlet velocity of the 13 simulations and the corresponding intensities of the fluctuations. It can be seen that the averaged time evolution of these realizations follows well the linear increase and decrease in the inlet velocity used for the simulations of the Challenge. The fluctuations have been modulated to have similar intensities as the turbulent flow at the outlet of the mouth according to the simulations of the flow in the upper respiratory tract during a violent expiratory event (Pallares *et al.*, 2022). These 13 LES were carried out up to $t = 2\,s$ ($\Delta t = 10^{-3}$ s) in a reduced cylindrical computational domain ($H = 50d$ and $D = 40d$,

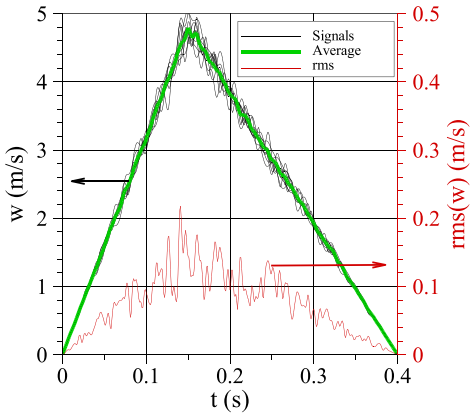

FIG. 14. Time evolution of the 13 different inlet velocities used to obtain different realizations of the flow. The average and the rms values are also indicated.

see Fig. 1) with a mesh resolution of 2.4×10^6 elements using a second-order finite volume code and the WALE SGS model, as in Pallares *et al.* (2022).

Figure 15 shows the time evolutions of the vertical [Fig. 15(a)] and axial [Fig. 15(b)] positions of the temperature centroid of these 13 simulations. The coordinates of the centroid of the thermal cloud (c_{Ty}, c_{Tz}) are computed using Eq. (3). The curves corresponding to the position of the centroid plus/minus the vertical (σ_{Ty}) and horizontal (σ_{Tz}) sizes defined in Eq. (4) have been also included to indicate the evolution of the dimensions of the thermal cloud [i.e., $c_{Ty} + \sigma_{Ty}$ and $c_{Ty} - \sigma_{Ty}$ in Fig. 15(a) and $c_{Tz} + \sigma_{Tz}$ and $c_{Tz} - \sigma_{Tz}$ in Fig. 15(b)]. The shaded regions in Fig. 15 mark the variability of the 13 simulations within two times the standard deviation of the position of the centroid of the temperature distribution at each time. The variability of the dimensions of the cloud is also indicated with shaded regions. Consequently, if the different instantaneous positions and sizes of the temperature cloud follow a normal distribution, the shaded areas mark the region where 95% of the realizations would be. To determine the normality of the vertical and axial positions of the centroid and the sizes of the thermal cloud, we performed the Anderson–Darling normality test (Anderson and Darling, 1954) with a 1% of significance for the 13 realizations at each time. This test indicates that the different realizations satisfy the normality test for $t > 0.2$ s. The data at $t < 0.2$ fail the test probably because of the random nature of the white-noise perturbations introduced in the time evolution of the inlet velocity (see Fig. 14).

The position of the centroid of the thermal cloud and its vertical [Fig. 15(a)] and horizontal [Fig. 15(b)] sizes obtained with the DNS reported in Fabregat *et al.* (2021a) are plotted in Fig. 14 with black lines. It can be seen that the vertical position and the vertical extension of the temperature cloud of the DNS is well within the variability of the 13 LES. For $t < 1.2$ s, the axial position and axial extension of the temperature cloud predicted by the DNS also fall within the variability of the 13 LES. At larger times ($t > 1.2$ s) and for the axial quantities [Fig. 15(b)], the DNS predicts a larger range, of about 5 cm, and extension for the thermal cloud. Note that for

Physics of Fluids ARTICLE scitation.org/journal/phf

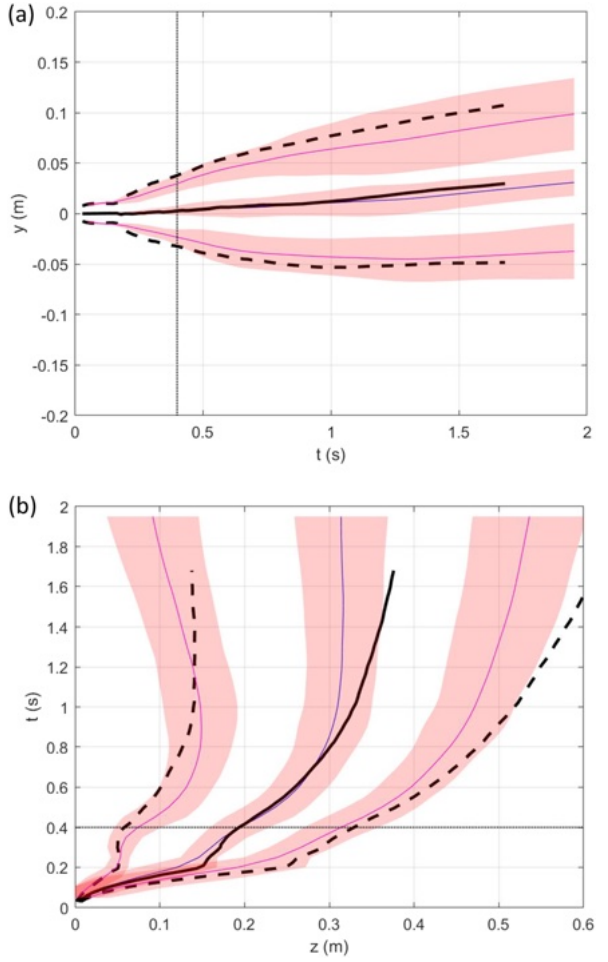

FIG. 15. Time evolutions of the horizontal (a) and vertical (b) positions of the centroid of the thermal cloud and the horizontal (a) and vertical (b) sizes. The predictions of the DNS are plotted in black. The time at which the flow injection ceases ($t = 0.4$ s) is indicated.

$t > 1.2$ s, the averaged axial position of the thermal cloud obtained with the DNS still increases with time, while the axial position for the 13 LES is essentially constant probably because of the excessive SGS viscosity at this late stage of the flow injection with a progressively reduced turbulence activity at these axial positions with a relatively coarse mesh.

REFERENCES

Abkarian, M., Mendez, S., Xue, N., Yang, F., and Stone, H. A., "Speech can produce jet-like transport relevant to asymptomatic spreading of virus," Proc. Natl. Acad. Sci. U. S. A. **117**(41), 25237–25245 (2020).

Alfaifi, H., Mohammadian, A., Gildeh, H. K., and Gharavi, A., "Experimental and numerical study of the characteristics of thermal and nonthermal offset buoyant jets discharged into stagnant water," Desalin. Water Treat. **141**, 171–186 (2019).

Anderson, T. W. and Darling, D. A., "A test of goodness-of-fit," J. Am. Stat. Assoc. **49**, 765–769 (1954).

ANSYS, Ansys Fluent–CFD Software (ANSYS, 2022).

Arjmandi, H., Amini, R., Kashfi, M., Abikenari, M. A., and Davani, A., "Minimizing the COVID-19 spread in hospitals through optimization of ventilation systems," Phys. Fluids **34**(3), 037103 (2022).

Arpino, F., Grossi, G., Cortellessa, G., Mikszewski, A., Morawska, L., Buonanno, G., and Stabile, L., "Risk of SARS-CoV-2 in a car cabin assessed through 3D CFD simulations," Indoor Air **32**(3), e13012 (2022).

Bhat, S. P., Kumar, B. R., Kalamkar, S. R., Kumar, V., Pathak, S., and Schneider, W., "Modeling and simulation of the potential indoor airborne transmission of SARS-CoV-2 virus through respiratory droplets," Phys. Fluids **34**(3), 031909 (2022).

Bourouiba, L., "The fluid dynamics of disease transmission," Annu. Rev. Fluid Mech. **53**, 473–508 (2021).

Calmet, H., Inthavong, K., Both, A., Surapaneni, A., Mira, D., Egukitza, B., and Houzeaux, G., "Large eddy simulation of cough jet dynamics, droplet transport, and inhalability over a ten minute exposure," Phys. Fluids **33**(12), 125122 (2021).

Chaudhuri, S., Basu, S., Kabi, P., Unni V. R., and Saha A., "Modeling the role of respiratory droplets in Covid-19 type pandemics," Phys. Fluids **32**(6), 063309 (2020).

Chong, K. L., Ng, C. S., Hori, N., Yang, R., Verzicco, R., and Lohse, D., "Extended lifetime of respiratory droplets in a turbulent vapor puff and its implications on airborne disease transmission," Phys. Rev. Lett. **126**(3), 034502 (2021).

Dbouk, T. and Drikakis, D., "On airborne virus transmission in elevators and confined spaces," Phys. Fluids **33**(1), 011905 (2021).

Diwan, S. S., Ravichandran, S., Govindarajan, R., and Narasimha, R., "Understanding transmission dynamics of COVID-19-type infections by direct numerical simulations of cough/sneeze flows," Trans. Indian Natl. Acad. Eng. **5**, 255–261 (2020).

Duchaine, F., Cizeron, M., Odier, N., Dombard, J., Marchall, S., Francois, N., and Poinsot, T., "High-performance CFD for respiratory droplet turbulent dispersion in a ventilated city bus," Int. J. Comput. Fluid Dyn. **35**(9), 758–777 (2021).

Duguid, J. P., "The size and the duration of air-carriage of respiratory droplets and droplet nuclei," Epidemiol. Infect. **44**(6), 471–479 (1946).

Fabregat, A., Gisbert, F., Vernet, A., Dutta, S., Mittal, K., and Pallarès, J., "Direct numerical simulation of the turbulent flow generated during a violent expiratory event," Phys. Fluids **33**(3), 035122 (2021a).

Fabregat, A., Gisbert, F., Vernet, A., Ferré, J. A., Mittal, K., Dutta, S., and Pallarès, J., "Direct numerical simulation of turbulent dispersion of evaporative aerosol clouds produced by an intense expiratory event," Phys. Fluids **33**(3), 033329 (2021b).

Fontes, D. H., Vilela, V., de Souza Meira, L., and de Souza, F. J., "Improved hybrid model applied to liquid jet in crossflow," Int. J. Multiphase Flow **114**, 98–114 (2019).

Foster, A. and Kinzel, M., "Estimating COVID-19 exposure in a classroom setting: A comparison between mathematical and numerical models," Phys Fluids **33**(2), 021904 (2021).

Gupta, J. K., Lin, C. H., and Chen, Q., "Flow dynamics and characterization of a cough," Indoor Air **19**(6), 517–525 (2009).

Ho, C. K., "Modelling airborne transmission and ventilation impacts of a COVID-19 outbreak in a restaurant in Guangzhou," China. Int. J. Comput. Fluid Dyn. **35**(9), 708–726 (2021).

Ho, C. K. and Binns, R., "Modeling and mitigating airborne pathogen risk factors in school buses," Int. Commun. Heat Mass Transfer **129**, 105663 (2021).

Indoor Air, https://onlinelibrary.wiley.com/doi/toc/10.1111/(ISSN)1600-0668.COVID-19-indoor-environment for COVID-19 and indoor environment, 2022.

International Communications in Heat and Mass Transfer, https://www.sciencedirect.com/journal/international-communications-in-heat-and-mass-transfer/vol/129/suppl/C for Numerical and experimental investigation of airborne pathogen transmission, 2021.

Kumar, R. and Dewan, A., "URANS computations with buoyancy corrected turbulence models for turbulent thermal plume," Int. J. Heat Mass Transfer **72**, 680–689 (2014).

Le Quéré, P., Weisman, C., Paillère, H., Vierendeels, J., Dick, E., Becker, R., Braak, M., and Locke, J., "Modelling of natural convection flows with large

temperature differences: A benchmark problem for low Mach number solvers. I. Reference solutions," ESAIM: Math. Modell. Numer. Anal. **39**(3), 609–616 (2005).
Liu, H., He, S., Shen, L., and Hong, J., "Simulation-based study of COVID-19 outbreak associated with air-conditioning in a restaurant," Phys. Fluids **33**(2), 023301 (2021).
Liu, K., Allahyari, M., Salinas, J., Zgheib, N., and Balachandar, S., "Investigation of theoretical scaling laws using large eddy simulations for airborne spreading of viral contagion from sneezing and coughing," Phys. Fluids **33**(6), 063318 (2021).
Mathai, V., Das, A., and Breuer, K., "Aerosol transmission in passenger car cabins: Effects of ventilation configuration and driving speed," Phys. Fluids **34**(2), 021904 (2022).
Mofakham, A. A. and Ahmadi, G., "On random walk models for simulation of particle-laden turbulent flows," Int. J. Multiphase Flow **122**, 103157 (2020).
Mohamadi, F. and Fazeli, A., "A review on applications of CFD modeling in COVID-19 pandemic," Arch. Comput. Methods Eng. **29**, 3567–3586 (2022).
Narayanan, S. R. and Yang, S., "Airborne transmission of virus-laden aerosols inside a music classroom: Effects of portable purifiers and aerosol injection rates," Phys. Fluids **33**(3), 033307 (2021).
Nazari, A., Jafari, M., Rezaei, N., Taghizadeh-Hesary, F., and Taghizadeh-Hesary, F., "Jet fans in the underground car parking areas and virus transmission," Phys. Fluids **33**(1), 013603 (2021).
Pallares, J. and Fabregat, A., "A model to predict the short-term turbulent indoor dispersion of small droplets and droplet nuclei released from coughs and sneezes," Indoor Built Environ. **31**(5), 1393–1404 (2022).
Pallares, J., Fabregat, A., and Cito, S., "Effects of upper respiratory tract anatomy and head movement on the buoyant flow and particle dispersion generated in a violent expiratory event," J. Aerosol Sci. **166**, 106052 (2022).
Pendar, M. R. and Páscoa, J. C., "Numerical modeling of the distribution of virus carrying saliva droplets during sneeze and cough," Phys. Fluids **32**(8), 083305 (2020).
Peng, S., Chen, Q., and Liu, E., "The role of computational fluid dynamics tools on investigation of pathogen transmission: Prevention and control," Sci. Total Environ. **746**, 142090 (2020).
Physics of Fluids, https://aip.scitation.org/toc/phf/collection/10.1063/phf.2021.FATV2020.issue-1 for Flow and the virus, 2021.
Pope, S. B., *Turbulent Flows* (Cambridge University Press, 2000).
Pourfattah, F., Wang, L. P., Deng, W., Ma, Y. F., Hu, L., and Yang, B., "Challenges in simulating and modeling the airborne virus transmission: A state-of-the-art review," Phys. Fluids **33**(10), 101302 (2021).
Rayegan, S., Shu, C., Berquist, J., Jeon, J., Zhou, L. G., Wang, L. L., Mbareche, H., Tardif, H., and Ge, H., "A review on indoor airborne transmission of COVID-19–modelling and mitigation approaches," J. Build. Eng. **64**, 105599 (2022).
Richards, J. M., "Inclined buoyant puffs," J. Fluid Mech. **32**(4), 681–692 (1968).
Saad, T., "CFD and Covid-19," Int. J. Comput. Fluid Dyn. **35**(9), 707 (2021).
Scorer, R. S., *Dynamics of Meteorology and Climate*, 1st ed. (Wiley, New York, 1997).
See https://www.openfoam.com/ for OpenFoam, 2022.
See https://www.paraview.org/ for ParaView, 2022.
Shao, X. and Li, X., "COVID-19 transmission in the first presidential debate in 2020," Phys. Fluids **32**(11), 115125 (2020).
Sheikhnejad, Y., Aghamolaei, R., Fallahpour, M., Motamedi, H., Moshfeghi, M., Mirzaei, P. A., and Bordbar, H., "Airborne and aerosol pathogen transmission modeling of respiratory events in buildings: An overview of computational fluid dynamics," Sustainable Cities Soc. **79**, 103704 (2022).
Siemens Product Lifecycle Management Software Inc., https://www.plm.automation.siemens.com/global/en/products/simcenter/STAR-CCM.html for STAR-CCM+, 2022.
Tang, J. W., Nicolle, A. D., Klettner, C. A., Pantelic, J., Wang, L., Suhaimi, A. B., Tan, A. Y. L., Ong, G. W., Su, R., Sekhar, C., Cheong, D. D. W., and Tham, K. W., "Airflow dynamics of human jets: Sneezing and breathing-potential sources of infectious aerosols," PloS One **8**(4), e59970 (2013).
Talaat, K., Abuhegazy, M., Mahfoze, O. A., Anderoglu, O., and Poroseva, S. V., "Simulation of aerosol transmission on a Boeing 737 airplane with intervention measures for COVID-19 mitigation," Phys. Fluids **33**(3), 033312 (2021).
Trivedi, S., Gkantonas, S., Mesquita, L. C., Iavarone, S., Oliveira, P. M. D., and Mastorakos, E., "Estimates of the stochasticity of droplet dispersion by a cough," Phys. Fluids **33**(11), 115130 (2021).
Vázquez, M., Houzeaux, G., Koric, S., Artigues, A., Aguado-Sierra, J., Arís, R. *et al.*, "Alya: Multiphysics engineering simulation toward exascale," J. Comput. Sci. **14**, 15–27 (2016).
Vreman, A. W., "An eddy-viscosity subgrid-scale model for turbulent shear flow: Algebraic theory and applications," Phys. Fluids **16**(10), 3670–3681 (2004).
Wang, J., Alipour, M., Soligo, G., Roccon, A., De Paoli, M., Picano, F., and Soldati, A., "Short-range exposure to airborne virus transmission and current guidelines," Proc. Natl. Acad. Sci. U. S. A. **118**(37), e2105279118 (2021).
Wu, L., Liu, X., Yao, F., and Chen, Y., "Numerical study of virus transmission through droplets from sneezing in a cafeteria," Phys. Fluids **33**(2), 023311 (2021).
Xu, C. and Yu, C. W. F., "Prevention and control of COVID-19 transmission," Indoor Built Environ. **31**(5), 1159 (2022).
Yang, L., Li, X., Yan, Y., and Tu, J., "Effects of cough-jet on airflow and contaminant transport in an airliner cabin section," J. Comput. Multiphase Flows **10**(2), 72–82 (2018).
Yu, H., Mui, K., and Wong, L., "Numerical simulation of bioaerosol particle exposure assessment in office environment from MVAC systems," J. Comput. Multiphase Flows **10**(2), 59–71 (2018).
Zhang, Z., Han, T., Yoo, K. H., Capecelatro, J., Boehman, A. L., and Maki, K., "Disease transmission through expiratory aerosols on an urban bus," Phys. Fluids **33**(1), 015116 (2021).
Zhang, B., Guo, G., Zhu, C., Ji, Z., and Lin, C. H., "Transport and trajectory of cough-induced bimodal aerosol in an air-conditioned space," Indoor Built Environ. **30**(9), 1546–1567 (2021).
Zhou, M. and Zou, J., "A dynamical overview of droplets in the transmission of respiratory infectious diseases," Phys. Fluids **33**(3), 031301 (2021).

UNIVERSITAT ROVIRA I VIRGILI
NUMERICAL SIMULATIONS OF PARTICLE TURBULENT DISPERSION AND
DEPOSITION WITH IMPLICATIONS FOR THE SPREADING OF AIRBORNE DISEASES
Akim Lavrinenko

Chapter 4

Direct Numerical Simulation of pathogen-laden aerosol dispersion in buoyancy-driven turbulent flow within confined spaces

Direct Numerical Simulation of pathogen-laden aerosol dispersion in buoyancy-driven turbulent flow within confined spaces

Akim Lavrinenko*, Alexandre Fabregat, Fernando Gisbert, Jordi Pallares

Department of Mechanical Engineering, Universitat Rovira i Virgili, Av. Països Catalans 26, 43007, Tarragona, Spain

Abstract

Turbulent dispersion of particles is vital in understanding the transmission of airborne infectious diseases. Transmission primarily occurs via inhalation of pathogen-laden aerosols released when infected individuals breathe, talk, cough, or sneeze. We employ Direct Numerical Simulations to investigate aerosol dispersion in an idealized cubic room subjected to high Rayleigh numbers induced by natural convection. Temperature difference on opposing walls drive turbulent flow with a dominant large-scale recirculation.

The initial aerosol distribution consists of spherical solid particles (0.1-2.5 μm in diameter) randomly seeded within a spheres initially located on the main diagonal of the cavity. Analysis of particle relative dispersion and concentration variance reveals strong inhomogeneity, highlighting lower dispersion in the central area of the room and significantly higher dispersion near the walls.

Additionally, we introduce a new analytical model for aerosol cloud dispersion within the cubic room, comparing it with Direct Numerical Simulations. Results suggest that closed-form models in some cases provide reasonable estimates of particle mixing time. According to simulation results, homogeneous mixing inside the room is attained 500 seconds after the release even for the most unfavorable conditions. This research advances our comprehension of indoor aerosol dispersion, a critical factor for evaluating the risks associated with disease transmission.

Keywords: Particle transport, Airborne infectious diseases, Mixing rate, Natural convection, Turbulent dispersion, Differentially heated cavity.
PACS: 44.35.+c, 44.25.+f, 47.27.E-
2000 MSC: 76F25, 76T15

1. Introduction

The transport of aerosols in turbulent flows plays a central role in various processes. Its practical applications span various fields, including environmental and climate studies, human health and safety, industrial processes, and fundamental fluid dynamics research.

*Corresponding author
Email addresses: akim.lavrinenko@urv.cat (Akim Lavrinenko), alexandre.fabregat@urv.cat (Alexandre Fabregat), fernando.gisbert@urv.cat (Fernando Gisbert), jordi.pallares@urv.cat (Jordi Pallares)

In industrial applications, such understanding aids the optimization of processes like combustion, spray coating, and powder handling [1, 2, 3]. The behavior of particles in turbulent conditions also affects the transport and distribution of aerosols, influencing climate and weather patterns by interacting with sunlight, radiation balance, and cloud formation [4]. It is instrumental in gauging and reducing environmental impact, as seen in the dispersion of pollutants in the atmosphere and aquatic systems [5, 6]. Furthermore, it has substantial implications on outdoor [7] and indoor air quality [8, 9, 10]. These studies deepens our understanding of fluid flow behavior, mixing processes, and the interplay between dispersed and carrier phases.

Also, comprehending how aerosols travel in turbulent environments is essential in grasping the spread of airborne infectious diseases. This includes diseases such as the common cold, influenza, chickenpox, measles, tuberculosis [11], and more recently, COVID-19 [12]. By July 2023, the latter has sadly resulted in over 691 million cases and exceeded 6.9 million fatalities worldwide [13]. These insights into aerosol transport mechanisms hence hold significant implications for public health. Centers for Disease Control [14] and Prevention and the World Health Organization [15] urges to accelerate the research and development process, and develop new rules and standards to mitigate the spread of diseases transmitted by pathogen-laden aerosols.

The COVID-19 pandemic has underscored the importance of gaining a deeper understanding of physics of pathogen-laden transport. Research on this subject has been ongoing for a considerable period of time and various methods have been employed [16, 17, 18, 19, 20, 21].

Direct Numerical Simulations (DNS) by Fabregat et al. [22, 23] showed that human violent expiratory events (coughs and sneezes), could be divided into two stages. In the first stage that starts immediately after the violent expiratory event, the turbulent particle dispersion is dominated by the jet/puff flow generated by the rapid exhalation. Studies suggest that the aerosol clouds, at the culmination of the first stage of exhalation, can be roughly estimated as a sphere with a radius of about 0.3 meters [24, 25]. A second stage starts approximately 2 s after exhalation, once significant fraction of the turbulent energy has already dissipated due to viscosity. The primary drivers of particle dispersion then become ambient air currents influenced by natural factors, such as room temperature gradients, or forced convection mechanisms like Heating, Ventilation, and Air Conditioning systems [26]. Consequently, the long-term distribution and mixing attributes of the particles mostly depend on these large-scale ambient flows. To improve our understanding of inhomogeneous turbulent flow and aerosol dispersion, we numerically investigate here the mixing properties of an idealized particle cloud resembling that genereated by a rapid exhalation in a cubical room with no ventilation using fully-resolved simulations. Building upon the existing research [22, 23], this study focuses on the second stage of violent expiratory event, when the dispersion of pathogen-laden particle clouds is governed by a large-scale buoyancy-driven flow. Through DNS with Lagrangian Particle Tracking (LPT), we model the airflow and pathogen-laden particles within a cubical room with sides of ~ 3 m subjected to a temperature difference of 1.24 K applied to two pairs of differentially heated opposed walls. By analyzing the trajectories of the particles within the cloud, we examine the spatial dependence of the mixing time for the particle cloud and given particle size. Using particle relative dispersion, we compare the mixing time of the particle cloud in our study with established regimes. This allows us to assess the behavior of the particle cloud in terms of dispersion characteristics. Additionally, utilizing the temporal evolution of the particle relative dispersion, we calculate the dispersion coefficient, which

provides quantitative information about the spreading and diffusion of particle cloud within the room. The costly DNS results are evaluated against closed-form models to appraise their predictive capabilities regarding mixing rates under idealized flow conditions. Two distinctive models are assessed - first, novel Gaussian model derived from an instantaneous aerosol point source, and second, a semi-analytical model for the dispersion of a continuous source proposed by Lau et al. [27]. The mixing times calculated using these closed models are compared to those from the DNS using the particle concentration variance as a comparative measure.

Mathematical and physical models are presented in Section 2. Simulation results, including instantaneous snapshots of the thermal flow, averaged outcomes, temporal particle relative dispersion and variance of the particle concentration, and a comparison with analytical model predictions, are presented and discussed in Section 3, 4. Conclusions drawn from the findings are outlined in Section 5. Additional details regarding the LPT model can be found in Appendix A (Section 6), while Appendix B (Section 7) provides, for completness, the derivation of the dispersion model equation proposed by Lau et al. [27].

2. Mathematical methods

In this study, we use the identical numerical setup described in Lavrinenko et al. [28]. The computational domain, representing an idealized cubical room, consists in a cavity of side length $l_s = 3.148$ m filled with air at average temperature $T_0 = 300$ K(see Fig. 1).

The bottom horizontal (floor) and the left vertical wall are kept at a constant temperature $T_h = T_0 + \Delta T/2$ while the top horizontal (ceiling) and the opposite right vertical wall which are kept at $T_c = T_0 - \Delta T/2$. The remaining vertical walls, normal to z, are assumed adiabatic. Temperature difference ΔT is 1.243 K and gravity acts in the $-y$ direction.

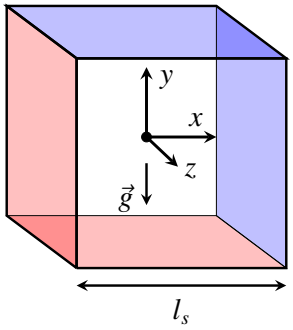

Figure 1: Sketch of the computational domain consisting of a $\left[-\frac{1}{2}, \frac{1}{2}\right]^3$ in non-dimensional units. Red and blue surfaces represent hot and cold walls respectively.

2.1. Carrier Phase Model

Assuming incompressibility conditions, the non-dimensional mass, momentum and thermal energy conservation equations under the Boussinesq approximation can be written as:

$$\frac{\partial u_i}{\partial x_i} = 0 \tag{1}$$

$$\frac{\partial u_i}{\partial t} + u_j \frac{\partial u_i}{\partial x_j} = -\frac{\partial p}{\partial x_i} + \frac{Pr}{\sqrt{Ra}} \frac{\partial^2 u_i}{\partial x_j \partial x_j} + Pr\theta\delta_{i2} \tag{2}$$

$$\frac{\partial \theta}{\partial t} + u_j \frac{\partial \theta}{\partial x_j} = \frac{1}{\sqrt{Ra}} \frac{\partial^2 \theta}{\partial x_j \partial x_j} \tag{3}$$

where t is time, u_i is the velocity component in the direction x_i, p is pressure and $\theta = \frac{T_0 - T}{\Delta T}$ is the temperature fluctuation. The Rayleigh and Prandtl number are defined as $Ra = (g\beta\Delta T l_s^3)/(\nu\alpha) = 3.6 \times 10^9$ and $Pr = \nu/\alpha = 0.7$ respectively where the velocity, length, time and temperature scales are $u_s = \alpha\sqrt{Ra}/l_s = 0.427$ m s^{-1}, $l_s = \alpha\sqrt{Ra}/u_s = 3.148$ m, $t_s = l_s/u_s = 7.372$ s and $T_s = \Delta T = 1.243$ K respectively.

Equations (1)-(3) are solved using NEK5000 [29], an open-source, high-order spectral element method (SEM) based solver designed for solving the incompressible Navier–Stokes equations. NEK5000 utilizes Nth-order tensor-product Lagrange polynomials as basis functions on the

Gauss–Lobatto–
Legendre quadrature points within each element, ensuring efficient evaluation and low storage costs for operators [30].

The solver employs a semi-implicit kth-order Backward Difference Formula (BDFk) and kth-order Extrapolation (EXTk) timestepping method. The time derivative is approximated using BDFk, while the nonlinear terms and other forcings are handled with EXTk. Viscous and pressure terms are treated implicitly, leading to the solution of a linear unsteady Stokes problem at each time step. This problem involves Helmholtz equations for each component of velocity, temperature, or scalars, and a Poisson equation for pressure [31]. NEK5000 is a widely utilized tool for both DNS and LES simulations across various flow configurations and applications [32, 33, 34].

The computational grid, with a total of approximately 300 million nodes, ensuring explicit resolution of all spatial and temporal scales as per the resolution criteria proposed by Scheel et al. [35] for similar buoyancy-driven flow configurations. The minimum and maximum grid cells are $\Delta X_{min} = \Delta Y_{min} = \Delta Z_{min} = 3.3 \times 10^{-3}$ and $\Delta X_{max} = \Delta Y_{max} = \Delta Z_{max} = 1.4 \times 10^{-4}$ non-dimensional units, respectively. For further details on the numerics and mesh generation, please refer to Fabregat and Pallares [36].

The Spectral Element Method (SEM) spatial discretization used in NEK5000 where the numerical approximation in each element can be expressed as a three-dimensional Legendre polynomial expansion of order N^3 is used to interpolate the particle velocity on the previous time step or in any other intermediate time in the predictor-corrector approach used in Exponential-Lagrangian Tracking Schemes (see details in [36]).

2.2. *Discrete phase model*

Particles are modelled as idealized globular and smooth spheres. Given the small particle size and high dilution, we assume a one-way coupling between the phases and neglect the particle collisions. When a particle deposits on the wall, it is subsequently reseeded to a random location within the domain.

The position of a given particle x_i^* can be written as:

$$\frac{dx_i^*}{dt} = u_i^* \tag{4}$$

where the particle velocity u_i^* can be determined as:

$$\frac{du_i^*}{dt} = \underbrace{\frac{u_i - u_i^*}{St_p}}_{\text{Drag}} + \underbrace{n_g \delta_{i2}}_{\text{Buoyancy}} + \underbrace{n_{th}\frac{\partial T}{\partial x_i}}_{\text{Thermophoresis}} + \underbrace{n_l \varepsilon_{ijk}\left[u_j^* - u_j\right]\omega_k}_{\text{Lift}} + \underbrace{n_i(t)}_{\text{Brownian}} \tag{5}$$

where St_p is the particle Stokes number, n_g is the magnitude of the buoyancy force experienced by a particle, δ_{ij} is the Kronecker delta, n_{th} is the pre-factor of the non-dimensional temperature gradient, n_l is the lift proportionality factor, ε_{ijk} is the Levi-Civita symbol, $\vec{\omega_k} = \vec{\nabla} \times \vec{u}$ is the flow vorticity and n_i is the Brownian force.

The particle transport model presented in Eqs. (4)-(5) assumes that there are five relevant forces acting on the particle, namely, hydrodynamic drag and lift, buoyancy, thermophoresis and Brow-

nian. The definitions of the different parameters in Eq. 5 can be found in Appendix A (Section 6) of this paper.

2.3. The Gaussian dispersion model for an instantaneous point source

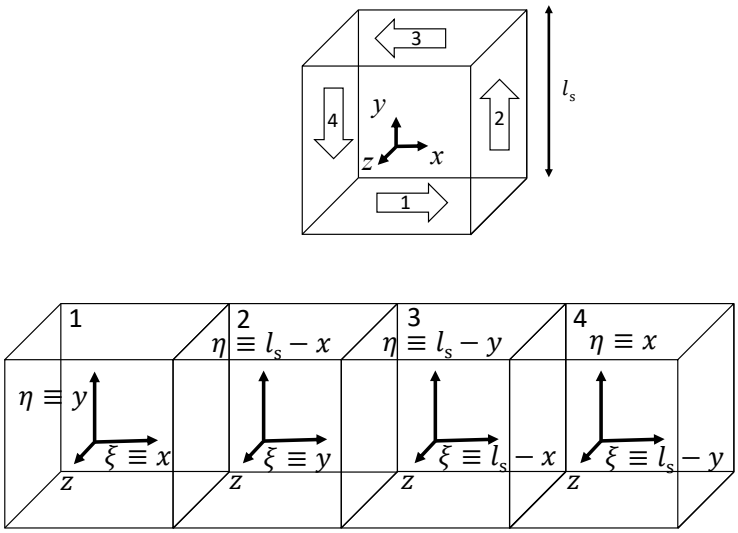

Figure 2: : (a) Sketch of the large-scale flow recirculation. (b) The channel used to model the dispersion process near the bottom wall (1), right vertical wall (2), top wall (3) and left vertical wall (4).

Computational Fluid Dynamics (CFD) simulations, such as Direct Numerical Simulations (DNS) and Large Eddy Simulations (LES), are widely used for investigating particle dispersion and are valuable for research and validation purposes. However, conducting these simulations demands substantial computational resources and generates vast data sets that necessitate time-consuming post-processing for the clear results and thus decision-making. As a result, there is a critical need for a reliable and efficient engineering tool capable of accurately estimating aerosol concentrations in indoor environments.

Addressing that need, we develop a Gaussian dispersion model that assumes the particle cloud advection along the path of the large-scale recirculation generated by the thermally active walls (see Fig. 2a). The cloud is assumed to be transported with a constant velocity (u_c) and dispersed by a constant turbulent diffusion coefficient (K). The distribution of particles along the path parallel to the four walls of the cavity of the large-scale recirculation is modelled similarly to the dispersion along a straight three-dimensional square duct sketched in Fig. 2b. The coordinate system of this domain has ξ, η and z as the streamwise, vertical and horizontal directions respectively. The domain is shown in Fig. 2b has a height and width of l_s and a streamwise dimension of $4l_s$, which corresponds, approximately to the path length of the large-scale recirculation sketched in Fig. 2a.

The dispersion of an instantaneous point source in an unbounded domain can be written as (see for example Seinfeld and Pandis [37] and Drivas et al. [38]).

$$c(x,y,z,t) = \frac{S}{8\,(\pi t K)^{3/2}} \exp\left[-\frac{\left(x+\frac{l_s}{2}-x_0+u_c t\right)^2}{4Kt} - \frac{\left(y+\frac{l_s}{2}-y_0\right)^2}{4Kt} - \frac{\left(z+\frac{l_s}{2}-z_0\right)^2}{4Kt}\right] \tag{6}$$

where c is concentration ($particles/m^3$), S is source strength ($particles/\mathrm{s}$), K is dispersion coefficient ($\mathrm{m^2\,s^{-1}}$), t is time (s) and u_c is velocity ($\mathrm{m\,s^{-1}}$).

Equation 6 can be adopted to the present simulation by expressing the original system of coordinate (x,y,z) in Fig. 2a to the transformed system of reference (ξ,η,z) shown in Fig. 2b. An instantaneous source is initially located at position ξ_0,η_0,z_0 inside the room with a constant streamwise velocity u_c. The new expression now reads:

$$c(\xi,\eta,z,t) = \frac{S}{8\,(\pi t K)^{3/2}} \exp\left(-\frac{\left(\xi+\frac{l_s}{2}-\xi_0-u_c t\right)^2}{4Kt}\right) R_z R_\eta \tag{7}$$

where ξ_0 , η_0 and z_0 ($-l_s/2 < \xi_0 < l_s/2,\ -l_s/2 < \eta < l_s/2,\ -l_s/2 < z < l_s/2$) are the coordinates of the point source emission. The sum in the term R_z accounts for the particle reflection on front and back walls of the channel located $z = -l_s/2$, $z = l_s/2$ and R_η accounts for the particle reflection on the bottom and top walls located at $\eta = -l_s/2$ and $\eta = l_s/2$ respectively.

The dispersion and reflection terms along the z direction:

$$R_z = \sum_{i=-\infty}^{i=\infty}\left[\exp\left(-\frac{(z+\frac{l_s}{2}+2il_s-z_0)^2}{4Kt}\right) + \exp\left(-\frac{(z+\frac{l_s}{2}+2il_s+z_0)^2}{4Kt}\right)\right] \tag{8}$$

Correspondingly along the η direction,

$$R_\eta = \sum_{i=-\infty}^{i=\infty}\left[\exp\left(-\frac{(\eta+\frac{l_s}{2}+2il_s-\eta_0)^2}{4Kt}\right) + \exp\left(-\frac{(\eta+\frac{l_s}{2}+2il_s+\eta_0)^2}{4Kt}\right)\right] \tag{9}$$

The instantaneous concentration distribution obtained from Eq. 7 in the channel is mapped into the cavity by transforming the system of coordinates ξ,η,z into the system of coordinates x,y,z, with its origin located at the center of the cavity (see Fig. 2a).

2.4. Semi-analytic model by Lau et al. [27]

Lau et al. [27] developed a semi-analytical model to examine the two-dimensional concentration of pathogen-laden particles in indoor environments. An infectious person is considered as the continuous source of infectious aerosols. All aerosols have the same size and carry the same amount of virus. The aerosols are transported by advection caused by the airflow with velocity

u_c, which follows the recirculating loop. It is assumed that the aerosols are passively released into the flow stream, as the expelled air from the mouth and nose during breathing and talking. In the absence of aerosol removal by ventilation, biological deactivation of the virus, and gravitational settling the time evolution of the concentration can be written as:

$$\begin{aligned} C(x,y,t) = {} & \frac{2R}{4\pi K h} \\ & \int_0^t \sum_{m=-\infty}^{\infty} \left[\exp - \frac{(x + \frac{l_s}{2} - u_c t - x_0 - 2ml)^2}{4Kt} + \right. \\ & \left. + \exp - \frac{(x + \frac{l_s}{2} + ut + x_0 - 2ml)^2}{4Kt} \right] \cdot \\ & \cdot \sum_{n=-\infty}^{\infty} \left[\exp - \frac{(y + \frac{l_s}{2} - y_0 - 2nw)^2}{4Kt} + \exp - \frac{(y + \frac{l_s}{2} + y_0 - 2nw)^2}{4Kt} \right] \mathrm{d}t \end{aligned} \tag{10}$$

where C is the concentration of infectious aerosols ($aerosols/m^2$) at all points on the surface of the looping airflow, R is the infectious aerosol emission rate ($aerosols$/s), l, w, h are length, width and height of the room respectively (m), x_0, y_0 is point source location. For completeness, more details on the original model are given in the Appendix B 7 of this paper and in the original paper of Lau et al. [27].

Equation 10 represents a model for continuous aerosol source, where the number of particles always increases. In contrast, both in the DNS and the model given in Eq. 7, the particle count remains constant, modelling particle cloud from a single isolated violent respiratory event. To allow direct comparison with the DNS results for a finite release of particles, the model of Lau et al. [27] was modified to consider injection of particles into the domain only during the exhalation event, which lasts for 0.4 s ($t = 0$ to $t = t_{inj} = 0.4$ s). Beyond t_{inj}, the aerosol count is set constant by subtracting additional aerosols every time step from the continuous source, as shown in Eq. 11.

$$C_{cough}(x,y,t) = C(x,y,t) - (C(x,y,t) - C_{inj}(x,y,t)) \tag{11}$$

Here, C_{cough} is the concentration for times $t > t_{inj}$, C is the concentration calculated using Eq. 10, and C_{inj} is the concentration calculated during the time interval from $t = 0$ to t_{inj}.

2.5. *Particle dispersion*

In order to quantify the ability of the flow to disperse and homogenize passive particle cloud across the entire room we use the relative dispersion of the particles and the variance of particle concentration.

The squared relative dispersion D^2 is defined as the average square distance over all particles pairs and it can be calculated using [6]:

$$D^2 = \frac{1}{P} \sum_{i,j} [x_i^* - x_j^*]^2 + [y_i^* - y_j^*]^2 + [z_i^* - z_j^*]^2 \tag{12}$$

where x^*, y^*, z^* are the individual particle coordinates and P is number of all possible particle pairs. The time evolution of D^2 can be represented under a scaling of the form:

$$D^2 \sim t^v, \tag{13}$$

Different regimes of relative dispersion have been identified based on the value of power number: $v = 3$ corresponds to Richardson's dispersion (homogeneous turbulent flows), shear/ballistic dispersion has $v = 2$, and standard eddy-diffusion (random walk) is when $v = 1$ [39].

The rate of growth of average square distance over all particles pairs can be related with the relative diffusivity as [40]:

$$K = \frac{1}{2}\frac{dD^2}{dt} \tag{14}$$

The variance of particle concentration serves as a metric for quantifying deviations from a uniform concentration distribution. To implement this approach, we partitioned our cavity into five equal segments in each direction, resulting in a total of N equally sized bins. We then monitored the particle concentration within each bin and compared them to the expected uniform distribution. The variance is defined as [41]:

$$\sigma^2 = \frac{1}{N}\sum_{i=1}^{N}(n_i - \mu)^2 \tag{15}$$

where N is number of the bins, n_i is particle concentration in the bin and μ is the mean particle concentration:

$$\mu = \frac{1}{N}\sum_{i=1}^{N} n_i \tag{16}$$

3. Results and discussion

As an example of the large scale flow structure Fig. 3, shows slices of the non-dimensional temperature field at different locations. The left panel of the figure shows the temperature contours on the plane $z = 0$ and it depicts the distinct features of the large-scale, persisting, clockwise circulation pattern on the temperature field. Distinct hot air vertices are noticeable close to the left and bottom hot walls, while the top and right cold walls display vigorous mixing of hot and cold air. Within the central region, the temperature field maintains a relatively stable and tranquil state, with only minor fluctuations observed around the average temperature (T_0). The right panel of the figure shows a slice at $y = 0.495$, located within the boundary layer of the cold top wall. This layer is characterized by the presence of cold fluid streaks that align roughly with the dominant flow direction, which is from left to right.

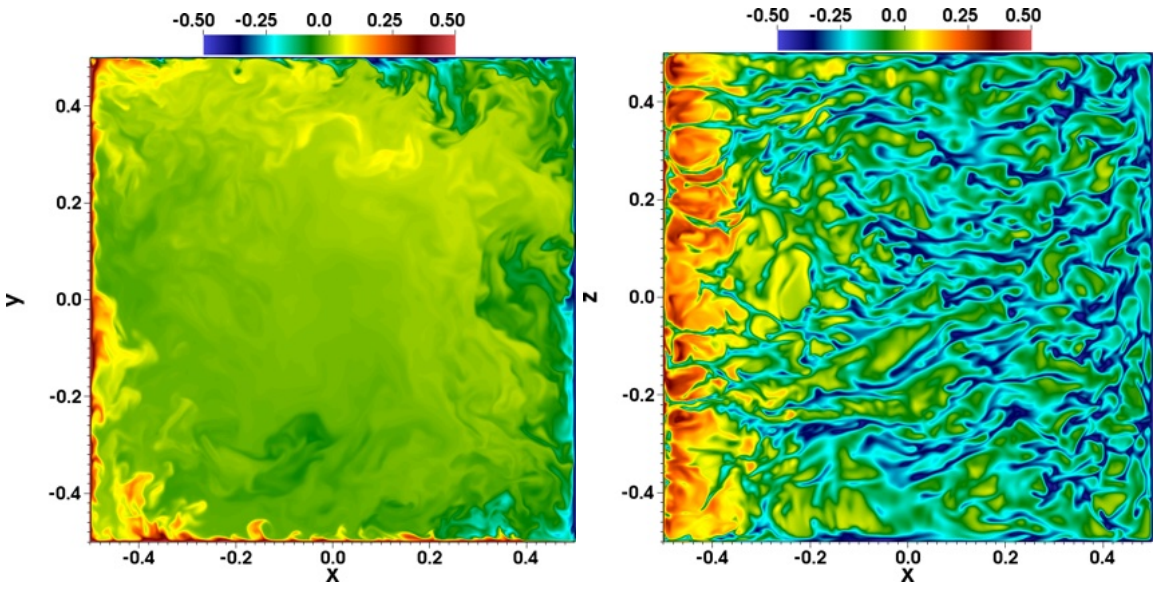

Figure 3: Left: instantaneous temperature slice at $z = 0$ (room bisector plane). Right: instantaneous temperature slice at $y = 0.495$ (near the cold horizontal representing the ceiling). All dimensions are non-dimensional.

This pattern is characterized by a distinct velocity and temperature profiles. Figure 4 shows the time-averaged non-dimensional temperature ($\langle T \rangle$) and velocities ($\langle u_x \rangle$, $\langle u_y \rangle$) along the bisector of the vertical symmetry plane of the cavity. The maximum vertical and horizontal average velocities are 0.246 and 0.188 in non-dimensional units respectively. Overall mean velocity in the cavity is 0.05.

In dimensional units the maximum average velocity is 0.105 $\mathrm{m\,s^{-1}}$ within the momentum boundary layer and near-zero velocities at the center of the room. Overall, the mean air velocity in the room is 0.021 $\mathrm{m\,s^{-1}}$, for a Prandtl and Rayleigh number considered.

As an example, Fig. 5 shows $(x - y)$ and $(x - z)$ projections of particle trajectories of three arbitrarily selected particles on the left and right panels, respectively. Filled and empty markers

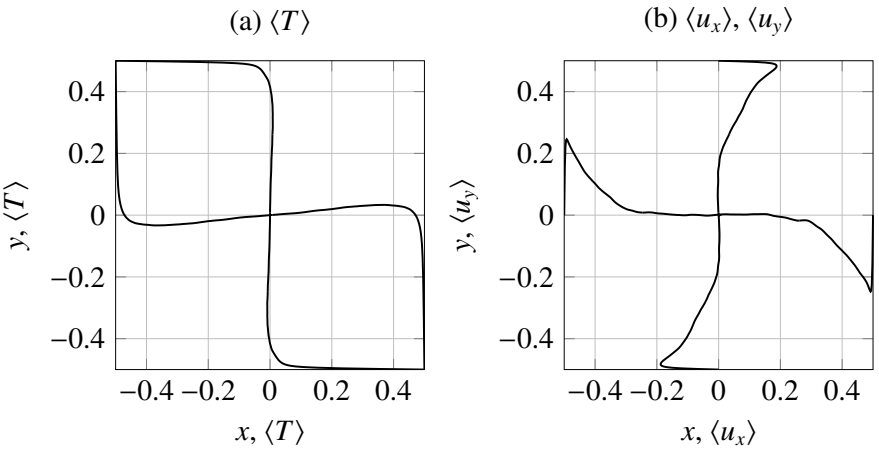

Figure 4: Time-averaged non-dimensional temperature (a) and velocity (b) profiles along the horizontal and vertical bisectors of the symmetry plane of the cavity z = 0 for $Ra = 3.6 \times 10^9$.

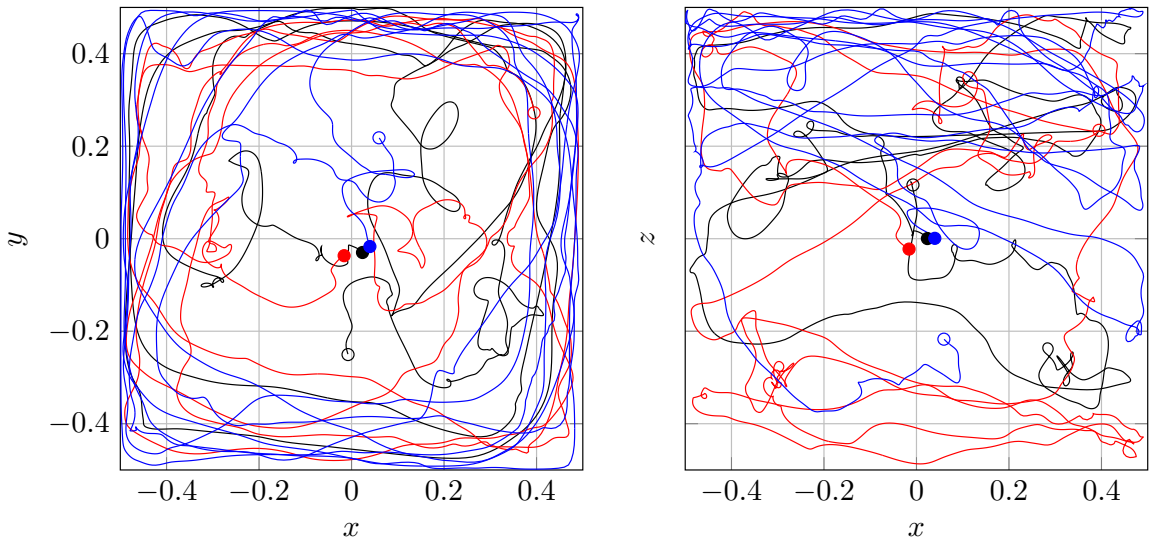

Figure 5: Three arbitrary particle trajectories (in different color) as seen from the *x*-*y* (left panel) and *x*-*z* (right panel) directions. Filled and empty markers indicate initial and terminal positions for each particle trajectory.

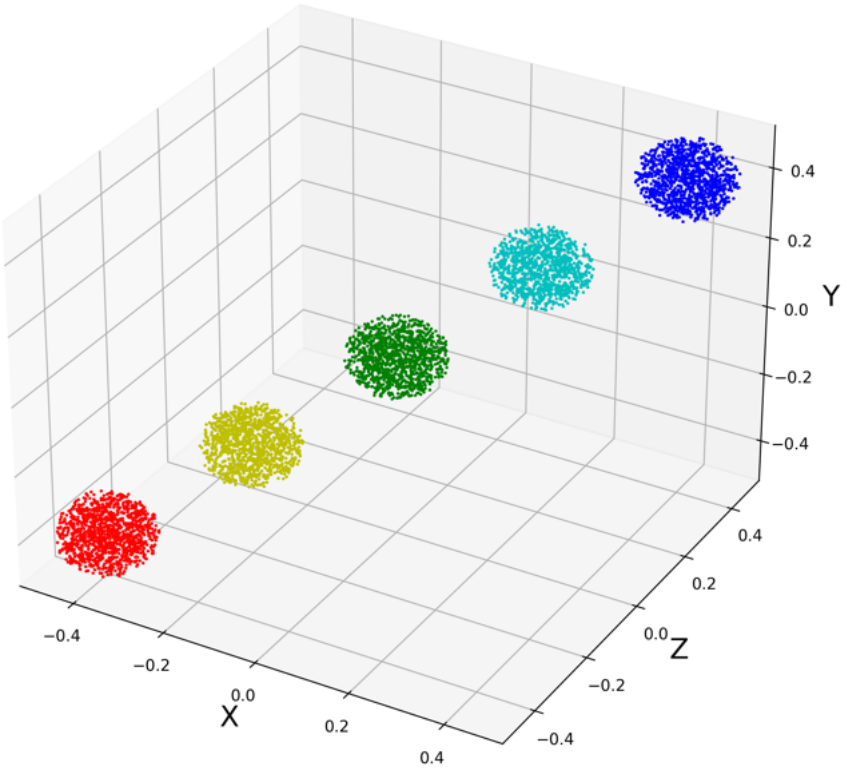

Figure 6: Initial position of the clouds (Table 1 provides the center coordinates of each cloud).

indicate starting and final positions for all three trajectories respectively. Released near the cavity center at $(0, 0, 0)$, particles initially spend some time in this low speed region before being captured and transported by the high-velocity clockwise dominant circulation. The lateral displacement in z direction of the particle trajectories are shown in the vertical projection in the right panel of Fig. 5. The results suggest that the particles do not have any attracting manifolds, nor any preferential location and are circulated across the entire width of the cavity under the action of the dominant large-scale circulation flow.

The pathogen-laden aerosol cloud, representing a human violent exhalation at the second stage,

No	color	$x, y, z,$	$\langle K_{sa} \rangle$ m^2 s^{-1}
1	red	-0.4, -0.4, -0,4	0.0133
2	yellow	-0.2, -0.2, -0,2	0.0088
3	green	0.0, 0.0, 0.0	0.0047
4	cyan	0.2, 0.2, 0,2	0.0129
5	blue	0.4, 0.4, 0,4	0.0110
		mean	0.01

Table 1: Particle cloud centroid coordinates and size-averaged dispersion coefficient of each sphere.

is modeled by randomly seeding smooth solid spherical particles within spheres with a radius of 0.3 m. We consider the dispersion of a total of 25 particle clouds (i.e. 5 locations of the clouds and 5 particle sizes). The trajectories of each cloud are tracked throughout the entire simulation period, which corresponds to 1.4×10^3 s (23 min). Using the particle trajectories of each cloud, we compare the mixing by utilizing the particle relative dispersion and the variance of the particle concentration.

Fig. 6 illustrates the initial locations of the particle clouds considered in this study. The figure displays the 5 clouds located along the main diagonal of the cavity. Each cloud comprises 5 particle sizes: 0.1, 0.5, 0.7, 1.3, and 2.5 μm. On average, there are 230 particles of each size present in each cloud. Table 1 provides the spatial coordinates of the considered cloud center locations along with their corresponding colors. Additionally, table 1 shows time and size averaged dispersion coefficient $\langle K_{sa} \rangle$ of each sphere and the average dispersion coefficient averaged over all sphere locations and particle sizes in the last row of the table. Subscript *sa* stands for size averaged value.

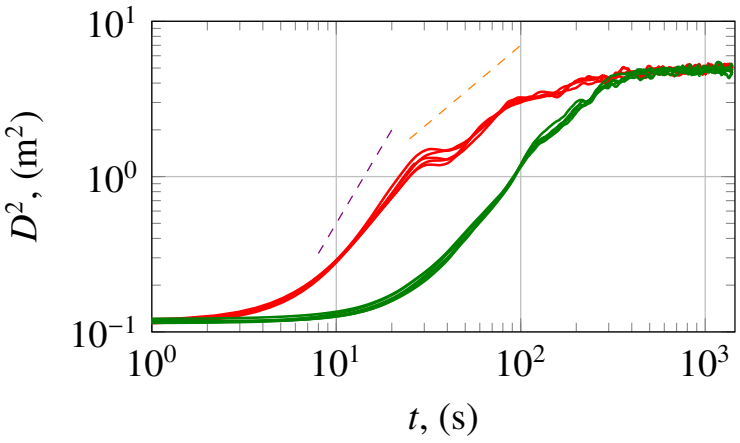

Figure 7: Temporal evolution of the relative dispersion D^2 in m^2 of particle sphere located in the center and the corner of the cavity for each considered particle size. Violet and orange dashed lines corresponds to shear/ballistic ($\nu = 2$) and linear diffusion ($\nu = 1$) regimes respectively.

To study the ability of the background air currents to disperse aerosol clouds we computed the

time evolution of the relative dispersion defined in Eq. 13. Fig. 7 shows the relative dispersion (D^2) for each particle size for the particle clouds located in the corner (green color) and in the center (red color) of the room (see Table 1 for coordinates). We use a uniform color to depict all particle sizes as there is minimal variation in the relative dispersion between the particle sizes for single cloud location. Also, in the case of the red cloud during the plateau period from 20 to 50 s, there are no distinctive trends and regular patterns observed at that moment. The figure shows that clouds of particles with different sizes located in the center of the cavity (green) require more time to initiate dispersion, and that the dispersion rate starts to increase rapidly at around 20 s, whereas the relative dispersion of the particle clouds initially located in the corner (red) start to grow at 3 s. After these initial growths the rate of dispersion in both cases is similar and is maximum with the rate of the ballistic regime (See Eq. 12). Violet and red dashed lines show shear/ballistic ($\nu = 2$) and linear diffusion ($\nu = 1$) regimes respectively. The average distance between particle pairs continues to grow until 500 s for both cases, where the relative dispersion reaches a plateau with the average distance between particle pair $D \sim 2.2$ m. At this point, it stops growing indicating that all particles are homogeneously mixed within the cavity. Aerosol clouds located in the corner reach the highest rate of dispersion at ~15 s, while clouds in the center at ~40 s. In both cases highest dispersion rate is close to shear/ballistic regime.

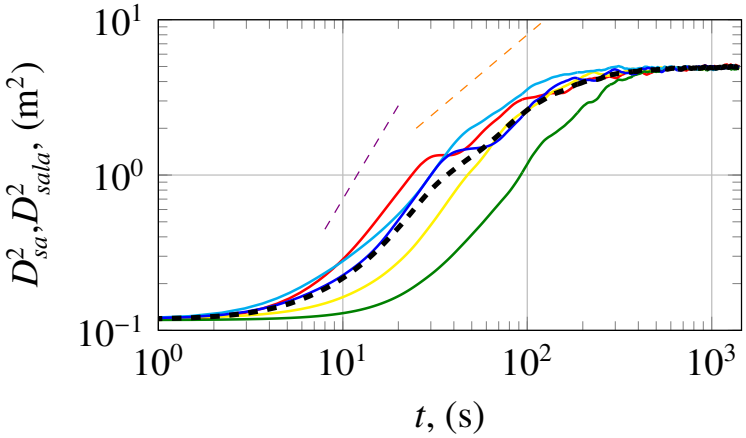

Figure 8: Temporal evolution of the relative dispersion D^2_{sa} in m^2 averaged over all particle sizes for each initial position, for color definition see Table 1. Black thick dashed line shows relative dispersion averaged over all particle initial cloud positions and sizes D^2_{sala} in m^2. Violet and orange dashed lines corresponds to shear/ballistic ($\nu = 2$) and linear diffusion ($\nu = 1$) regimes respectively.

Figure 8 shows the particle size-averaged relative dispersion (D^2_{sa}) of each cloud initially located along the main diagonal of the cavity. Due to near zero average velocities in the center of the cavity the green cloud initially located at the center takes longer to initiate dispersion, reaching the highest rate of dispersion around 40 s after the release. Clouds located close to the center of the main diagonal exhibit asymmetric behavior. During the initial 10 seconds, the cyan cloud exhibits the highest rate of relative dispersion, surpassing the dispersion rates of the rest of the clouds. While the yellow cloud dispersion surpasses only the green cloud dispersion rate. This indicates

the presence of inhomogeneities in the recirculating flow pattern. Both clouds, yellow and cyan, which initially were located to the left and right from the green cloud, reach dispersion rate close to the ballistic regime at ~25 s. The rate of particle relative dispersion of the cyan cloud is similar to the clouds located in the corners of the cavity (red and blue). Both clouds initially located in the opposite corners of the room exhibit similar pattern, with rapid growth of relative dispersion starting from 3 s. These clouds show a plateau between 25 and 60 s. This is a consequence of the large-scale recirculation advecting the spherical-like clouds along the horizontal walls of the cavity until particle clouds reach vertical walls, here their shapes flatten, taking on a disc-like form. As a result, the average distance between particle pairs does not increase, contributing to the observed intermediate plateau in the plot of the particle relative dispersion. This phenomenon hinders particle dispersion for some time and accounts for the characteristic behavior seen in the relative dispersion plot (Fig. 8). The cyan sphere does not exhibit this pattern, showing continuous growth. Because of this, the first particle cloud to reach the uniform distribution is cyan, it takes 300 s, while the red, blue and green clouds require 200 s more. All the clouds disperse at a rate between the shear/ballistic and linear regimes, and at a certain point in time, they reach a transition point where the diffusion rate reaches its maximum and subsequently slows down.

The temporal evolution of the size and the location-averaged particle relative dispersion (D^2_{sala}) shown with black thick dashed line in Fig. 8 (subscript *sala* stands for size and location averaged value). The plot can be divided into three distinct stages. The first stage, which spans the initial 10 s, is characterized by the capturing of particles by the flow. In the second stage, there is a rapid growth in the distance between the particles in the clouds, reaching the maximum dispersion rate at 30 s. The third stage commences after the transition point, dispersion rate is following the linear regime ($\nu = 1$), and gradually slows down, until the particles achieve a homogeneous distribution within the room at 500 s.

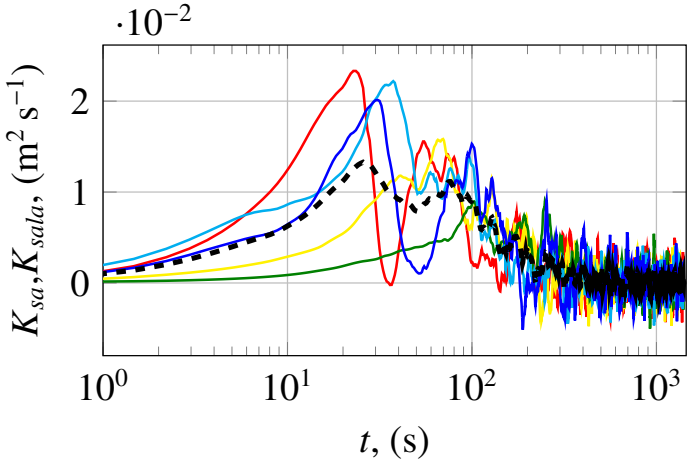

Figure 9: Temporal evolution of the relative diffusivity K_{sa} in m^2 s^{-1} averaged over particle sizes for each position, for color definition see Table 1 and averaged temporal evolution of the relative diffusivity K_{sala} in m^2 s^{-1} averaged over particle sizes and positions is plotted using thick black dashed line.

We computed the size-averaged particle relative diffusivity ($K_{sa}(t)$) using time evolution of the

size-averaged particle relative dispersion ($D^2_{sa}(t)$) and Eq. 14. Figure 9 shows relative diffusivity (K_{sa}) of each cloud, which initial positions with colors defined in Table 1. The black thick dashed line corresponds to the size and location averaged particle relative diffusivity (K_{sala}). The red, blue, and cyan clouds reach their maximum diffusion rates within the time interval of approximately 20 to 40 s. However, due to the effect the cavity walls, the relative diffusivities of the red and blue clouds experience a rapid decline, exhibiting a local minimum, and then subsequently increases again, displaying a local maximum at 50 s for the red cloud and 100 s for the blue cloud. Nature of this phenomenon were already explained (See Fig. 8). In contrast, the remaining particle clouds (cyan, yellow, and green) exhibit continuous growth in their relative diffusivity until they reach their respective maximum rates at 30, 70, and 100 s. After reaching their maximum values, the relative diffusivity of these clouds starts to decline. From 500 s onwards, the rate of relative dispersion fluctuates around zero. The time-averaged dispersion coefficient for each sphere is provided in Table 1.

The averaged temporal evolution of the relative diffusivity averaged over particle sizes shown in Fig.9 exhibits a rapid increase in relative diffusivity immediately after the release of particles, peaking at approximately 25 s with value of $K_{sala} = 0.013$ m^2 s^{-1}. Subsequently, it decreases and reaches a local minimum at around 50 s, followed by another growth phase up to approximately 70 s, where it reaches a local maximum. However, after reaching the local maximum, the relative diffusivity experiences a rapid decline, exhibiting fluctuations. Around 500 s, the relative diffusivity reaches a statistically stable state, fluctuating around zero.

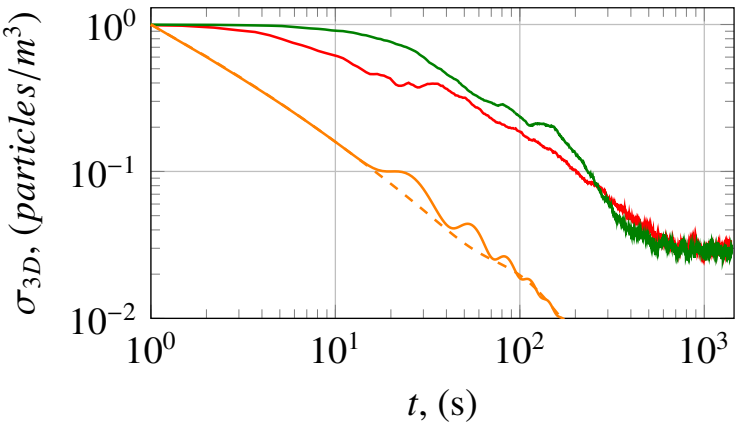

Figure 10: Temporal evolution of the three-dimensional variance of particle concentration (σ_{3D}) for each initial position and averaged over all particle sizes. DNS results are plotted with red for the cloud located at [-0.4, -0.4, -0.4] and for the cloud located at [-0.0, -0.0, -0.0], model results are shown with orange line, dashed line corresponds to $u_c = 0.021$ m s^{-1} and solid line to $u_c = 0.105$ m s^{-1}

To compare the dispersion predicted by the DNS with that of the analytical models, we use the variance of the particle concentration as a measure of the dispersion process. To facilitate a comparison the cavity is divided into $5^3 = 125$ equal square bins. We track particle count in each bin, then, by utilizing Eq.15, we compute the variance of particle concentration, and the results are shown in Fig. 10. On the other hand, Fig. 11 shows the 2D variance of particle concentration,

obtained from Lau et al. [27] model, where dispersion is considered only in two dimensions. To compare the results with the DNS, in this case the cavity is divided into $5^2 = 25$ equal rectangular bins from the top-down (x-z) plane, and the particle count in each bin is tracked over time.

Fig. 10 shows the temporal evolution of the three-dimensional variance of particle concentration(σ_{3D}) of the DNS for a cloud located in the corner (red) and the center (green) averaged over all particle sizes. The predictions of the analytical models are plotted with orange color. The solid orange line represents the model results with a velocity (u_c) of 0.105 m s^{-1} which is close to maximum time-averaged velocity in the cavity, while the dashed orange line represents the results with a (u_c) of 0.021 m s^{-1} which corresponds to overall mean air velocity in the room. The dispersion rate predicted by the model appears to be unaffected by changes in velocity. According to the model, the particle concentration variance reaches value of $\sigma_{3D} = 10^{-2}$ $particles/m^3$ at $t = 168$ s, while the DNS particle concentration variance reaches value of $\sigma_{3D} = 8.5 \times 10^{-2}$ $particles/m^3$ and stagnates after 500 s.

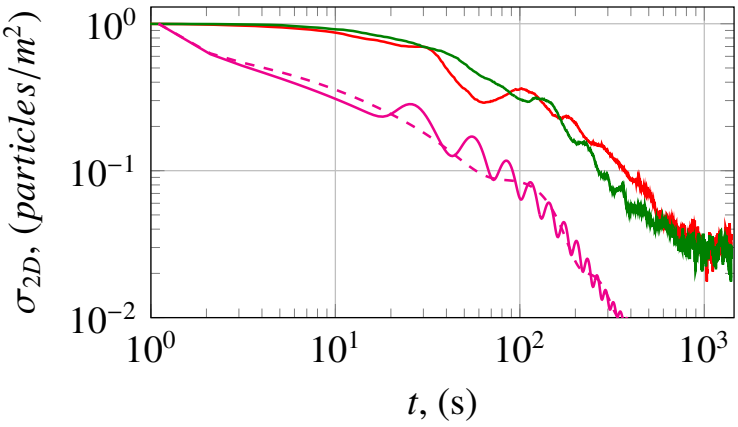

Figure 11: Temporal evolution of the two-dimensional variance of particle concentration (σ_{2D}) for each initial position and averaged over all particle sizes. DNS results are plotted with red for the cloud located at [-0.4, -0.4, -0.4] and with green for the cloud located at [-0.0, -0.0, -0.0], model results shown with magenta line, solid line $u_c = 0.105$ and dashed line $u_c = 0.021$

In Fig. 11, the time-dependent evolution of the two-dimensional variance of particle concentration (σ_{2D}) of the DNS results for corner red particle cloud, averaged over all particle sizes. It is shown along with the analytical model in magenta. The dashed magenta line represents the analytical model proposed by Lau et al. [27] with $u_c = 0.021$ m s^{-1}, while the solid magenta line corresponds to $u_c = 0.105$ m s^{-1}. According to the Lau et. al. [27] model, particle concentration variance $\sigma_{2D} = 10^{-2}$ $particles/m^3$ at $t = 360$ s, but the DNS results indicate that it takes approximately t = 800 - 900 s to achieve even particle concentration in the room.

4. Discussion

The dispersion analysis reveals notable differences between the Lau et al. [27] model and the DNS results. The Lau et al. model takes approximately 360 s to reach a dispersion value of

$\sigma_{2D} = 10^{-2}\ particles/m^2$, whereas the DNS simulation achieves homogeneus particle distribution state around 900 s. On the other hand, the model presented in Eq. 7 achieves a similar dispersion value at around 168 s, while the DNS simulation reaches this state at approximately 500 s.

Comparing the 2D and 3D approaches of the DNS results highlights that achieving a homogeneous distribution occurs faster in the 3D case. This disparity suggests that the dispersion behavior predicted by the 2D approach is inaccurate. The results unequivocally demonstrate the failure of the 2D dispersion model to accurately predict the dispersion process. While both analytical models fall short of providing reliable predictions compared to the DNS, the 3D approach in model Eq. 7 yields better results.

Indeed, the DNS simulation offers more accurate predictions of the particle dispersion process within the room compared to the analytical models. The overprediction of the dispersion rate of the analytical models can be attributed to their simplifications, such as assuming a homogeneous and isotropic environment, a constant dispersion coefficient, and neglecting the impact of turbulent eddies on particle dispersion. By considering these simplifications, the analytical models may fail to capture the intricacies of the actual dispersion process, leading to discrepancies with the DNS results.

Upon investigating the effect of velocity in the Gaussian models, it becomes evident that the dispersion rate remains independent of velocity. This conclusion is supported by analyzing Eqs. 7 and 10, where it is observed that the dispersion rate is solely influenced by the dispersion coefficient, while the velocity merely determines the spatial location of the aerosol cloud.

From Fig. 8 and Table 1, it can be observed that the cyan particle cloud reaches homogeneous dispersion faster compared to other clouds, while the red corner clouds has the largest dispersion coefficient. There is a inconsistency between the two results due to the calculation of K. In Table 1, the value of K is determined based on the relative diffusivity until the time corresponding to the overall maximum value of temporal diffusivity, which on average occurs at around 25 s after the release of the clouds.

5. Conclusion

To better understand the capacity of confined turbulent flows to disperse and homogenize aerosol patches, like those generated during a person's cough or sneeze, we conducted fully-resolved simulations of spherical particle clouds with different particle sizes in a buoyancy-driven turbulent flow in a cubic cavity. The results indicate that the time required to achieve fully mixed conditions depends on the initial location of the cloud. However, the dispersion rate, as measured by relative dispersion and the predictions of variance of particle concentration, remains consistent across the numerical experiments.

The comparison of the DNS results with simplified analytical models reveals that the latter significantly overpredict the rate of dispersion when compared to the fully-resolved simulations.

Both models fail to accurately replicate DNS results. However, our newly developed model, which adopts a 3D approach that aligns more closely with real-world conditions, indicates that the cloud's variance is expected to converge to values similar to those observed in DNS at approximately 168 s. In contrast, the DNS predicts fully mixed conditions after 500 s. On the other hand,

the 2D model proposed by Lau et al. [27] indicates that the aerosol cloud would become evenly dispersed in the room after 360 s. In contrast, in a 2D approach, DNS predicts that particles would take 800-900 s to become evenly dispersed after their release. The discrepancy between the simplified models and the DNS results underscores the need for more sophisticated models that can accurately capture the complex dynamics of aerosol dispersion in confined turbulent flows.

Overall, these results provide insights into the dynamics of particle dispersion in a closed room by the action of buoyancy-driven turbulent flow at $Ra = 3.6 \times 10^9$ and highlight presence of non homogeneous flow with time and space dependent dispersion coefficient. The observed temporal evolution of relative dispersion, relative diffusivity, 3D and 2D variance can be used to validate analytical models and improve our understanding of the physical processes involved in particle cloud dispersion. Our findings underscore the limitations of current analytical models and its inability to give reliable and physical results. Our study emphasizes that despite the simple geometry and mechanism of action, buoyancy-driven flow in the cubical cavity is a complex three-dimensional phenomenon characterized by large-scale recirculation patterns with the presence of local instabilities arising from turbulence. These findings highlight the significance of undertaking additional research in this field and the necessity of developing novel, efficient and computationally cheap methods for modeling these processes.

Conflict of interest

All authors declared no conflicts of interest.

Acknowledgments

We would like to extend our sincere appreciation to Andrew Poje for his valuable insights and comments, which have greatly enriched the quality of this manuscript.

This study was funded by the Spanish Ministerio de Ciencia e Innovacion through the grants PID2020-113303 GB-C21 and RTI2018- 100907-A-I00 (MCIU/AEI/FEDER) and by the Generalitat de Catalunya through the grant 2021 SGR 00732.

6. Appendix A

The particle transport model, described by Eqs. (4)-(5), incorporates five distinct forces acting on the particles: hydrodynamic drag, lift, buoyancy, thermophoresis, and Brownian motion. In this study, the one-way coupling approach is utilized, assuming that the dispersed phase exerts no influence on the momentum conservation of the carrier phase. This assumption remains valid when dealing with small particles and dilute systems, where the contributions of the dispersed phase to the carrier phase's momentum conservation can be considered negligible.

6.0.1. Drag

Hydrodynamic drag accounts for the fluid resistance or friction a particle experiences as it moves with respect to the carrier phase. The hydrodynamic drag can be characterized by the particle Stokes number defined as the ratio of the particle and flow characteristic times. Small

St_p are associated to particles that rapidly react to changes in accelerations in the underlying flow while large Stokes are found in inertia-dominated particles. The Stokes number for a particle of diameter $\tilde{d}_p$ can be written as:

$$St_p = \frac{d_p^2}{18C_c}\frac{\rho_p}{\mu_f}u_s\, l_s \tag{17}$$

where ρ_p is the particle density, C_c is the Cunningham correction factor

$$Kn = \frac{2\lambda}{\tilde{d}_p} \tag{18}$$

$$C_c = 1 + Kn\left[1.205e^{-0.0026/Kn} + 0.425e^{-0.7400/Kn}\right] \tag{19}$$

where $d_p = \tilde{d}_p/l_s$ is the non-dimensional particle diameter and $\lambda = 6.8 \times 10^{-8}$ m is the free mean path in air at T_0 [42].

6.0.2. Buoyancy (weight)

The magnitude of the buoyancy force experienced by a particle within a fluid with different density under a gravitational field with acceleration magnitude $g = 9.81\mathrm{m\,s^{-2}}$ can be written as:

$$n_g = -g\left(1 - \frac{\rho_f}{\rho_p}\right)\frac{l_s}{u_s^2}. \tag{20}$$

6.0.3. Thermophoresis

Thermophoresis is the force due to gradients in the temperature field across the particle characteristic length. The pre-factor of the non-dimensional temperature gradient, n_{th}, is defined as [43]:

$$n_{th} = -18\frac{K_{tp}}{d_p^2}\frac{\nu_f^2}{\widetilde{T}_0}\frac{\rho_f}{\rho_p}\frac{T_s}{l_s^2 u_s^2} \tag{21}$$

where the factor K_{tp}, defined as,

$$K_{tp} = \frac{2C_s\left(k_f + 2k_pKn\right)\left[1 + 2Kn\left(1.2 + 0.41\exp\left(-0.44/Kn\right)\right)\right]}{\left(1 + 6C_mKn\right)\left(2k_f + k_p + 4k_pC_tKn\right)}, \tag{22}$$

contains three constant set to $C_s = 1.17$, $C_m = 1.14$ and $C_t = 2.18$. Note that the negative sign in n_{th} indicates that the force points in the direction of maximal temperature decay.

6.0.4. Lift

The hydrodynamic force acts perpendicular to the flow direction and is proportional to the cross product of the velocity difference between the two phases and the local vorticity in the carrier phase. The proportionality factor has the form

$$n_l = C_L\frac{\rho_f}{\rho_p} \tag{23}$$

where the lift coefficient C_L is defined as [44]:

$$C_L = \left[5.816\sqrt{\frac{Sr_p}{2Re_p}} - 0.875\frac{Sr_p}{2}\right]\frac{3}{4Sr_p}\frac{J(\varepsilon)}{2.255} \tag{24}$$

where the particle Reynolds number is Re_p, particle Strouhal number is Sr_p, ε and J are determined using the relations:

$$Re_p = \left|u_i^* - u_i\right| d_p Re, \tag{25}$$

$$Sr_p = \frac{\left|\epsilon_{ijk}\left[u_j^* - u_j\right]\omega_k\right|}{\left|u_j^* - u_j\right|^2} d_p, \tag{26}$$

$$\varepsilon = \sqrt{\frac{Sr_p}{Re_p}}, \tag{27}$$

$$J(\varepsilon) = 0.6765\left\{1 + \tanh\left[2.5\log_{10}(\varepsilon + 0.191)\right]\right\}\left\{0.677 + \tanh\left[6(\varepsilon - 0.32)\right]\right\}. \tag{28}$$

6.0.5. Brownian

For small enough particles, the net force due to molecular vibrations may not be negligible and, therefore, contribute to the transport. This Browninan force takes the form [45]:

$$n_i(t) = Z_i\sqrt{\frac{2\pi}{\Delta t}216\frac{\rho_f}{\rho_p^2}\frac{k_B\widetilde{T}_0\nu_f}{d_p^5\pi^2 C_c}\frac{\widetilde{t}^3}{\widetilde{l}^7}} \tag{29}$$

where Z_i is independent zero-mean Gaussian random number, $k_B = 1.38064852 \times 10^{-23}\ \mathrm{J\,K^{-1}}$ is the Boltzmann constant.

6.1. Settling velocity

To gain insight into the role played by the flow hydrodinamics on the wall deposition, the deposition rate is often compared with the settling velocity, v_s. This quantity is determined by assuming that the only forces acting on a particle suspended in a quiescent fluid are drag and buoyancy. Simplifying Eqs. (5), the expression for v_s yields

$$v_s = St_p n_g \delta_{i2}. \tag{30}$$

6.2. Exponential-Lagrangian Tracking Schemes

Eqs. (4) and (5) are temporally integrated using Exponential-Lagrangian Tracking Schemes (ELTS) [46]. ELTS are inherently stable and offer, at least, $O(\Delta t^2)$ local truncation errors depending on the application. Details on the ELTS temporal discretization can be found in [36].

7. Appendix B

In this section, we reproduce derivation of the model proposed by Lau et al. [27] and discuss the key assumptions. Authors have developed a quasi-three-dimensional spatio-temporal model that is quick to run and predicts the concentration of viral aerosols indoors with semi-analytic solution. The model considers an infectious person speaking or breathing and assumes the presence of an air-conditioning unit in the room, driving a recirculating flow, see Fig. 12a.

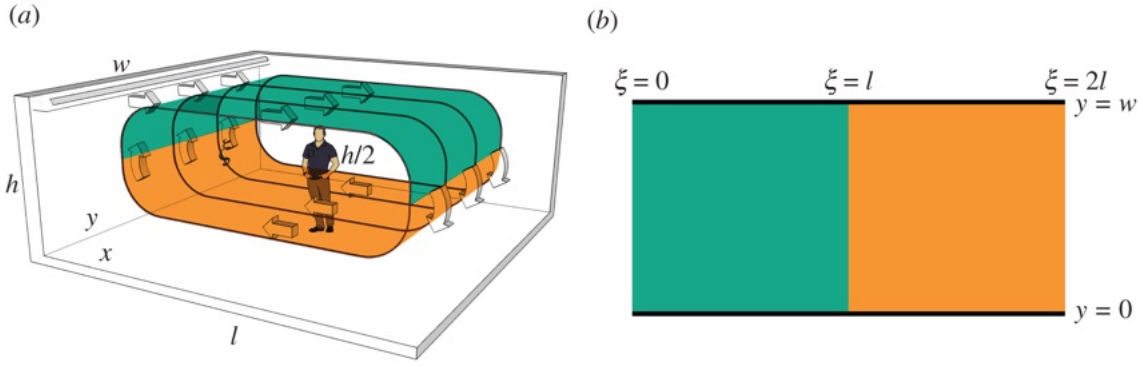

Figure 12: Sketch of the computational domain. Figure is taken from the paper by Lau Zechariah, Griffiths Ian M., English Aaron and Kaouri Katerina 2022 Predicting the spatio-temporal infection risk in indoor spaces using an efficient airborne transmission modelProc. R. Soc. A.4782021038320210383 http://doi.org/10.1098/rspa.2021.0383, Figure 2.

The infectious person acts as a continuous source of infectious aerosols, S_{inf}, all aerosols are of the same size and carry the same amount of virus. The aerosols are transported by advection caused by the airflow, which follows the recirculating loop and has velocity u. The aerosols are passively released into the flow stream, so that the advection velocity of the aerosols is also u. The infectious aerosols are assumed to be removed due to three factors: ventilation, biological deactivation of the virus, and gravitational settling. These correspond to sink terms, which are denoted by S_{vent}, S_{deact}, and S_{set}, respectively.

Finally, it assumes turbulent mixing of the air. Turbulence leads to the aerosols diffusing much more rapidly than due to Brownian motion. Turbulent diffusion is governed by the eddy diffusion coefficient, K (m^2/s). From these assumptions, we arrive at the advection-diffusion-reaction (ADR) equation, the governing equation for the concentration of infectious aerosols:

$$\frac{\partial C}{\partial t} + \nabla \cdot (uC) - \nabla \cdot (K \nabla C) = S_{inf} - S_{vent} - S_{deact} - S_{set} \tag{31}$$

Thus, an infectious person talking or breathing at position (ξ_0, y_0) is modelled as follows:

$$S_{inf} = R\delta(\xi - \xi_0)\delta(y - y_0) \tag{32}$$

where $\delta(x)$ is the Dirac delta function.

Furthermore, it is assumed that there is mechanical ventilation provided by air-conditioning units which models the ventilation effect as a sink term of uniform strength over the domain S_{vent}.

The biological deactivation and gravitational settling are S_{deact} and S_{set} respectively. In our case we consider that there are no air exchange, viral deactivation and settling in the room thus this terms are 0.

The typical airflow from an air-conditioning unit, $u = 0.1 - 1$ m/s, so it is assumed that the air is an incompressible fluid; that is:

$$\nabla \cdot \mathbf{u} = 0 \tag{33}$$

For a room with length l and width w, the loop surface of the airflow is unwrapped to the two-dimensional domain $(\xi, y) \in [0, 2l] \times [0, w]$, see Fig 12b. This extended domain allows to model the evolution of the aerosol cloud in both the upper and lower layers of the flow stream in a simpler way. Assuming there is only one infectious person, equations 31 is substituted into ADR equation 31 to obtain the partial differential equation (PDE), which we will be solving:

$$\frac{\partial C}{\partial t} + u\frac{\partial C}{\partial \xi} - K\left(\frac{\partial^2 C}{\partial \xi^2} + \frac{\partial^2 C}{\partial y^2}\right) = R\delta(\xi - \xi_0)\delta(y - y_0) \tag{34}$$

where $\mathbf{u}$ is the airflow velocity vector, K is the diffusion coefficient.

In the beginning there are no virus-carrying aerosols, hence, the initial condition is:

$$C(\xi, y, 0) = 0 \tag{35}$$

In the set-up the aerosols loop around the room. This is modelled through periodic boundary conditions on the concentration and its derivative at the wall $\xi = 0$ and the opposite side of the extended domain, at $\xi = 2l$. Hence:

$$C(0, y, t) = C(2l, y, t), \tag{36}$$

$$\frac{\partial C}{\partial \xi}(0, y, t) = \frac{\partial C}{\partial \xi}(2l, y, t) \tag{37}$$

The system is closed by applying Neumann boundary conditions at the walls located at $y = 0, w$ as follows:

$$\frac{\partial C}{\partial y}(\xi, 0, t) = \frac{\partial C}{\partial y}(\xi, w, t) = 0 \tag{38}$$

The conditions in equation 38 correspond to perfect reflection of aerosols at the wall.

The PDE shown in Eq. 34 is solved with the boundary conditions in Eq. 38 and initial condition in Eq. 35 by first solving the homogeneous problem to determine the impulse function. Then, the impulse is convolved with the source function Eq. 32. Owing to the periodic and Neumann boundary conditions Eq. 38, method of images could be used when solving for the impulse

function. Hence, the solution is given by:

$$C(\eta, y, t) = \int_0^t \frac{R}{4\pi K t} \sum_{m=-\infty}^{\infty} e^{-\frac{(\eta - ut - \eta_0 - 2ml)^2}{4Kt}} \times \\ \times \sum_{n=-\infty}^{\infty} \left(e^{-\frac{(y - y_0 - 2nw)^2}{4Kt}} + e^{-\frac{(y + y_0 - 2nw)^2}{4Kt}} \right) dt \tag{39}$$

By leveraging the mapping of the quasi-three-dimensional setup to a two-dimensional geometry, the aerosol concentration is averaged in the upper and lower branches of the loop surface to determine the concentration for the quasi-three-dimensional setup. Specifically, it is defined that $x \in [0, l]$ to be the Cartesian coordinate in the direction of the upper flow, so $x = \eta$, $0 \leq \eta \leq l$ defines the upper branch, and $x = 2l - \eta$ defines the lower branch for $l \leq \eta \leq 2l$. The concentration of viral aerosols in the upper branch is then given by:

$$C_{\text{upper}}(x, y, t) = C(x, y, t) \tag{40}$$

and the concentration of viral aerosols in the lower branch is given by:

$$C_{\text{lower}}(x, y, t) = C(2l - x, y, t) \tag{41}$$

The separation between the two branches is half the height of the room. It is assumed that within the two branches, the air is well mixed and it is used to transform the two-dimensional expressions back into a three-dimensional representation:

$$C(x, y, t) = \frac{C_{\text{upper}}(x, y, t) + C_{\text{lower}}(x, y, t)}{2} \cdot \frac{h}{2} \tag{42}$$

Then substitute equation 39 into equation 42 to obtain the total concentration:

$$C(x, y, t) = \frac{2R}{4\pi K h} \int_0^t \sum_{m=-\infty}^{\infty} \left[e^{-\frac{(x - ut - x_0 - 2ml)^2}{4Kt}} + e^{-\frac{(x + ut + x_0 - 2ml)^2}{4Kt}} \right] \times \\ \times \sum_{n=-\infty}^{\infty} \left[e^{-\frac{(y - y_0 - 2nw)^2}{4Kt}} + e^{-\frac{(y + y_0 - 2nw)^2}{4Kt}} \right] \tag{43}$$

References

[1] Khaled Al-Farhany, Mohamed F. Al-dawody, Dhafer A. Hamzah, Wael Al-Kouz, Zafar Said, Numerical investigation of natural convection on Al_2O_3–water porous enclosure partially heated with two fins attached to its hot wall: under the MHD effects, Applied Nanoscience (2021). doi:10.1007/s13204-021-01855-y.

[2] S. Shahzad, M. Sheikholeslami, T. Ambreen, A. Shafee, H. Babazadeh, M. Ahmad, Heat transfer management of hybrid nanofluid including radiation and magnetic source terms within a porous domain, Applied Nanoscience 10 (05 2020). doi:10.1007/s13204-020-01432-9.

[3] G. C. Morrison, P. Zhao, L. Kasthuri, The spatial distribution of pollutant transport to and from indoor surfaces, Atmospheric Environment 40 (20) (2006) 3677–3685. doi:https://doi.org/10.1016/j.atmosenv.2006.03.015.
URL https://www.sciencedirect.com/science/article/pii/S1352231006002901

[4] P. James, A. Stohl, C. Forster, S. Eckhardt, P. Seibert, A. Frank, A 15-year climatology of stratosphere–troposphere exchange with a Lagrangian particle dispersion model 2. Mean climate and seasonal variability, Journal of Geophysical Research: Atmospheres 108 (D12) (2003). doi:https://doi.org/10.1029/2002JD002639.
URL https://agupubs.onlinelibrary.wiley.com/doi/abs/10.1029/2002JD002639

[5] K. Zhang, S. Batterman, Air pollution and health risks due to vehicle traffic, Science of The Total Environment 450-451 (2013) 307–316. doi:https://doi.org/10.1016/j.scitotenv.2013.01.074.
URL https://www.sciencedirect.com/science/article/pii/S0048969713001290

[6] J. Meyerjürgens, M. Ricker, V. Schakau, T. H. Badewien, E. V. Stanev, Relative dispersion of surface drifters in the north sea: The effect of tides on mesoscale diffusivity, Journal of Geophysical Research: Oceans 125 (8) (2020) e2019JC015925, e2019JC015925 2019JC015925. doi:https://doi.org/10.1029/2019JC015925.
URL https://agupubs.onlinelibrary.wiley.com/doi/abs/10.1029/2019JC015925

[7] I. Manisalidis, E. Stavropoulou, A. Stavropoulos, E. Bezirtzoglou, Environmental and health impacts of air pollution: A review, Frontiers in Public Health 8 (2020). doi:10.3389/fpubh.2020.00014.
URL https://www.frontiersin.org/articles/10.3389/fpubh.2020.00014

[8] A. Drescher, Computer tomography and optical remote sensing: Development for the study of indoor air pollutant transport and dispersion, Ph.D. thesis, Lawrence Berkeley National Laboratory (1995).

[9] M. P. Wan, C. Y. H. Chao, Y. D. Ng, G. N. S. To, W. C. Yu, Dispersion of expiratory droplets in a general hospital ward with ceiling mixing type mechanical ventilation system, Aerosol Science and Technology 41 (3) (2007) 244–258. arXiv:https://doi.org/10.1080/02786820601146985, doi:10.1080/02786820601146985.
URL https://doi.org/10.1080/02786820601146985

[10] L. Morawska, J. W. Tang, W. Bahnfleth, P. M. Bluyssen, A. Boerstra, G. Buonanno, J. Cao, S. Dancer, A. Floto, F. Franchimon, C. Haworth, J. Hogeling, C. Isaxon, J. L. Jimenez, J. Kurnitski, Y. Li, M. Loomans, G. Marks, L. C. Marr, L. Mazzarella, A. K. Melikov, S. Miller, D. K. Milton, W. Nazaroff, P. V. Nielsen, C. Noakes, J. Peccia, X. Querol, C. Sekhar, O. Seppänen, S. ichi Tanabe, R. Tellier, K. W. Tham, P. Wargocki, A. Wierzbicka, M. Yao, How can airborne transmission of COVID-19 indoors be minimised?, Environment International 142 (2020) 105832. doi:https://doi.org/10.1016/j.envint.2020.105832.
URL https://www.sciencedirect.com/science/article/pii/S0160412020317876

[11] Airborne and direct contact diseases.
URL https://www.maine.gov/dhhs/mecdc/infectious-disease/epi/airborne/index.shtml#:~:text=Airborne%20diseases%20are%20caused%20by,particles%2C%20respiratory%20and%20water%20droplets

[12] Coronavirus disease (COVID-19): How is it transmitted?
URL https://www.who.int/news-room/questions-and-answers/item/coronavirus-disease-covid-19-how-is-it-transmitted

[13] COVID-19 CORONAVIRUS PANDEMIC.
URL https://www.worldometers.info/coronavirus/

[14] CDC Public Health Science Agenda for COVID-19.
URL https://www.cdc.gov/coronavirus/2019-ncov/science/science-agenda-covid19.html

[15] Global research on coronavirus disease (COVID-19).
URL https://www.who.int/emergencies/diseases/novel-coronavirus-2019/global-research-on-novel-coronavirus-2019-ncov

[16] J. Shirolkar, C. Coimbra, M. Queiroz McQuay, Fundamental aspects of modeling turbulent particle dispersion in dilute flows, Progress in Energy and Combustion Science 22 (4) (1996) 363–399. doi:https://doi.org/10.1016/S0360-1285(96)00006-8.
URL https://www.sciencedirect.com/science/article/pii/S0360128596000068

[17] A. Gadgil, C. Lobscheid, M. Abadie, E. Finlayson, Indoor pollutant mixing time in an isothermal closed room:

an investigation using cfd, Atmospheric Environment 37 (39) (2003) 5577–5586, indoor Air Chemistry and Physics: Papers from Indoor Air 2002. doi:https://doi.org/10.1016/j.atmosenv.2003.09.032.
URL https://www.sciencedirect.com/science/article/pii/S135223100300774X

[18] N. Klepeis, Modeling human exposure to air pollution (10 2006). doi:10.1201/9781420012637.ch19.

[19] M. Z. Bazant, J. W. M. Bush, A guideline to limit indoor airborne transmission of COVID-19, Proceedings of the National Academy of Sciences 118 (17) (2021) e2018995118. arXiv:https://www.pnas.org/doi/pdf/10.1073/pnas.2018995118, doi:10.1073/pnas.2018995118.
URL https://www.pnas.org/doi/abs/10.1073/pnas.2018995118

[20] M. Auvinen, J. Kuula, T. Grönholm, M. Sühring, A. Hellsten, High-resolution large-eddy simulation of indoor turbulence and its effect on airborne transmission of respiratory pathogens—Model validation and infection probability analysis, Physics of Fluids 34 (1), 015124 (01 2022). arXiv:https://pubs.aip.org/aip/pof/article-pdf/doi/10.1063/5.0076495/16624013/015124_1_online.pdf, doi:10.1063/5.0076495.
URL https://doi.org/10.1063/5.0076495

[21] J. Szoplik, M. Ciuksza, Mixing time prediction with artificial neural network model, Chemical Engineering Science 246 (2021) 116949. doi:https://doi.org/10.1016/j.ces.2021.116949.
URL https://www.sciencedirect.com/science/article/pii/S0009250921005145

[22] A. Fabregat, F. Gisbert, A. Vernet, S. Dutta, K. Mittal, J. Pallares, Direct numerical simulation of the turbulent flow generated during a violent expiratory event, Physics of Fluids 33 (2021) 035122. doi:10.1063/5.0042086.

[23] A. Fabregat, F. Gisbert, A. Vernet, J. A. Ferré, K. Mittal, S. Dutta, J. Pallarès, Direct numerical simulation of turbulent dispersion of evaporative aerosol clouds produced by an intense expiratory event, Physics of Fluids 33 (3) (2021) 033329. doi:10.1063/5.0045416.

[24] A. Lavrinenko, A. Fabregat, J. Pallares, Comparison between fully resolved and time-averaged simulations of particle cloud dispersion produced by a violent expiratory event, Acta Mechanica Sinica 38 (8) (2022). doi:10.1007/s10409-022-09032-x.

[25] J. Pallares, A. Fabregat, A. Lavrinenko, H. A. bin Norshamsudin, G. Janiga, D. F. Fletcher, K. Inthavong, M. Zasimova, V. Ris, N. Ivanov, R. Castilla, P. J. Gamez-Montero, G. Raush, H. Calmet, D. Mira, J. Wedel, M. Štrakl, J. Ravnik, D. Fontes, F. J. de Souza, C. Marchioli, S. Cito, Numerical simulations of the flow and aerosol dispersion in a violent expiratory event: Outcomes of the "2022 International Computational Fluid Dynamics Challenge on violent expiratory events", Physics of Fluids 35 (4), 045106 (04 2023). arXiv:https://pubs.aip.org/aip/pof/article-pdf/doi/10.1063/5.0143795/16829566/045106_1_5.0143795.pdf, doi:10.1063/5.0143795.
URL https://doi.org/10.1063/5.0143795

[26] A. V. Baughman, A. J. Gadgil, W. W. Nazaroff, Mixing of a point source pollutant by natural convection flow within a room, Indoor Air 4 (2) 114–122. doi:https://doi.org/10.1111/j.1600-0668.1994.t01-2-00006.x.
URL https://onlinelibrary.wiley.com/doi/abs/10.1111/j.1600-0668.1994.t01-2-00006.x

[27] Z. Lau, I. M. Griffiths, A. English, K. Kaouri, Predicting the spatio-temporal infection risk in indoor spaces using an efficient airborne transmission model, Proceedings of the Royal Society A: Mathematical, Physical and Engineering Sciences 478 (2259) (2022) 20210383. doi:10.1098/rspa.2021.0383.
URL https://royalsocietypublishing.org/doi/abs/10.1098/rspa.2021.0383

[28] A. Lavrinenko, F. Gisbert, J. Pallares, A. Fabregat, Fully-resolved numerical simulations of the turbulent flow and particle deposition in a cubical cavity with two pairs of differentially heated opposed walls at rayleigh number 3.6×10^9, International Communications in Heat and Mass Transfer 141 (2023) 106564. doi:https://doi.org/10.1016/j.icheatmasstransfer.2022.106564.
URL https://www.sciencedirect.com/science/article/pii/S0735193322006868

[29] P. F. Fischer, J. W. Lottes, S. G. Kerkemeier, Nek5000.
URL http://nek5000.mcs.anl.gov

[30] A. Deville, MO, A. Fischer, PF, A. Mund, EH, R. Gartling, DK, High-Order Methods for Incompressible Fluid Flow, Applied Mechanics Reviews 56 (3) (2003) B43–B43. arXiv:https://asmedigitalcollection.asme.org/appliedmechanicsreviews/article-pdf/56/3/B43/5439822/b34_1.pdf, doi:10.1115/1.1566402.

URL https://doi.org/10.1115/1.1566402

[31] K. Mittal, S. Dutta, P. Fischer, Multirate timestepping for the incompressible navier-stokes equations in overlapping grids, Journal of Computational Physics 437 (2021) 110335. doi:https://doi.org/10.1016/j.jcp.2021.110335.
URL https://www.sciencedirect.com/science/article/pii/S0021999121002308

[32] A. Fabregat Tomàs, A. C. Poje, T. M. Özgökmen, W. K. Dewar, Dynamics of multiphase turbulent plumes with hybrid buoyancy sources in stratified environments, Physics of Fluids 28 (9) (2016) 095109. arXiv:https://doi.org/10.1063/1.4963313, doi:10.1063/1.4963313.
URL https://doi.org/10.1063/1.4963313

[33] E. Merzari, A. Obabko, P. Fischer, Spectral element methods for liquid metal reactors applications (2017). doi:10.48550/ARXIV.1711.09307.
URL https://arxiv.org/abs/1711.09307

[34] R. Vinuesa, P. Negi, M. Atzori, A. Hanifi, D. Henningson, P. Schlatter, Turbulent boundary layers around wing sections up to rec=1,000,000, International Journal of Heat and Fluid Flow 72 (2018) 86–99. doi:https://doi.org/10.1016/j.ijheatfluidflow.2018.04.017.
URL https://www.sciencedirect.com/science/article/pii/S0142727X17311426

[35] J. Scheel, S. Emran, J. Schumacher, Resolving the fine-scale structure in turbulent Rayleigh-Benard convection, New Journal of Physics 15 (11 2013). doi:10.1088/1367-2630/15/11/113063.

[36] A. Fabregat, J. Pallarès, Heat transfer and boundary layer analyses of laminar and turbulent natural convection in a cubical cavity with differently heated opposed walls, International Journal of Heat and Mass Transfer 151 (2020) 119409. doi:https://doi.org/10.1016/j.ijheatmasstransfer.2020.119409.
URL https://www.sciencedirect.com/science/article/pii/S001793101935731X

[37] J. H. Seinfeld, S. N. Pandis, Atmospheric Chemistry and Physics: From Air Pollution to Climate Change, Wiley, 2016.

[38] P. Drivas, P. Valberg, B. Murphy, R. Wilson, Modeling indoor air exposure from short-term point source releases, Indoor Air 6 (2004) 271 – 277. doi:10.1111/j.1600-0668.1996.00006.x.

[39] L. F. Richardson, Atmospheric diffusion shown on a distance-neighbour graph, Proceedings of the Royal Society of London. Series A, Containing Papers of a Mathematical and Physical Character 110 (756) (1926) 709–737. arXiv:https://royalsocietypublishing.org/doi/pdf/10.1098/rspa.1926.0043, doi:10.1098/rspa.1926.0043.
URL https://royalsocietypublishing.org/doi/abs/10.1098/rspa.1926.0043

[40] B. Shivamoggi, Relative particle dispersion in two-dimensional and quasi-geostrophic turbulence, Physica A: Statistical Mechanics and its Applications 529 (2019) 121546. doi:https://doi.org/10.1016/j.physa.2019.121546.
URL https://www.sciencedirect.com/science/article/pii/S0378437119309100

[41] Wikipedia contributors, Variance — Wikipedia, The Free Encyclopedia (Accessed 2023).
URL https://en.wikipedia.org/wiki/Variance

[42] M. D. Allen, O. G. Raabe, Slip correction measurements of spherical solid aerosol particles in an improved millikan apparatus, Aerosol Science and Technology 4 (3) (1985) 269–286. arXiv:https://doi.org/10.1080/02786828508959055, doi:10.1080/02786828508959055.
URL https://doi.org/10.1080/02786828508959055

[43] L. Talbot, R. K. Cheng, R. W. Schefer, D. R. Willis, Thermophoresis of particles in a heated boundary layer, Journal of Fluid Mechanics 101 (4) (1980) 737–758. doi:10.1017/S0022112080001905.

[44] J. B. McLaughlin, Inertial migration of a small sphere in linear shear flows, Journal of Fluid Mechanics 224 (1991) 261–274. doi:10.1017/S0022112091001751.

[45] H. Ounis, G. Ahmadi, J. B. McLaughlin, Brownian particle deposition in a directly simulated turbulent channel flow, Physics of Fluids A: Fluid Dynamics 5 (6) (1993) 1427–1432. arXiv:https://doi.org/10.1063/1.858578, doi:10.1063/1.858578.
URL https://doi.org/10.1063/1.858578

[46] I. E. Barton, Exponential-lagrangian tracking schemes applied to stokes law, Journal of Fluids Engineering 118 (1996) 85–89.

UNIVERSITAT ROVIRA I VIRGILI
NUMERICAL SIMULATIONS OF PARTICLE TURBULENT DISPERSION AND
DEPOSITION WITH IMPLICATIONS FOR THE SPREADING OF AIRBORNE DISEASES
Akim Lavrinenko

Chapter 5

Fully-resolved numerical simulations of the turbulent flow and particle deposition in a cubical cavity with two pairs of differentially heated opposed walls at Rayleigh number 3.6×10^9

International Communications in Heat and Mass Transfer 141 (2023) 106564

Contents lists available at ScienceDirect

International Communications in Heat and Mass Transfer

journal homepage: www.elsevier.com/locate/ichmt

Fully-resolved numerical simulations of the turbulent flow and particle deposition in a cubical cavity with two pairs of differentially heated opposed walls at Rayleigh number 3.6×10^9

Akim Lavrinenko *, Ferran Gisbert, Jordi Pallares, Alexandre Fabregat

Universitat Rovira i Virgili, Departament d`Enginyeria Mecanica, Av. Països Catalans 26, Tarragona 43007, Catalonia, Spain

ARTICLE INFO

Keywords:
Turbulent mixing
Direct Numerical Simulation
Dispersed multiphase flows
Particle wall deposition
Natural convection
Cubical cavity

ABSTRACT

The turbulent dispersion and deposition of airborne solid particles is studied by means of fully-resolved numerical simulations. The computational domain, consisting in a cubical cavity with differentially heated opposed walls filled with air, reproduces the experimental conditions of measurements previously reported in the literature. The computational model assumes that each solid spherical particle trajectory is governed by the balance between hydrodynamic drag, buoyancy, lift, thermophoresis and Brownian forces. The dominant terms responsible for particle deposition mostly depend on the particle size, the solid–gas density ratio and the hydrodynamics within the thermal and momentum boundary layers near the solid surfaces. The present results suggest that previous correlations for the wall-averaged Nusselt number as a function of Rayleigh number over the range between 10^7 and 5.4×10^8 can be extended up to Rayleigh number 3.6×10^9. Also, numerical predictions of the particle deposition rates on thermally active surfaces are in good agreement with both experimental data and analytical boundary layer solutions for particle sizes ranging between 0.1 μm and 2.5 μm in diameter. These particle sizes allows to study different particle deposition regimes varying from that controlled by thermophoresis (0.1 μm) to that dominated by gravitational forces (2.5 μm).

1. Introduction

The present work aims to simultaneously delve into two relevant problems that have garnered significant amount of both numerical and experimental efforts, namely, airborne particle dispersion and turbulent natural convection in enclosed domains. Combined or independently, both topics are of relevance in a wide range of applications including airborne transmission of infectious diseases [1,2], valuable surface soiling [3], formation of blood vessel occlusions [4], oceanic and atmospheric pollutant transport [5], nuclear power plant safety [6] and heat transfer equipment design [7] to mention a few.

Regarding buoyancy-driven flows in enclosed domains, when the Rayleigh number is large enough, even simple geometries consisting in cavities with differentially heated walls exhibit complex flow dynamics characterized by large-scale and coherent circulating structures and non-isotropic small-scale turbulence associated to the presence of momentum and thermal boundary layers in the near-wall regions [8]. Prototypical flow configurations enclosed in parallelepipedic or cylindrical domains and their variants in terms of cavity geometry and thermal wall arrangement have been the subject of both computational and experimental investigations. In their exhaustive review on turbulent natural convection in rectangular cavities, Miroshnichenko and Sheremet [9] concluded that gaining insight into strategies and mechanism to enhanced turbulent heat transfer is crucial given the overwhelmingly large number of real-world applications. The laminar natural convection flows were investigated by Pandey et al. [10] who summarized existing numerical and experimental studies in several types of enclosures with and without internal bodies. Likewise, Abdulkadhim et al. [11] examined natural convection works addressed to investigate more complex geometries.

In this study we focus our attention on the enclosed flow bounded by two pairs of differentially heated opposed walls. This flow configuration was investigated by Shiralkar and Tien [12] who numerically studied the circulating flow in a squared two dimensional (2D) cavity at several Rayleigh numbers (Ra) between 10^3 and 10^6. These authors reported that the numerically predicted streamline patterns were in good qualitative agreement with the experiments by Ostrach and Raghavan [13]. Corcione [14], who numerically studied heat transfer in 2D rectangular enclosures, reported dimensionless correlations and distributions of

* Corresponding author.
E-mail address: akim.lavrinenko@urv.cat (A. Lavrinenko).

https://doi.org/10.1016/j.icheatmasstransfer.2022.106564
Received 9 September 2022; Received in revised form 8 November 2022; Accepted 4 December 2022
Available online 23 December 2022

Nomenclature

Symbols

Ra	Rayleigh number
Nu	Nusselt number
T	temperature
l	length
t	time
u_i	i-th direction velocity
u	velocity
p	pressure
Pr	Prandtl number
g	gravitational acceleration
x_i^*	i-th particle position
u_i^*	i-th particle velocity
St	Stokes number
Sr	Strouhal number
n_g	particle buoyancy force magnitude
n_{th}	prefactor of non-dimensional temperature gradient
n_l	lift proportionality factor
n_i	Brownian force
d	diameter
C_c	Cunningham correction factor
Kn	Knudsen number
C_s	thermal slip coefficient
C_m	momentum exchange coefficient
C_t	numerical factor
k_i	thermal conductivity for phase i
C_L	lift coefficient
Re	Reynolds number
Z_i	independent zero-mean Gaussian random number
k_B	Boltzman constant
v_s	settling velocity
k	kinetic energy
V	volume
v_d	deposition velocity
N	total number of particles
N_d	number of deposited particles
A_d	area of the wall for particle deposition
M_s	total deposited mass of particles
$\langle C \rangle$	bulk concentration of suspended particles
$\langle \cdot \rangle$	time-averaged value

Greek symbols

Δ	increment
ν	kinematic viscosity
α	thermal diffusivity
β	thermal expansion coefficient
ρ	density
δ_{ij}	Kronecker delta
ε_{ijk}	Levi-Civita symbol
ω	vorticity
λ	air free mean path
ε	kinetic energy dissipation
τ	temporal scale

Subscripts

vert	vertical
hor	horizontal
0	reference value
p	particle
f	fluid
s	scale
h	hot walls
c	cold walls
m	m-th cavity wall
l, r	left and right cavity walls
b, t	bottom and top cavity walls
q, d	front and back cavity walls

Superscript

$\tilde{a}$	dimensional value
$\overline{a}$	volume-averaged value
$\widehat{a}$	wall-averaged value

vertical and horizontal wall Nusselt number (Nu) versus Ra in the range between 10^3 and 10^6. Danis et al. [15] used the Smoothed Particle Hydrodynamics (SPH) technique to investigate the natural convection in a squared 2D cavity over the same Ra number range. The obtained correlation were found to be in agreement with previous studies of the same flow configurations. The algebraic heat flux model proposed by Hanjalic and Vasic [16] was used to investigate the heat transfer in a 2D square cavity over the range $10^{10} \leqslant Ra \leqslant 10^{12}$. The reported Nusselt number for vertical and horizontal walls versus Rayleigh number were in relatively good agreement with the experiments carried out by Kirkpatrick and Bohn [17]. Using Direct Numerical Simulations (DNS), Fabregat and Pallares [18] investigated the heat transfer in a cubical Differentially Heated Cavity (DHC) for both laminar and turbulent regimes over the range $10^5 \leqslant Ra \leqslant 5.4 \times 10^8$ and reported correlations for the wall-averaged Nu on both the vertical and horizontal surfaces.

Regarding the transport of suspended material in fluids, the turbulent dispersion and wall deposition of airborne particles have attracted notable efforts due to their central role in the spreading of toxic or hazardous particulate matter in the environment [19], the fouling of active surfaces in heat exchange equipment [20], and recently, the transmission of infectious diseases including the COVID-19 [21]. When particles are small enough, the capacity of the turbulent air flow driven by thermal gradients to transport suspended particles and their likelihood to land on a solid surface strongly depends on the density ratio between the dispersed and carrier phases, the particle size and local characteristics of the background thermal and hydrodynamic fields. Puragliesi et al. [6] used DNS to investigate particle deposition in a 2D buoyancy-driven flow within a DHC at Ra numbers between 10^9 and 10^{10} using particles with diameters between 15 and 35 μm. Kalilainen et al. [22] experimentally studied the depletion dynamics of 1.0 and 2.5 μm particles inside a DHC at $Ra = 10^9$ with all walls insulated except the two opposing vertical walls that were kept at distinct temperatures. Dehbi et al. [23] used Large-Eddy Simulations (LES) to predict the air flow field and particle dynamics inside a DHC. The particle concentration was found to decay exponentially with time and the computed depletion rate constants were in very good agreement with experimental data for particles with diameters of 1.4 and 3.5 μm [22]. Kim et al. [24] extended the work of Kalilainen et al. [22] and Dehbi et al. [23] by using experiments and LES with wall-to-wall radiation effects and Lagrangian Particle Tracking (LPT). They reported excellent agreement between LES velocity and temperature fields and experimental data. Additionally, Kim et al. [24] investigated particle deposition velocity on thermally active walls providing data on the decay rates in a cubical cavity for different Rayleigh number and particle sizes. Lai et al. [25] investigated the role played by wall rugosity and concluded that the ratio of particle deposition rate on rough surfaces relative to smooth surfaces increased with the particle size and the velocity magnitude of the air flow. The effect of surface roughness was also investigated by Zhong

et al. [26] who reported that non-smooth walls enhanced the overall particle deposition.

Of particular interest is the work of Thatcher et al. [27] who experimentally determined the deposition rate of particles ranging from 0.1 to 2.5 μm onto smooth surfaces at $Ra = 5.4 \times 10^8$ and $Ra = 3.6 \times 10^9$. Using exactly the same flow set-up, Fabregat and Pallares [18,28,29] numerically investigated the hydrodynamics and particle deposition at $Ra = 5.4 \times 10^8$ using DNS coupled with a LPT approach. They proved that the numerical approach can satisfactorily predict the wall-averaged deposition rate and identified preferential deposition locations on the cavity walls.

By extending the analysis of Fabregat and Pallares [18] up to $Ra = 3.6 \times 10^9$, the present study has two goals, namely, (i) to assess the validity of the wall-averaged *Nu* correlation over the range $10^7 \leqslant Ra \leqslant 5.4 \times 10^8$ up to this Rayleigh number, and (ii) to compare the numerical results of wall-average particle deposition rate with the experiments reported by Thatcher et al. [27] and the boundary layer solutions presented in Pallares and Fabregat [28].

The paper is organized as follows: Section 2 contains a description of the physical and mathematical models with details of the computational domain and initial and boundary conditions. In Section 3 we present the hydrodynamics results and discuss the updated correlation between *Nu* vs *Ra* in the context of previous studies. Spatial distribution of the particle deposition and the average deposition rate on each thermally active wall for each particle size are also presented. Section 4 analyzes the comparison of the numerical predictions with experiments and boundary layer theory. Finally, in Section 5 we outline the conclusions and comment on future work.

2. Physical and mathematical model

Following the experimental set-up used by Thatcher et al. [27], the computational domain used here consists in a cubical cavity of side length $\widetilde{l} = 3.14$ m filled with air where two pairs of opposed walls are kept at constant but different temperatures. Note that dimensional quantities are denoted with a tilde. The turbulent flow is driven by holding the bottom (*floor*) and left vertical wall temperature constant at $\widetilde{T}_h$, i.e. $\widetilde{T}(\widetilde{x}, -\widetilde{l}/2, \widetilde{z}) = \widetilde{T}(-\widetilde{l}/2, \widetilde{y}, \widetilde{z}) = \widetilde{T}_h$ (in red in Fig. 1) and the top (*ceiling*) and right vertical walls at $\widetilde{T}_c = \widetilde{T}_h - 1.3$ K, i.e. $\widetilde{T}(\widetilde{x}, \widetilde{l}/2, \widetilde{z}) = T(\widetilde{l}/2, \widetilde{y}, \widetilde{z}) = \widetilde{T}_c$ (in blue in Fig. 1). The two remaining walls, normal to direction z, are assumed perfectly insulated, i.e.

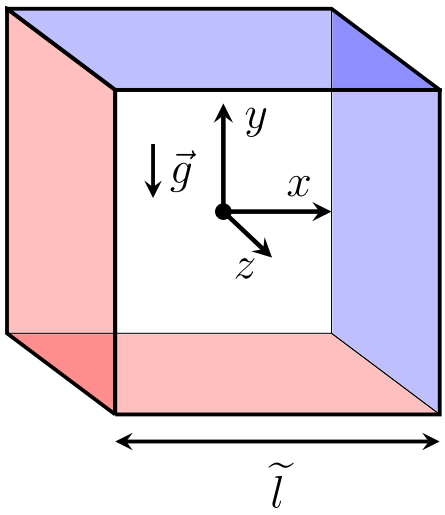

Fig. 1. Sketch of the computational domain.

$$\left.\frac{\partial \widetilde{T}}{\partial \widetilde{z}}\right|_{\widetilde{z}=\pm\widetilde{l}/2} = 0.$$

All physical properties of both the carrier (air) and dispersed phases are evaluated at the reference temperature $\widetilde{T}_0 = (\widetilde{T}_h + \widetilde{T}_c)/2 = 300$ K and gravity is aligned with the $-y$ direction.

To investigate the transport and deposition of suspended material on each surface, 55,000 particles of 0.1, 0.5, 0.7, 1.3 and 2.5 μm in diameter were randomly seeded within the domain once statistically steady conditions were reached. The total of 275,000 idealized (smooth and spherical) particles were allowed to circulate within the cavity over $\Delta\widetilde{t} = 1.4 \times 10^3$ s. Using identical flow computational set-up and mathematical models as in Fabregat et al. [18] (see this reference for details), here we use the Boussinesq approximation assuming incompressibility and neglecting radiation and viscous dissipation. Thus, the non-dimensional mass, momentum and heat conservation equations can be written as:

$$\frac{\partial u_i}{\partial x_i} = 0 \tag{1}$$

$$\frac{\partial u_i}{\partial t} + u_j\frac{\partial u_i}{\partial x_j} = -\frac{\partial p}{\partial x_i} + \frac{Pr}{\sqrt{Ra}}\frac{\partial^2 u_i}{\partial x_j \partial x_j} + PrT\delta_{i2} \tag{2}$$

$$\frac{\partial T}{\partial t} + u_j\frac{\partial T}{\partial x_j} = \frac{1}{\sqrt{Ra}}\frac{\partial^2 T}{\partial x_j \partial x_j} \tag{3}$$

where t is time, u_i is the velocity component in the direction x_i, p is pressure, T is temperature perturbation and *Ra* and *Pr* are the Rayleigh and Prandtl groups defined as:

$$Ra = \frac{g\beta T_s l_s^3}{\nu\alpha} = 3.6 \times 10^9 \tag{4}$$

$$Pr = \frac{\nu}{\alpha} = 0.7. \tag{5}$$

where ν is the kinematic viscosity, α is the thermal diffusivity, β is the thermal expansion coefficient and g is the gravitational acceleration. The length, velocity, time and temperature scales are $l_s = \widetilde{l} = 3.14$ m, $u_s = \alpha Ra^{1/2}/\widetilde{l} = 0.428$ m s^{-1}, $t_s = \widetilde{l}/u_s = 7.34$ s and $T_s = \Delta\widetilde{T} = 1.3$ K respectively.

Note that the equation of state that relates fluid density ρ_f and temperature deviation under the Boussinesq approximation can be written as:

$$\rho_f = \rho_0\left[1 - \beta\left(\widetilde{T} - \widetilde{T}_0\right)\right] \tag{6}$$

where ρ_0 is the reference density at $\widetilde{T}_0$. Eqs. (1)–(3) along with the initial and boundary conditions are solved using Nek5000 [30], an open source, high-order spectral element method (SEM) based solver for the incompressible Navier–Stokes equations. The basis functions in SEM are Nth-order tensor-product Lagrange polynomials on the Gauss–Lobatto–Legendre quadrature points inside each element that ensure fast evaluation and low storage cost operators [31]. Nek5000 uses a semi-implicit kth-order Backward Difference Formula (BDFk) and kth-order Extrapolation (EXTk) timestepping in which the time derivative is approximated by a BDFk while the nonlinear terms (and other forcings) are treated with a EXTk. The viscous and pressure terms are treated implicitly. This approach leads to a linear unsteady Stokes problem to be solved at each time step, which comprises a Helmholtz equation for each component of velocity (and temperature or scalars) and a Poisson equation for pressure [32]. Nek5000 has been extensively used to carry out both DNS and LES simulations in a wide variety of flow configurations and applications [33–35].

The mesh grid, with a total of approximately 300 million nodes,

ensures the explicit resolution of all spatial and temporal scales according to the resolution criteria proposed by Scheel et al. [36] for similar buoyancy driven flow configurations. The minimum and maximum grid grid spacings are $\Delta X_{min} = \Delta Y_{min} = \Delta Z_{min} = 3.3 \times 10^{-3}$ and $\Delta X_{max} = \Delta Y_{max} = \Delta Z_{max} = 1.4 \times 10^{-4}$ non-dimensional units, respectively. Further details on numerics and mesh generation can be found in Fabregat and Pallares [18].

Regarding the transport of the dispersed phase, the equation of motion of an idealized spherical and smooth particle can be derived from the force balance acting upon it (see Fabregat and Pallares [18] for details). Thus, the position of a given particle x_i^* can be written as:

$$\frac{dx_i^*}{dt} = u_i^* \tag{7}$$

where the particle velocity u_i^* can be determined as:

$$\frac{du_i^*}{dt} = \underbrace{\frac{u_i - u_i^*}{St_p}}_{\text{Drag}} + \underbrace{n_g \delta_{i2}}_{\text{Buoyancy}} + \underbrace{n_{th}\frac{\partial T}{\partial x_i}}_{\text{Thermophoresis}} + \underbrace{n_l \varepsilon_{ijk}\left[u_j^* - u_j\right]\omega_k}_{\text{Lift}} + \underbrace{n_i(t)}_{\text{Brownian}} \tag{8}$$

where St_p is particle the Stokes number, n_g is the magnitude of the buoyancy force experienced by a particle, δ_{ij} is the Kronecker delta, n_{th} is the pre-factor of the non-dimensional temperature gradient, n_l is the lift proportionality factor, ε is the Levi–Civita symbol, $\vec{\omega} = \vec{\nabla} \times \vec{u}$ is the flow vorticity and n_i is the Brownian force.

The particle transport model presented in Eqs. (7) and (8) assumes that there are five relevant forces acting on the particle, namely, hydrodynamic drag and lift, buoyancy, thermophoresis and Brownian. Under the one-way coupling approach, used in this work, the dispersed phase is assumed to have negligible contributions to the carrier phase momentum conservation. This assumption is valid for small enough particles and dilute systems.

2.1. Drag

Hydrodynamic drag accounts for the fluid resistance or friction a particle experiences as it moves with respect to the carrier phase. The hydrodynamic drag can be characterized by the particle Stokes number defined as the ratio of the particle and flow characteristic times. Small St_p are associated to particles that rapidly react to changes in accelerations in the underlying flow while large Stokes are found in inertia-dominated particles. The Stokes number for a particle of diameter $\widetilde{d}_p$ can be written as:

$$St_p = \frac{d_p^2}{18C_c}\frac{\rho_p}{\mu_f}u_s l_s \tag{9}$$

where ρ_p is the particle density, C_c is the Cunningham correction factor.

$$Kn = \frac{2\lambda}{\widetilde{d}_p} \tag{10}$$

$$C_c = 1 + Kn\left[1.205e^{-0.0026/Kn} + 0.425e^{-0.7400/Kn}\right] \tag{11}$$

where $d_p = \widetilde{d}_p/l_s$ is the non-dimensional particle diameter and $\lambda = 6.8 \times 10^{-8}$ m is the free mean path in air at $\widetilde{T}_0$ [37].

2.2. Buoyancy (weight)

The magnitude of the buoyancy force experienced by a particle within a fluid with different density under a gravitational field with acceleration magnitude $g = 9.81$ m s^{-2} can be written as:

$$n_g = -g\left(1 - \frac{\rho_f}{\rho_p}\right)\frac{l_s}{u_s^2}. \tag{12}$$

2.3. Thermophoresis

Thermophoresis is the force due to gradients in the temperature field across the particle characteristic length. The pre-factor of the non-dimensional temperature gradient, n_{th}, is defined as [38]:

$$n_{th} = -18\frac{K_{tp}}{d_p^2}\frac{\nu_f^2}{\widetilde{T}_0}\frac{\rho_f}{\rho_p}\frac{T_s}{l_s^2 u_s^2} \tag{13}$$

where the factor K_{tp}, defined as,

$$K_{tp} = \frac{2C_s\left(k_f + 2k_p Kn\right)\left[1 + 2Kn(1.2 + 0.41\exp(-0.44/Kn))\right]}{\left(1 + 6C_m Kn\right)\left(2k_f + k_p + 4k_p C_t Kn\right)}, \tag{14}$$

contains three constant set to $C_s = 1.17, C_m = 1.14$ and $C_t = 2.18$. Note that the negative sign in n_{th} indicates that the force points in the direction of maximal temperature decay.

2.4. Lift

The hydrodynamic force acts perpendicular to the flow direction and is proportional to the cross product of the velocity difference between the two phases and the local vorticity in the carrier phase. The proportionality factor has the form

$$n_l = C_L\frac{\rho_f}{\rho_p} \tag{15}$$

where the lift coefficient C_L is defined as [39]:

$$C_L = \left[5.816\sqrt{\frac{Sr_p}{2Re_p}} - 0.875\frac{Sr_p}{2}\right]\frac{3}{4Sr_p}\frac{J(\varepsilon)}{2.255} \tag{16}$$

where the particle Reynolds number is Re_p, particle Strouhal number is Sr_p, ε and J are determined using the relations:

$$Re_p = \left|u_i^* - u_i\right| d_p Re, \tag{17}$$

$$Sr_p = \frac{\left|\epsilon_{ijk}\left[u_j^* - u_j\right]\omega_k\right|}{\left|u_j^* - u_j\right|^2}d_p, \tag{18}$$

$$\varepsilon = \sqrt{\frac{Sr_p}{Re_p}}, \tag{19}$$

$$J(\varepsilon) = 0.6765\{1 + \tanh[2.5\log_{10}(\varepsilon + 0.191)]\}\{0.677 + \tanh[6(\varepsilon - 0.32)]\}. \tag{20}$$

2.5. Brownian

For small enough particles, the net force due to molecular vibrations may not be negligible and, therefore, contribute to the transport. This Browninan force takes the form [40]:

$$n_i\left(t\right) = Z_i\sqrt{\frac{2\pi}{\Delta t}216\frac{\rho_f}{\rho_p^2}\frac{k_B\widetilde{T}_0\nu_f}{d_p^5\pi^2 C_c}\frac{\widetilde{t}^3}{\widetilde{l}^7}} \tag{21}$$

where Z_i is independent zero-mean Gaussian random number, $k_B = 1.38064852 \times 10^{-23}$ J K^{-1} is the Boltzmann constant.

2.6. Settling velocity

To gain insight into the role played by the flow hydrodinamics on the wall deposition, the deposition rate is often compared with the settling velocity, v_s. This quantity is determined by assuming that the only forces acting on a particle suspended in a quiescent fluid are drag and buoy-

ancy. Simplifying Eq. (8), the expression for v_s yields

$$v_s = St_p n_g \delta_{i2}. \tag{22}$$

2.7. Exponential-Lagrangian Tracking Schemes

Eqs. (7) and (8) are temporally integrated using Exponential-Lagrangian Tracking Schemes (ELTS) [41]. ELTS are inherently stable and offer, at least, $\mathcal{O}(\Delta t^2)$ local truncation errors depending on the application. Details on the ELTS temporal discretization can be found in [18].

The Spectral Element Method (SEM) spatial discretization used in Nek5000 where the numerical approximation in each element can be expressed as a three-dimensional Legendre polynomial expansion of order N^3 is used to interpolate the particle velocity on the previous time step or in any other intermediate time in the predictor–corrector approach used in ELTS (see details in [18]).

3. Results

3.1. Flow hydrodynamics

To illustrate the hydrodynamic and thermal fields under statistically developed conditions, Fig. 2 shows three slices for an arbitrary flow snapshot at $t \approx 200$ as indicated in panel (a). The instantaneous non-dimensional temperature field (T) at $z = 0$ in panel (b) clearly shows the signature of the persistent large scale clockwise recirculation rising along the hot vertical wall and descending along the cold one. The distinct levels of turbulence intensities between the boundary layers along the solid surfaces and the mildly fluctuating central region clearly emerge in the temperature field characterized by the presence of turbulent intrusions in the vicinity of walls. To elucidate the rich flow structure within the boundary layers, panel (c) shows the horizontal velocity component u_x very close to the top cold wall ($y = 0.495$). The fine scale turbulence structure is characterized by the presence of streak-like patterns within the momentum boundary layer mostly aligned with the dominant current direction. When compared to panel (c), the vertical velocity component u_y near the vertical cold wall at $x = 0.495$ shown in panel (d) exhibits a distinct structure that reflects the difference between both walls orientation with respect to the gravitational action.

To illustrate the temporal evolution of the flow under statistically converged conditions Fig. 3 shows a sample of the time evolution of the volume-averaged (indicated with an overbar) kinetic energy k and its dissipation ε defined as:

$$\overline{k} = \frac{1}{2V}\int_V \left(u_i u_i\right) dV \tag{23}$$

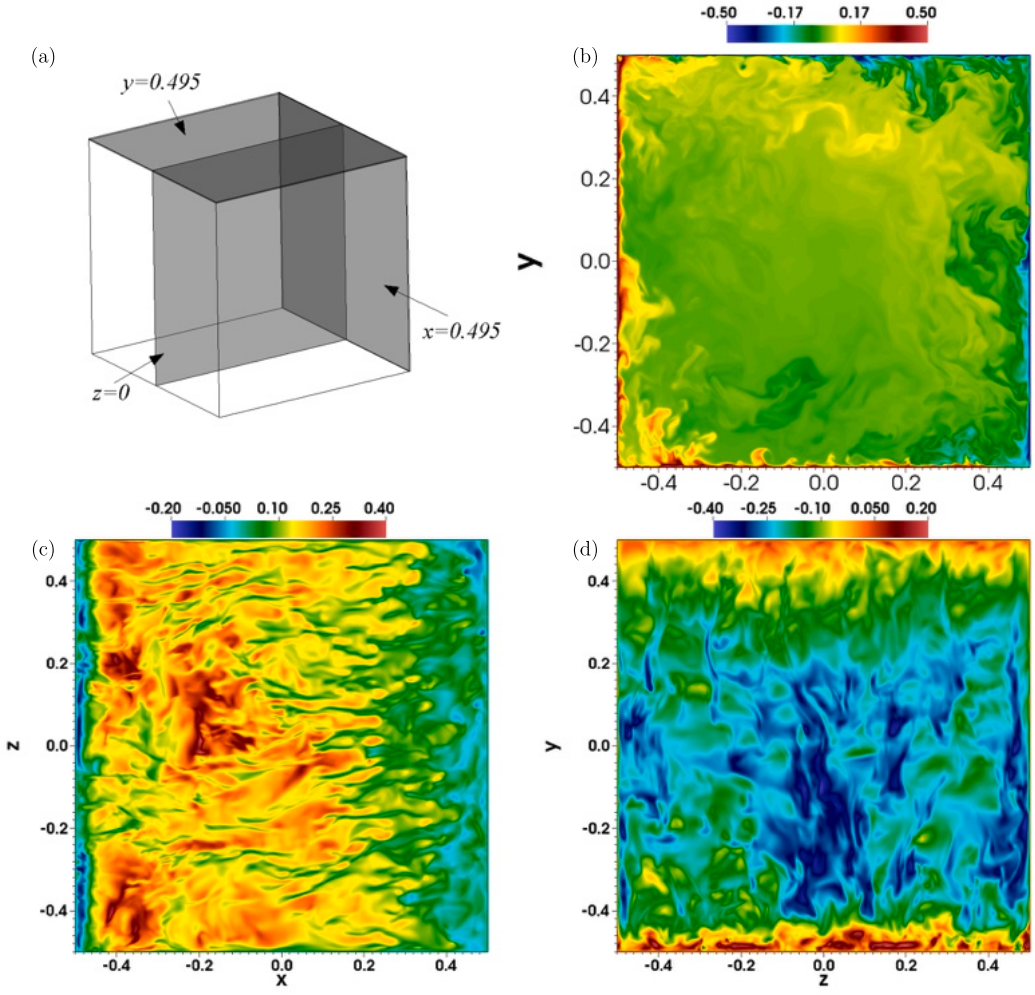

Fig. 2. (a) Three slices across the cavity domain: (b) instantaneous temperature field at $z = 0$, (c) horizontal velocity component at $y = 0.495$ and (d) vertical velocity component at $x = 0.495$.

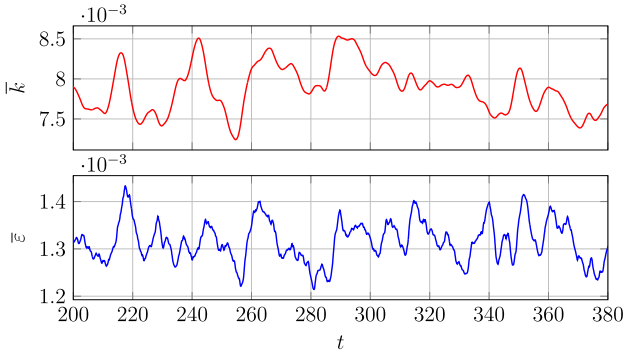

Fig. 3. History sample showing the temporal evolution of the volume-averaged turbulent kinetic energy $\overline{k}$ (top panel) and turbulent dissipation $\overline{\varepsilon}$ (bottom).

and

$$\overline{\varepsilon} = \frac{Pr}{\sqrt{Ra}V}\int_V \left(\frac{\partial u_i}{\partial x_i}\frac{\partial u_i}{\partial x_i}\right) dV \tag{24}$$

where V is cavity volume. The corresponding non-dimensional temporal scale is $\tau = \langle\overline{k}\rangle/\langle\overline{\varepsilon}\rangle \approx 6$ where angle brackets indicate temporally averaged quantities.

Fig. 4 shows the time-averaged non-dimensional horizontal (a) and vertical (b) velocity components (u_x, u_y) at $z = 0$. It can be seen that the contours are antisymmetrical with respect to the origin of the coordinate system located at the center of the cavity (see Fig. 1). The corresponding profiles of the non-dimensional time-averaged temperature and velocity components u and v along the vertical and horizontal cavity bisectors are shown in Fig. 5. Panel (a) shows the temperature results for the present $Ra = 3.6 \times 10^9$ in black. For comparison, the profiles at $Ra = 10^7$ (red), 10^8 (blue) and 5.4×10^8 (green) presented in Fabregat and Pallarès [18] are also included. Analogously, panel (b) shows the time-averaged profiles of u along the vertical cavity bisector and v along the horizontal one. These results show the progressive thinning of both the momentum and thermal boundary layers and the increase of wall heat transfer and wall shear stress as Rayleigh number increases. It can also be seen that vertical velocity near the hot and cold walls is slightly higher than the horizontal velocity near the hot floor and cold ceiling.

The temporal evolution of $\widehat{Nu}$ is shown in Fig. 6 over the same temporal sample used in Fig. 3. Hot and cold vertical walls results are shown in orange and teal, respectively, while red and blue are used for the hot and cold horizontal walls. Temporal averages of wall-averaged Nusselt number for the horizontal and vertical walls are

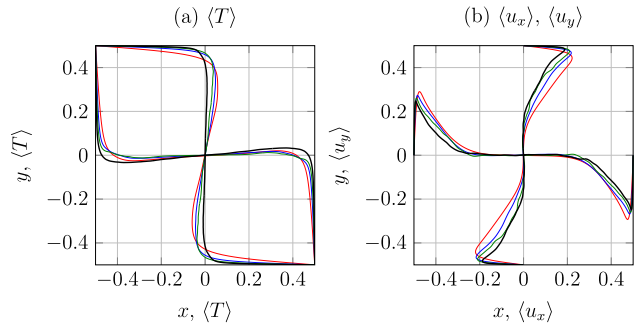

Fig. 5. Time-averaged non-dimensional temperature (a) and velocity (b) profiles along the horizontal and vertical bisectors of the symmetry plane of the cavity z $= 0$. Red, blue, green and black represents $Ra = 1.0 \times 10^7, Ra = 1.0 \times 10^8, Ra = 5.4 \times 10^8$ and $Ra = 3.6 \times 10^9$ respectively.

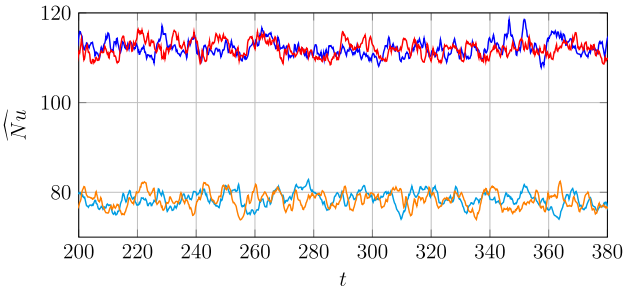

Fig. 6. Temporal evolution of the (absolute) wall-averaged Nusselt number on each wall. Red and blue correspond to the horizontal hot and cold walls respectively while orange and teal correspond to the vertical hot and cold walls.

approximately $\langle\widehat{Nu}_b\rangle = \langle\widehat{Nu}_t\rangle = 112$ and $\langle\widehat{Nu}_l\rangle = \langle\widehat{Nu}_r\rangle = 78$, respectively. Where average heat flux across a given wall is defined as $\widehat{Nu}_m$:

$$\widehat{Nu}_m = -\int_{\Omega_m} \frac{\partial T_m}{\partial n_m}\, d\Omega_m \tag{25}$$

where $m = \{b, t, l, r, f, q\}$ represent each face of the cubical domain and n_m represent the corresponding face-normal direction. By definition, $\widehat{Nu}_f = \widehat{Nu}_q = 0$ on the adiabatic walls.

Fig. 7 shows the dependence of the temporal and wall-averaged Nusselt number on the Rayleigh number over the range between 10^3

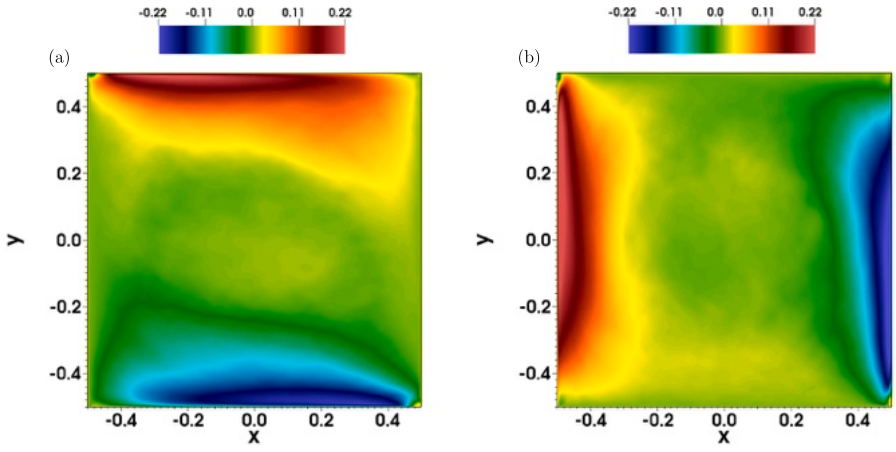

Fig. 4. Time-averaged non dimensional horizontal velocity (a) and vertical velocity (b) components at $z = 0$.

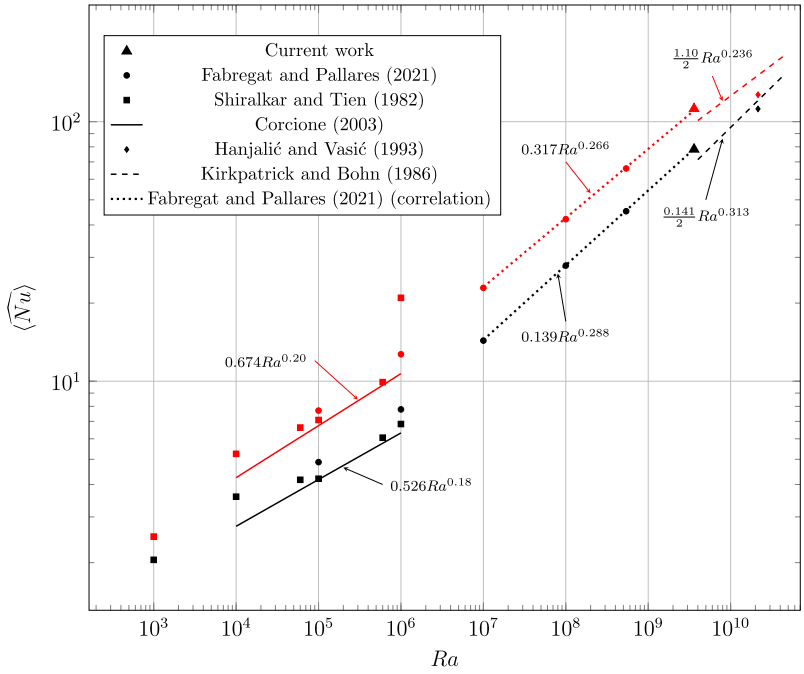

Fig. 7. Dependence of the vertical (black) and horizontal (red) time and wall-averaged Nusselt number on the Rayleigh number. Corcione [14] and Kirkpatrick & Bohn [17] correlations are show as solid and dashed lines respectively. Dotted line indicates the correlation for the current results over the entire Rayleigh number range.

and 10^{11} using black and red for the vertical and horizontal wall respectively. Results include 2D numerical simulations [12,14], 3D Reynolds-Averaged Navier–Stokes (RANS) solutions [16] and experiments [17]. The present DNS results at $Ra = 3.6 \times 10^9$, shown using triangles, suggest that the correlation derived for $10^7 \leqslant Ra \leqslant 5.4 \times 10^8$ by Fabregat and Pallarès [18] can be extended up to $Ra = 3.6 \times 10^9$. Specifically, these correlations for both the horizontal and vertical wall-averaged Nusselt number over the $10^7 \leqslant Ra \leqslant 3.6 \times 10^9$ are:

$$\langle \widehat{Nu} \rangle_{vert} = 0.139 Ra^{0.288}, \tag{26}$$

$$\langle \widehat{Nu} \rangle_{hor} = 0.317 Ra^{0.266} \tag{27}$$

In comparison to the correlations in [17] estimated from experimental data, the present correlations in Eqs. (26) and (27) predict slightly higher wall-averaged Nusselt number on both wall orientations. The extrapolation of the present correlations and those reported in [17] up to $Ra = 3.6 \times 10^9$ predicts larger values of wall-averaged Nusselt number in comparison to those reported by Hanjalić and Vasić [16].

3.2. Particle dynamics and deposition

To investigate the particle deposition on thermally active walls, a total of 275,000 ideal solid spherical particles of 0.1, 0.5, 0.7, 1.3 and 2.5 μm in diameter were randomly seeded and advected according to the model in Eqs. (7) and (8). Following the same approach used in Fabregat and Pallares [29], once the flow reached statistically steady conditions, the particle trajectory and deposition locations on each wall over the next $\Delta t = 180$ time units were recorded. The particle was assumed to deposit on the corresponding wall when the distance between the center of a particle and a wall was equal or less than its radius. No rebound and resuspension have been considered. Deposited particles are randomly reseeded within the cavity domain to ensure a constant number of suspended particles across the entire simulation. The Stokes number of the smallest and the biggest particles are $St_p = 8.4 \times 10^{-9}$ and $St_p = 3.3 \times 10^{-5}$ respectively. The ability of the model in Eqs. (7) and (8) to predict the rate at which particles deposit on each surface of the cavity at $Ra = 3.6 \times 10^9$ is assessed by comparing the numerical results with the experiments of Thatcher et al. [27] and also with the predictions from the Boundary Layer (BL) model derived by Pallares and Fabregat [28].

Figs. 8–12 show the landing positions on each wall for each particle size using red, blue and black markers to distinguish between hot, cold and adiabatic walls respectively. Arrows are used to indicate the large scale flow direction.

The absence of deposition for particles of 0.1 and 0.5 μm in diameter suggests that thermophoresis force prevents the smallest particles from landing on the hot walls.

While landing positions across the vertical cold wall are approximately homogeneous, the horizontal wall exhibits larger impact density near the region where the ascending fluid along the vertical hot wall impinges on the ceiling. This can be explained by the intensified favourable temperature gradient in the vicinity of this corner where a hot vertical wall meets a cold horizontal one. On the adiabatic walls, where no thermal forcing hinders or favors particle transport by means of thermophoresis, only a few particle depositions were recorded.

For larger particles of 0.7 μm, results in Fig. 10 suggest that deposition on the ceiling are restricted to the region where the (negative) vertical gradient of temperature exceeds the gravitational force with most of landings occurring within $-1/2 < x < -1/3$. Similar magnitudes between these two opposing terms explain also the few depositions recorded on the hot horizontal wall. Again, the absence of thermal and gravitational components along the z-axis results in a few landings on the adiabatic walls.

As shown in Figs. 11 and 12, as particle size increases, the contribution of gravity to particle transport relative to thermophoresis increases. Thus, while deposition rate increases at the hot floor surface, it decays at the cold ceiling. Despite this, the intensified thermal gradient near the bottom right corner where descending cold fluid impinges on the hot floor leads to decreased floor deposition rate for particles of 1.3 μm in the vicinity of this location. This inhomogeneity vanishes in the case of the largest particles as shown in Fig. 12. Note that Fig. 11 has one deposited particle on the cold ceiling and this particle is not taken into

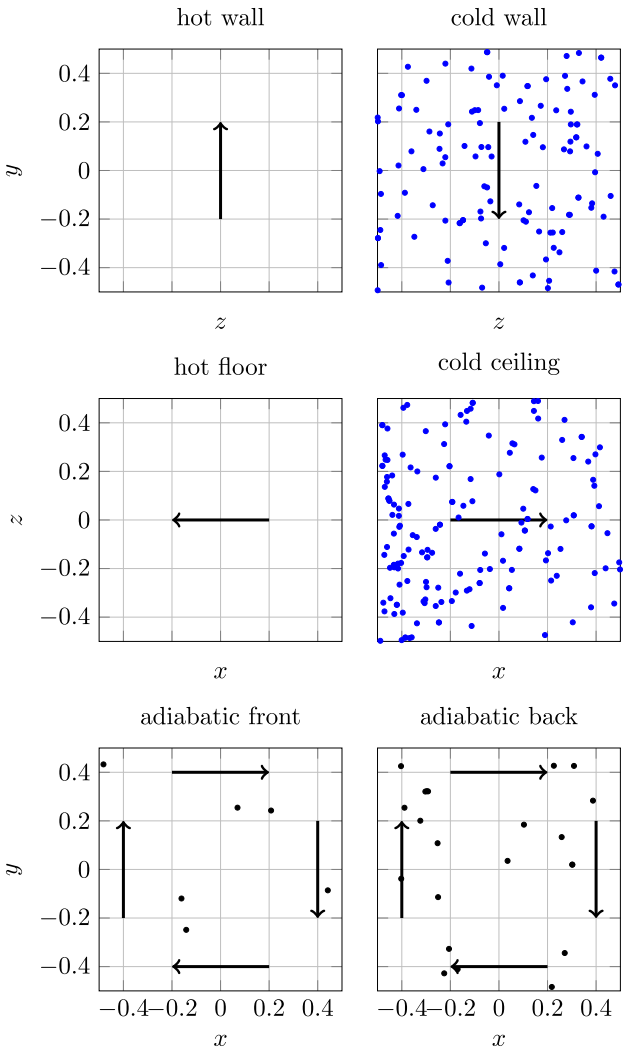

Fig. 8. Landing positions on the walls of particles with $\widetilde{d}_p = 0.1$ μm. The direction of the large scale circulation close to the wall is indicated with an arrow.

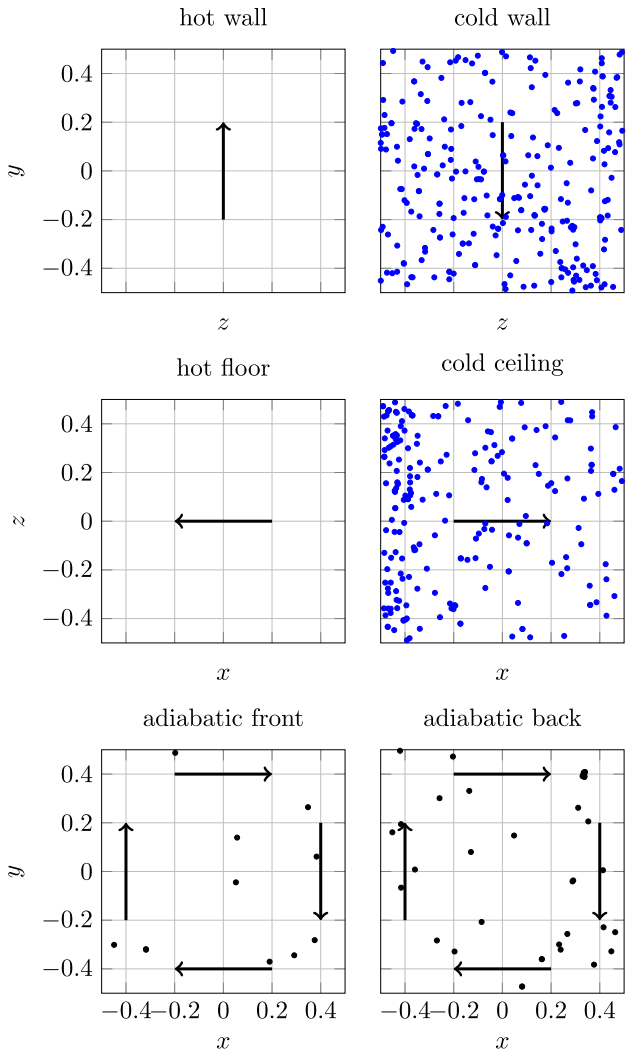

Fig. 9. Landing positions on the walls of particles with $\widetilde{d}_p = 0.5$ μm. The direction of the large scale circulation close to the wall is indicated with an arrow.

account when calculating the deposition velocity.

The results for particles with diameters of 1.3 and 2.5 μm suggest that although thermophoresis forces are no longer able to establish a net transport of particles towards the ceiling, they remain significant in the horizontal direction as evidenced by the deposition solely on the cold vertical wall. Deposition on thermally inactive walls are found to be mostly independent of the particle size over the considered diameter range.

The wall-averaged deposition velocity is defined as:

$$\widehat{v}_d = \frac{\widetilde{M}_s}{\Delta\widetilde{t}_d \left\langle C \right\rangle \widetilde{A}_d} = \frac{N_d}{N} \frac{\widetilde{l}}{\Delta\widetilde{t}_d} \tag{28}$$

where N is the total number of particles, N_d is the number of deposited particles over the time span $\Delta\widetilde{t}_d$ and area $\widetilde{A}_d = \widetilde{l}^2$, $\widetilde{M}_s = \rho_p \widetilde{A}_d \widetilde{V}_p$ is the total deposited mass of the particles, $\widetilde{V}_p = (\pi/6)\widetilde{d}_p^3$ is the particle volume and $\langle C \rangle = \rho_p N \widetilde{V}_p / \widetilde{l}^3$ is the bulk concentration of suspended particles which is kept constant in the simulations. Fig. 13 shows the dimensional deposition velocity along the perimeter of the vertical symmetry plane of the cavity. The present DNS wall-averaged deposition velocity for each particle size and thermally active wall are shown in Fig. 13 as horizontal dark blue lines. Using empty and filled black markers for the two different reported experiments at $Ra = 3.6 \times 10^9$, the same figure also shows the experimental results by Thatcher et al. [27] along with the experimental detection limit depicted using a red dashed line. BL model predictions of wall-averaged deposition velocity from Pallares and Fabregat [28] are shown in magenta color. Green dashed line shows settling velocity defined in Eq. (22). For completeness, we also included using teal lines the results by Kim et al. [24], who numerically simulated a DHC with one pair of vertical thermally active walls using LES at $Ra = 10^9$ to determine the deposition rate of 0.7, 1.3 and 2.5 μm particles on the thermally active vertical walls and 0.7 μm particles on the adiabatic floor.

DNS and BL model predictions of the deposition rate on both cold walls for the smallest particles of 0.1 and 0.5 μm are in a good agreement. When compared to experiments of Thatcher et al. [27], both DNS and BL model underpredict the rate of deposition of 0.1 μm particles on both cold walls while slightly overpredicted values are found for 0.5 μm particles. For these two particle sizes, DNS predicts no deposition on the hot walls while BL model are found to predict relatively small rates in quite good agreement with the experimental results. In the case of particles with diameter 0.1 μm, experimental results are in between the

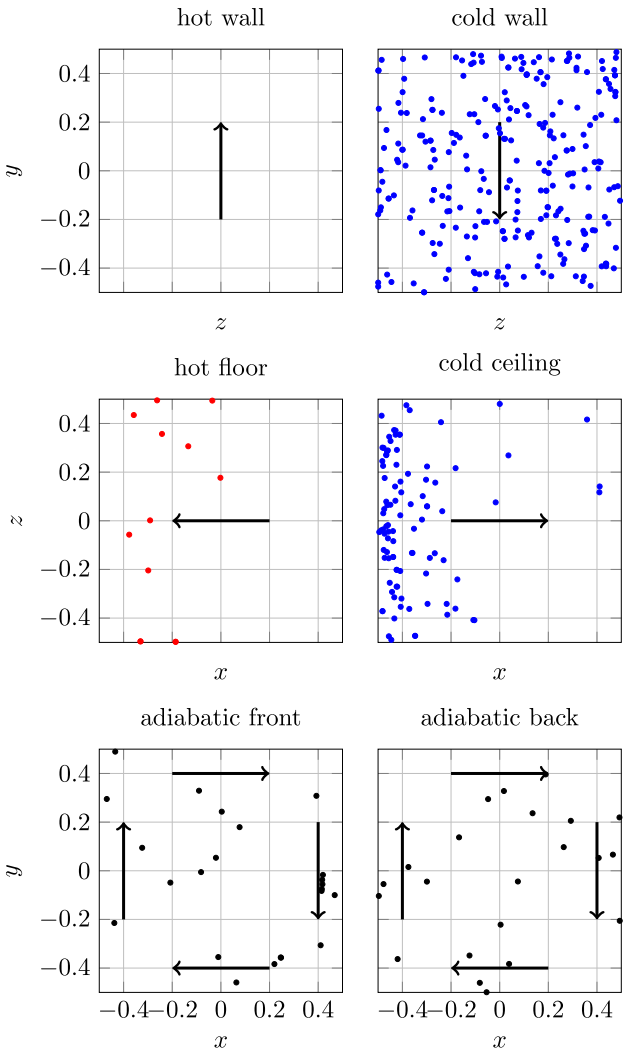

Fig. 10. Landing positions on the walls of particles with $\widetilde{d}_p = 0.7\,\mu m$. The direction of the large scale circulation close to the wall is indicated with an arrow.

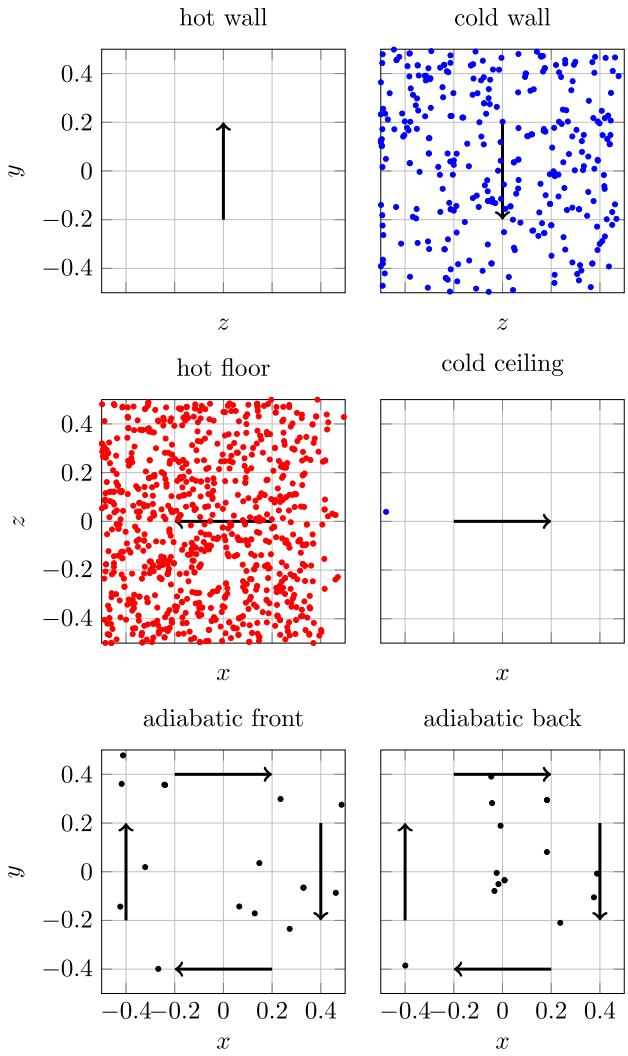

Fig. 11. Landing positions on the walls of particles with $\widetilde{d}_p = 1.3\,\mu m$. The direction of the large scale circulation close to the wall is indicated with an arrow.

BL model prediction and the settling velocity. Experimental values for particles of 0.5 μm are notably smaller that those obtained by the BL model which are in very good agreement with the settling velocity. BL model also predict a very small deposition rate on the vertical wall for 0.1 μm but no deposition for 0.5 μm particles. Experimental data on this vertical surface is below (0.1 μm) or very close (0.5 μm) to the detection limit.

For particles of 0.7 μm, experimental deposition rates on the hot floor are bounded between the BL and the numerical predictions. Although neither BL nor DNS predict any deposition on the vertical hot wall, measurements of Thatcher et al. [27] did record some particle deposition, albeit, very close to the detection level. Although exhibiting a fair amount of data dispersion, experimental deposition rate on the cold ceiling is in good agreement with DNS results (BL model predict no deposition). The significant value of deposition rate on this surface suggests that the vertical thermophoretic force is capable of balancing the gravitational force along the vertical direction. All three predictions, DNS, BL model and experiments exhibit very good agreement on the cold vertical wall.

Current DNS, BL model and experimental results are in very good agreement for the largest particles of 1.3 and 2.5 μm in diameter. Both the numerical simulations and the BL solutions predict particles exclusively depositing on the floor and on the right cold wall with no impacts on the left warm wall and cold ceiling. In contrast, experimental results reported a few depositions on these two surfaces although data is notably dispersed and near the detection limit. Despite differences in the flow configuration, the values of deposition velocity reported by Kim et al. [24] for $Ra = 10^9$ are quite similar.

4. Discussion

There exists a discrepancy between the DNS deposition rate predictions and the values obtained with the BL model and the experimental measurements for the particles between 0.1 and 0.7 μm. Specifically, while DNS predicted no deposition for the 0.1 and 0.5 μm particles on the hot floor, BL models results were in agreement to the experiments which reported non-negligible deposition rates above the detection level (see Fig. 13). Similarly, DNS for the 0.7 μm particles under-predicted the experimental observations on the same surface. These differences might be explained, first, by the construction of the BL solutions. In the derivation of the particle deposition rate (see [28]), the dispersed phase velocity was decomposed into two components, one

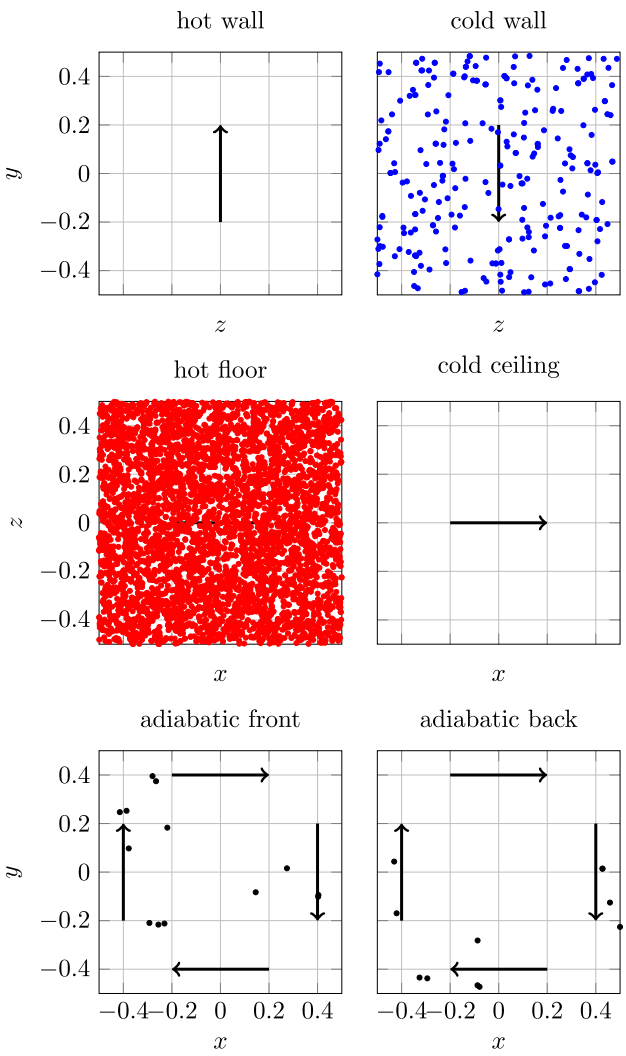

Fig. 12. Landing positions on the walls of particles with $\widetilde{d}_p = 2.5$ µm. The direction of the large scale circulation close to the wall is indicated with an arrow.

accounting for gravitational settling velocity and the other accounting for the rest of the transport contributions, namely, hydrodynamic drag, thermophoresis and Brownian forces. By doing so, the form of the force balance without the gravitational contribution could be integrated and then corrected to account for this initially neglected term. As shown in Pallares and Fabregat [28], these approaches are capable of accurately predicting both DNS and experiments for both 0.1 and 0.5 µm in a $Ra = 5.4 \times 10^8$ cavity. However, when the magnitude of the thermophoresis effect is comparable or larger than gravity (this is when particles are small and Ra is high), these models tend to over-predict the deposition on horizontal walls as a result of the correction to take into account the gravity force. Thereby, under conditions dominated by thermophoresis, BL model tend to predict deposition velocities close to the settling velocity (See Fig. 13 for particles of 0.1, 0.5 and 0.7 µm). To illustrate the relative importance of the gravitational and thermophoresis forces, Table 1 shows the non-dimensional values of the buoyancy (n_g) and the surface averaged thermophoresis terms ($n_{th}\frac{dT}{dy}$) on the horizontal walls for each particle size. For comparison, the surface horizontal thermophoresis term ($n_{th}\frac{dT}{dx}$) on the thermally active vertical walls has also been included. All in all, in the absence of gravitational effects, the BL models predictions on vertical walls are in good agreement with DNS and experimental results (See Fig. 13).

Notably, Thatcher et al. [27] mention that their experimental results do not agree with the theoretical predictions of Nazaroff and Cass [42] for some particle sizes. This observation could suggest that the balance between thermophoresis and gravitational effects may not be properly accounted for in this model. In addition, the experimental non-negligible deposition rate reported by Thatcher et al. [27] might be explained by enhanced gravitational effects associated to particle agglomeration. In this regard, Kim et al. [24] used experiments to investigate particle removal rates in a DHC of side length 0.7 m with two opposite vertical walls held at different temperatures and the rest adiabatic. The transport of monodisperse particles with aerodynamically equivalent diameters of 0.7, 1.4, and 3.5 µm, which corresponds to 0.5, 1.0 and 2.5 µm physical diameter, at $Ra = 10^9$ was estimated by sampling particle concentration every 10 to 30 min for 1.0 and 2.5 µm and 1 h for 0.5 µm particles. Using microscopic imaging, these authors reported the existence of duplets, triplets and even quadruplets produced by particle adhesion phenomenon. Table 2 shows the Kim et al. [24] average and standard deviation results for single and agglomerate fractions from the particle size also considered in the present work. Using the same experimental setup and similar flow conditions, Kalilainen et al. [22] reported single particle fractions of between 69% and 74% and between 89% and 95% for 1.0 and 2.5 µm respectively with agglomerates of up to seven particles.

The works of Kim et al. [24] and Kalilainen et al. [22] suggested that adhesion effects under similar conditions as those used by Thatcher et al. [27] is plausible, although, no reported analysis on agglomerates was reported. In addition, particle seeding method used by Kim et al. [24] and Kalilainen et al. [22] who used the same DHC experimental setup differs from Thatcher et al. [27].

5. Conclusion

Using a one-way coupling between the carrier and the disperse phase, turbulent convective flow in a cubical cavity with two pairs of opposed thermally active walls at $Ra = 3.6 \times 10^9$ and suspended particle transport and deposition have been numerically investigated using DNS.

Temporal averages of the hydrodynamic field allowed to expand the correlations between the Rayleigh number and the wall-averaged Nusselt number derived by Fabregat and Pallares [18] up to 3.6×10^9 and to compare the present results with those available in the literature for a relatively wide range of Rayleigh numbers. Particle deposition rate on each cavity wall are reported and compared to the BL model and experimental results. The use of a disperse phase transport model accounting for hydrodynamic drag, buoyancy, lift, thermophoresis and Brownian effects is shown to accurately predict the wall deposition velocity for a relatively wide range of particle sizes ranging between thermophoresis and buoyancy dominated regimes at a relatively high Rayleigh number.

Results show that BL model is able to accurately predict deposition velocity of supermicron particles at $Ra = 3.6 \times 10^9$. For submicron particles there are differences compared with the DNS. This could be explained by the assumptions made in the derivation of the BL solutions. As a result, when the magnitude of the thermophoresis effect is similar to or larger than gravitational force, these models tend to over-predict the deposition on horizontal walls. DNS predictions of deposition velocity for supermicron particles are in excellent agreement with the experiment and BL model. Discrepancy appears when particles are less than one micron and thermophoresis is the dominating force. As suggested in the literature, this non-negligible difference with experiments for submicron particles could be explained considering the phenomenon of particle agglomeration (see Section 4).

Considering everything, our results suggest that the deposition of submicron particles is heavily influenced by thermophoretic forces. On the other hand, thermophoresis has negligible influence on deposition

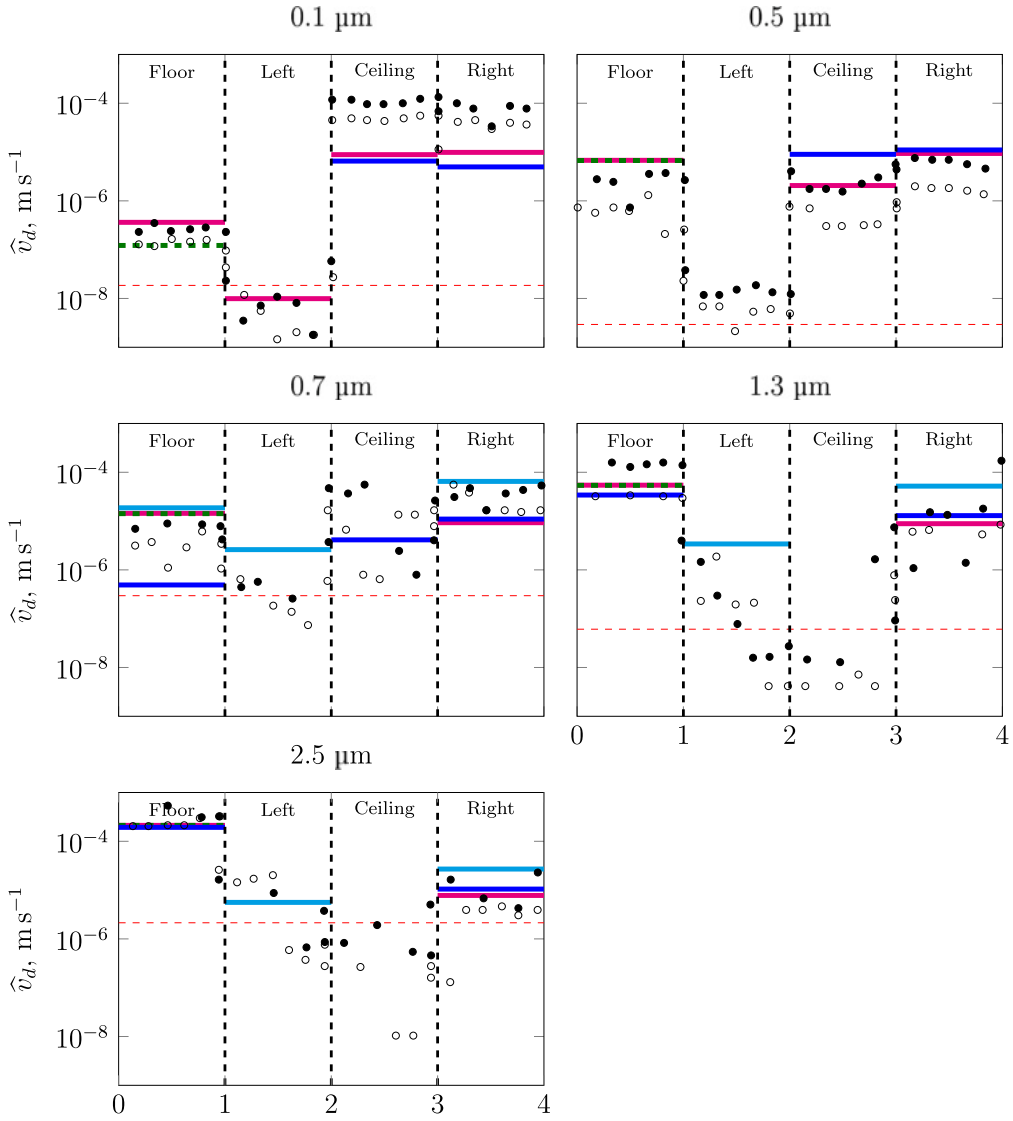

Fig. 13. Particle wall-average deposition velocity for all five diameters and four thermally active walls. Magenta and blue color represent BL model and DNS results, respectively. Dashed green line is the settling velocity. Red dashed line indicates the experimental detection level. Empty and filled round markers represent two different realisations of the experiment reported by Thatcher et al. [27]. Kim et al. [24] LES results are shown with teal lines.

Table 1

Buoyancy (n_g), horizontal ($n_{th}\frac{dT}{dx}$) and vertical ($n_{th}\frac{dT}{dy}$) thermophoresis terms for considered particle sizes.

$\widetilde{d}_p$, μm	n_g	$n_{th}\frac{dT}{dy}$	$n_{th}\frac{dT}{dx}$
0.1	−65.64	2165.03	1507.79
0.5	−65.64	84.41	58.79
0.7	−65.64	42.74	29.76
1.3	−65.64	11.97	8.34
2.5	−65.64	2.97	2.07

Table 2
Prescribed sizes vs. averaged particle fractions.

$\widetilde{d}_p$, μm	single fraction (%)	double fraction (%)	triple fraction (%)
0.5	72 ± 3	20 ± 2	8 ± 3
1.0	85 ± 3	13 ± 2	2 ± 1
2.5	90 ± 2	9 ± 3	1 ± 1

rate of particles larger than one micrometer for which buoyancy forces dominate the transport (see Table 2). A similar conclusion can be found in Dehbi et al. [23], Kim et al. [24] and Thatcher et al. [27].

Future efforts would be directed to use the present results to investigate the relative dispersion of particle pairs initialized within spheres approximately representing the aerosol cloud generated by a human exhalation. The goal is to obtain accurate estimates of the time required by such cloud to homogeneously disperse in a human-scale room. These results would be of help to characterize the infection risk from airborne contagious diseases including COVID-19 in closed room taking into account natural convection.

CRediT authorship contribution statement

Akim Lavrinenko: Conceptualization, Software, Validation, Investigation, Data-curation, Writing-original-draft, Writing-review-editing, Visualization. **Ferran Gisbert:** Software, Data-curation. **Jordi Pallares:** Conceptualization, Methodology, Software, Validation, Investigation, Resources, Writing-review-editing, Supervision, Project-

administration, Funding-acquisition. **Alexandre Fabregat:** Conceptualization, Methodology, Software, Investigation, Validation, Resources, Writing-review-editing, Supervision, Project-administration, Funding-acquisition.

Declaration of Competing Interest

The authors declare the following financial interests/personal relationships which may be considered as potential competing interests: Akim Lavrinenko reports financial support was provided by Spanish Ministerio de Ciencia.

Data availability

Data will be made available on request.

Acknowledgements

This work has been funded by Spanish Ministerio de Ciencia, Innovación y Universidades through the grants RTI2018-100907-A-I00 and PID2020-113303 GB-C21 and by the Generalitat de Catalunya through the grant 2017-SGR-1234.

References

[1] Cdc public health science agenda for covid-19. URL:https://www.cdc.gov/coronavirus/2019-ncov/science/science-agenda-covid19.html.
[2] Global research on coronavirus disease (covid-19). URL:https://www.who.int/emergencies/diseases/novel-coronavirus-2019/global-research-on-novel-coronavirus-2019-ncov.
[3] D.L. Liu, Particle deposition onto enclosure surfaces, Aerospace Report No TR-2009 (8550-2) (2009). URL:https://apps.dtic.mil/sti/pdfs/ADA505166.pdf.
[4] S. Muraoka, R. Takagi, Y. Araki, K. Uda, M. Sumitomo, S. Okamoto, M. Nishihori, T. Izumi, M. Nakamura, R. Saito, Blood flow stagnation after treatment of a giant internal carotid artery aneurysm: a computed fluid dynamics analysis, Sci. Rep. 12 (2022).
[5] J. Meyerjürgens, M. Ricker, V. Schakau, T.H. Badewien, E.V. Stanev, Relative dispersion of surface drifters in the north sea: the effect of tides on mesoscale diffusivity, J. Geophys. Res.: Oceans 125 (2020), https://doi.org/10.1029/2019JC015925.
[6] R. Puragliesi, A. Dehbi, E. Leriche, A. Soldati, M. Deville, DNS of buoyancy-driven flows and Lagrangian particle tracking in a square cavity at high Rayleigh numbers, Int. J. Heat Fluid Flow 32 (5) (2011) 915–931, https://doi.org/10.1016/j.ijheatfluidflow.2011.06.007. URL:https://www.sciencedirect.com/science/article/pii/S0142727X11000956.
[7] P.M. Doran, Chapter 9 - Heat Transfer, in: P.M. Doran (Ed.), Bioprocess Engineering Principles, (Second Edition), second edition Edition,, Academic Press, London, 2013, pp. 333–377, https://doi.org/10.1016/B978-0-12-220851-5.00009-5.
[8] A. Vasiliev, A. Sukhanovsky, P. Frick, A. Budnikov, V. Fomichev, M. Bolshukhin, R. Romanov, High rayleigh number convection in a cubic cell with adiabatic sidewalls, Int. J. Heat Mass Transf. 102 (2016) 201–212, https://doi.org/10.1016/j.ijheatmasstransfer.2016.06.015.
[9] I. Miroshnichenko, M. Sheremet, Turbulent natural convection heat transfer in rectangular enclosures using experimental and numerical approaches: A review, Renew. Sustain. Energy Rev. 82 (2018) 40–59, https://doi.org/10.1016/j.rser.2017.09.005. URL:https://www.sciencedirect.com/science/article/pii/S1364032117312595.
[10] S. Pandey, Y. Park, M. Ha, An exhaustive review of studies on natural convection in enclosures with and without internal bodies of various shapes, Int. J. Heat Mass Transf. 138 (2019) 762–795, https://doi.org/10.1016/j.ijheatmasstransfer.2019.04.097.
[11] A. Ammar, m.A. Isam, m.S. Nejla, An exhaustive review on natural convection within complex enclosures: Influence of various parameters, Chin. J. Phys. 74 (2021) 365–388, https://doi.org/10.1016/j.cjph.2021.10.012. URL:https://www.sciencedirect.com/science/article/pii/S0577907321002574.
[12] G.S. Shiralkar, C.L. Tien, A numerical study of the effect of a vertical temperature difference imposed on a horizontal enclosure, Numer. Heat Transf. 5 (2) (1982) 185–197, https://doi.org/10.1080/10407788208913442, arXiv.
[13] S. Ostrach, C. Raghavan, Effect of stabilizing thermal gradients on natural convection in rectangular enclosures, J. Heat Transfer 101 (2) (1979) 238–243, https://doi.org/10.1115/1.3450953, arXiv:https://asmedigitalcollection.asme.org/heattransfer/article-pdf/101/2/238/5744423/238_1.pdf.
[14] M. Corcione, Effects of the thermal boundary conditions at the sidewalls upon natural convection in rectangular enclosures heated from below and cooled from above, Int. J. Therm. Sci. 42 (2) (2003) 199–208, https://doi.org/10.1016/S1290-0729(02)00019-4. URL:https://www.sciencedirect.com/science/article/pii/S1290072902000194.
[15] M.E. Danis, M. Orhan, A. Ecder, Isph modelling of transient natural convection, Int. J. Comput. Fluid Dyn. 27 (1) (2013) 15–31, https://doi.org/10.1080/10618562.2012.753146, arXiv.
[16] K. Hanjalic, S. Vasić, Computation of turbulent natural convection in rectangular enclosures with an algebraic flux model, Int. J. Heat Mass Transf. 36 (1993) 3603–3624.
[17] A. Kirkpatrick, M. Bohn, An experimental investigation of mixed cavity natural convection in the high Rayleigh number regime, Int. J. Heat Mass Transf. 29 (1986) 369–382.
[18] A. Fabregat, J. Pallarès, Heat transfer and boundary layer analyses of laminar and turbulent natural convection in a cubical cavity with differently heated opposed walls, Int. J. Heat Mass Transf. 151 (2020), 119409, https://doi.org/10.1016/j.ijheatmasstransfer.2020.119409. URL:https://www.sciencedirect.com/science/article/pii/S001793101935731X.
[19] European Enviroment Agency, 3.3 dispersion of hazardous substances. URL:https://www.eea.europa.eu/publications/92-9157-202-0/page303.html.
[20] S. Ogbonnaya, O. Ajayi, Fouling phenomenon and its effect on heat exchanger: a review, Front. Heat Mass Transf. 9 (2017), https://doi.org/10.5098/hmt.9.31.
[21] Coronavirus disease (covid-19): How is it transmitted? URL:https://www.who.int/news-room/questions-and-answers/item/coronavirus-disease-covid-19-how-is-it-transmitted.
[22] J. Kalilainen, P. Rantanen, T. Lind, A. Auvinen, A. Dehbi, Experimental investigation of a turbulent particle-laden flow inside a cubical differentially heated cavity, J. Aerosol Sci. 100 (C) (2016) 73–87, https://doi.org/10.1016/j.jaerosci.2016.06.001.
[23] A. Dehbi, J. Kalilainen, T. Lind, A. Auvinen, A large eddy simulation of turbulent particle-laden flow inside a cubical differentially heated cavity, J. Aerosol Sci. 103 (2016), https://doi.org/10.1016/j.jaerosci.2016.10.003.
[24] H. Kim, A. Dehbi, J. Kalilainen, Measurements and LES computations of a turbulent particle-laden flow inside a cubical differentially heated cavity, Atmos. Environ. 186 (2018) 216–228, https://doi.org/10.1016/j.atmosenv.2018.05.037. URL:https://www.sciencedirect.com/science/article/pii/S1352231018303418.
[25] Alvin C.K. Lai, Miriam A. Byrne, Antony J.H. Goddard, Experimental studies of the effect of rough surfaces and air speed on aerosol deposition in a test chamber, Aerosol Sci. Technol. 36 (10) (2002) 973–982, https://doi.org/10.1080/02786820290092249, arXiv.
[26] X. Zhong, S.C. Fu, K.C. Chan, C.Y. Chao, Experimental study of particle deposition on patterned microstructured surfaces in a chamber environment, J. Aerosol Sci. 157 (2021), 105802, https://doi.org/10.1016/j.jaerosci.2021.105802. URL:https://www.sciencedirect.com/science/article/pii/S0021850221005346.
[27] T.L. Thatcher, W.A. Fairchild, W.W. Nazaroff, Particle deposition from natural convection enclosure flow onto smooth surfaces, Aerosol Sci. Technol. 25 (4) (1996) 359–374, https://doi.org/10.1080/02786829608965402.
[28] J. Pallares, A. Fabregat, Prediction of particle deposition on the walls of a cubical cavity with differentially heated opposed walls using heat and mass transfer laminar mixed convection boundary layer models, Int. J. Heat Mass Transf. 165 (2021), 120691, https://doi.org/10.1016/j.ijheatmasstransfer.2020.120691. URL:https://www.sciencedirect.com/science/article/pii/S0017931020336279.
[29] A. Fabregat, J. Pallarès, Transport and wall surface deposition of airborne particles in enclosed, buoyancy-driven turbulent flows using fully-resolved numerical simulations, Int. Commun. Heat Mass Transfer 134 (2022), 106048, https://doi.org/10.1016/j.icheatmasstransfer.2022.106048. URL:https://www.sciencedirect.com/science/article/pii/S0735193322001701.
[30] P.F. Fischer, J.W. Lottes, S.G. Kerkemeier, Nek5000. URL:http://nek5000.mcs.anl.gov.
[31] M.O. Deville, P.F. Fischer, E.H. Mund, D.K. Gartling, High-Order Methods for Incompressible Fluid Flow, Appl. Mech. Rev. 56 (3) (2003), https://doi.org/10.1115/1.1566402. B43–B43. arXiv:https://asmedigitalcollection.asme.org/appliedmechanicsreviews/article-pdf/56/3/B43/5439822/b34_1.pdf.
[32] K. Mittal, S. Dutta, P. Fischer, Multirate timestepping for the incompressible navier-stokes equations in overlapping grids, J. Comput. Phys. 437 (2021), 110335, https://doi.org/10.1016/j.jcp.2021.110335. URL:https://www.sciencedirect.com/science/article/pii/S0021999121002308.
[33] A. Fabregat Tomàs, A.C. Poje, T.M. Özgökmen, W.K. Dewar, Dynamics of multiphase turbulent plumes with hybrid buoyancy sources in stratified environments, Phys. Fluids 28 (9) (2016), 095109, https://doi.org/10.1063/1.4963313 arXiv.
[34] E. Merzari, A. Obabko, P. Fischer, Spectral element methods for liquid metal reactors applications (2017). doi:10.48550/ARXIV.1711.09307. URL:https://arxiv.org/abs/1711.09307.
[35] R. Vinuesa, P. Negi, M. Atzori, A. Hanifi, D. Henningson, P. Schlatter, Turbulent boundary layers around wing sections up to rec=1,000,000, Int. J. Heat Fluid Flow 72 (2018) 86–99, https://doi.org/10.1016/j.ijheatfluidflow.2018.04.017. URL:https://www.sciencedirect.com/science/article/pii/S0142727X17311426.
[36] J. Scheel, S. Emran, J. Schumacher, Resolving the fine-scale structure in turbulent Rayleigh-Benard convection, New J. Phys. 15 (2013), https://doi.org/10.1088/1367-2630/15/11/113063.
[37] M.D. Allen, O.G. Raabe, Slip correction measurements of spherical solid aerosol particles in an improved millikan apparatus, Aerosol Sci. Technol. 4 (3) (1985) 269–286, https://doi.org/10.1080/02786828508959055, arXiv.
[38] L. Talbot, R.K. Cheng, R.W. Schefer, D.R. Willis, Thermophoresis of particles in a heated boundary layer, J. Fluid Mech. 101 (4) (1980) 737–758, https://doi.org/10.1017/S0022112080001905.
[39] J.B. McLaughlin, Inertial migration of a small sphere in linear shear flows, J. Fluid Mech. 224 (1991) 261–274, https://doi.org/10.1017/S0022112091001751.

[40] H. Ounis, G. Ahmadi, J.B. McLaughlin, Brownian particle deposition in a directly simulated turbulent channel flow, Physics of Fluids A, Fluid Dyn. 5 (6) (1993) 1427–1432, https://doi.org/10.1063/1.858578, arXiv.
[41] I.E. Barton, Exponential-lagrangian tracking schemes applied to stokes law, J. Fluids Eng. 118 (1996) 85–89.
[42] W.W. Nazaroff, G.R. Cass, Environ. Int. 15 (1989) 567–584.

UNIVERSITAT ROVIRA I VIRGILI
NUMERICAL SIMULATIONS OF PARTICLE TURBULENT DISPERSION AND
DEPOSITION WITH IMPLICATIONS FOR THE SPREADING OF AIRBORNE DISEASES
Akim Lavrinenko

Chapter 6

Conclusions and future work

6.1 Conclusions

This thesis addressed the complex dynamics of turbulent particle transport. The in-depth investigation and analysis of case studies revealed several key findings and enriched our understanding of the field. The research has analyzed different aspects of turbulent particle dispersion using numerical perspectives.

The results obtained from studying both the first and the second stages of a violent expiratory event have the potential to enhance our understanding of the dynamics of pathogen-laden aerosol dispersion in both short-term and long-term scenarios. These findings hold significant implications for the field of public health. This enhanced understanding directly contributes to the effective management and mitigation of risks associated with airborne diseases. As aerosol dispersion plays an important role in environmental science, advanced understanding of particle dispersion is crucial for predicting air pollution levels and their impact on human health and environment. Our DNS with chosen Lagrangian model demonstrates that fundamental physics of turbulent buoyancy-driven turbulent flow driven by natural convection with dispersed phase could be reproduced numerically. This opens new perspective for numerical investigation of this phenomena and provides insights into the underlying physical mechanisms, such as the interplay between gravity and thermophoresis forces, particle dispersion, and turbulent flow structures. Newly reported high Rayleigh versus Nusselt number correlation fill in the existing gap in the literature. Study of the particle deposition and dispersion within turbulent flow in the differentially heated cavity contributes to the fundamental fluid mechanics.

The detailed investigation of turbulent jet flow with dispersed phase during violent expiratory events revealed the caveats involved in modeling transient flows and the rapid decay of turbulence intensity post-exhalation in Chapter 2 of this work. The challenge of balancing computational requirements and predictive accuracy in modeling particle dynamics were investigated by the comparison between DNS and URANS equations with a $k-\epsilon$ turbulence model. Results show that URANS effectively can reproduce the general flow hydrodynamics and offers a reasonably accurate approximation of the particle cloud transport generated by the rapid exhalation. We carried out a quantitative investigation of the effect of emerging finer flow features with increasing mesh resolution on the hydrodynamics, using metrics such as the thermal field size and the position and variance of the particle cloud centroids. Findings reveal that the trajectory of particle clouds dominated by drag force (diameters ranging from 4 µm to 32 µm) align more closely with those documented in the DNS as hydrodynamics become better resolved with finer grid resolutions. Results show that particles above 32 µm in diameter to be largely unaffected by mesh resolution due to their propensity to escape the thermal puff through gravitational effects. However, despite the significant difference between the coarsest and finest grids, the relative positions of clouds for all particle sizes remained relatively consistent across the meshes considered. The URANS model, however, tends to overestimate the distance travelled by particles with diameters from 4 µm to 32 µm, while underestimating for particle diameters exceeding 64 µm comparing to the DNS. This conclusion is significant considering the complex and transient nature of the flow, which involves a transition from a laminar to a turbulent regime during the accelerated air injection and a turbulent to a laminar transition as turbulence intensity swiftly decays after the exhalation phase. Our analysis of mesh independence permitted the quantification of the cell count's influence on flow hydrodynamics, which significantly determines the dispersion of the particle cloud, particularly for smaller particles where drag dominates their transport.

Chapter 3 provides an in-depth examination of the outcomes from the international CFD challenge that centered on simulating first stage of mild expiratory event. Each team participating in the challenge simulated the flow and ensuing particle dynamics resulting from a representative violent expiratory event comprising a brief

injection of hot fluid with solid particles into a colder, initially stagnant, environment. The results were evaluated against two benchmarks - a DNS and an ensemble average of 13 independent LES. Each team performed simulations on the same flow setup but varied solvers, the grid topology and resolution and turbulence modeling methods. The study considered both evaporative and non-evaporative particles ranging from 4 to 256 µm, resulting in 12 simulations in total - seven based on URANS equations and five on LES. Results of this collaborative endeavor fulfills next key objectives. Firstly, this study lays the foundation for those interested in simulating the first stage of a violent expiratory event. The analysis of the results highlights the limitations of commonly used simulation methodologies and showcases the capabilities of URANS and LES when compared to the DNS. Secondly, it assists in generating reliable initial conditions for simulations of long-term, long-range flow and particle transport. Finally, it contributes to the development of better mitigation strategies aimed at reducing infection risks from diseases spread via pathogenic aerosols discharged during respiratory events. The analysis showed the proficiency of various computational codes and turbulence models in reproducing an idealized violent expiratory event and the resulting particle dynamics. The results, however, demonstrated a need for improvements in the modeling of vertical turbulent mixing, as it was generally underestimated by the most simulations. The used models predicted the shape and range of the buoyant thermal cloud reasonably well, affirming the potential utility of computational modeling in studying the dynamics of aerosol particles in a real-world scenarios.

Both URANS and LES based simulations accurately predicted the vertical and horizontal mixing of the new jet during the flow injection ($t \leq 0.4$ s). However, both approaches underpredicted the vertical mixing of the thermal puff after the flow injection ceased (t > 0.4 s), with the thermal cloud's vertical size being about 50% smaller in URANS and 30% smaller in LES compared to the DNS results. The trajectories and size of particle clouds predicted by the DNS were generally well-replicated by both alternative methods. The cloud centroids exhibited wider axial ranges and lower vertical displacements in comparison to the DNS for particles that remain airborne (4 to 16 µm). On the other hand, predictions more accurately reproduced the DNS for larger particles (64 to 256 µm) which follow near-ballistic

trajectories. URANS and LES were observed to overestimate the travel distance for smaller particles (4 to 16 µm) and underestimate for larger particles (greater than 64 µm). The most accurate predictions were for the particles with diameters of 32 and 64 µm. As hydrodynamics became better resolved, due to improved grid resolution, the predicted trajectories of the particle cloud centroids converged more closely with the DNS for particles in the 4 to 32 µm diameter range. Our analysis of the participant's numerical grids helped us discern how cell count affects flow dynamics, which strongly influences the dispersion of the particle clouds, especially when the particles are small and their transport is dominated by drag. We examined the emergence of more detailed flow characteristics as the mesh resolution increases, and how this affects the hydrodynamics and turbulence mixing intensity using thermal field size, and the position and variance of the particle cloud centroids. The turbulence model used for URANS simulations had minimal impact on the prediction of the thermal puff's position and extent. Yet, finer spatial resolution in URANS simulations resulting in better agreement with the DNS data.

In chapter 4 through DNS we explored the dispersion of aerosols in buoyancy-driven turbulent flows within enclosed spaces using the second stage of the violent expiratory event as case study. Particularly, aerosol cloud dynamics analyses revealed that particles ranging from 0.1 to 2.5 µm become homogeneously distributed within the first 500 s after the release in a cubical room (Side length $\sim$3 m) with two pairs of opposed horizontal and vertical walls kept at different temperature. Also, the dispersion rate of particle clouds remains the same within the cavity but overall cloud mixing time is strongly affected by the initial location of the particle cloud. Simulation results revealed that particle clouds initially located in the regions with high temperature and velocity gradient (near the thermally active walls) onset dispersion much faster than those initially located within the central region of the cavity with low velocity and low temperature difference. Results revealing no discernible difference in the dispersion rate across considered particle sizes under studied conditions. This conclusions provide insights into the pathogen-laden aerosol dispersion within indoor environments with large-scale recirculating flow and their implications for the spread of airborne diseases.

A new analytical model of aerosol cloud dispersion in enclosed room with recirculating flow developed during these project and the results of the semi-analytical model proposed by Lau et al. [33] revealed, that due to assumptions and simplifications models tend to overpredict mixing rates of particle clouds in indoor spaces. Despite this, models showed some estimations of the time required to achieve fully mixed conditions. Comparison with the Gaussian dispersion models emphasized the importance of turbulence distribution within the room and demonstrated limited abilities of these models to predict accurate mixing time in turbulent enclosed flows.

These findings expose the complexity inherent to enclosed turbulent buoyancy-driven flows, characterized by large-scale recirculation patterns and local turbulence-induced instabilities. Despite the simplicity of the geometry and mechanism of action, the turbulence engenders a non-homogeneous, time and space-dependent dispersion coefficient.

Overall, our study advances the understanding of aerosol cloud behavior in confined spaces with background air currents, underscoring the shortcomings of current analytical models. The insight into particle cloud dynamics and dispersion rates offers critical data for refining these models and underscores the necessity for ongoing research to devise innovative, efficient, and computationally economical modelling methods.

In chapter 5, DNS is used to explore the turbulent convective flow in a cubical cavity, with two opposing thermally active wall pairs with Rayleigh number of 3.6×10^9 and to examine the transport and deposition of suspended particles in this environment.

Time-averaged hydrodynamic field data allowed to extend the established correlations between the Rayleigh number and the wall-averaged Nusselt number to as high as 3.6×10^9 filling in an existing gap in the literature. Particle deposition rates are reported on each thermally active wall of the cavity and compared with results of the Boundary Layer (BL) model and results of identical experimental setup of Thatcher et al. [20]. The study employed a disperse phase transport model, which took into account five forces: hydrodynamic drag, buoyancy, lift, thermophoresis, and Brownian motion. It is found that this model could accurately predict wall

deposition rates for particles of various sizes, including those dominated by thermophoretic and buoyancy forces at a relatively high Rayleigh number.

Results indicated that the a classical Boundary Layer (BL) model can precisely predict the deposition velocity of supermicron particles at Ra = 3.6×10^9. However, for submicron particles, comparison with the DNS predictions showed discrepancies. This could be attributed to the assumptions made during the derivation of the BL solutions. When the effect of thermophoresis was similar to, or exceeded, gravitational force, these models tended to overestimate deposition on horizontal walls. Notably, our DNS predictions for supermicron particle deposition velocity were in excellent agreement with both experimental results and the BL model. We noticed differences when particle size dropped below one micron and thermophoresis became the dominating force. Literature suggests that these significant differences could be due to the effect of particle agglomeration and the chosen thermophoresis model. In depth literature analysis suggested that for submicron particles with dominant thermophoresis forces model proposed by Beresnev and Chernyak [34] gives better results than the model proposed by Talbot et al. [35], which was used in this study.

Overall, our findings suggest that thermophoretic forces heavily influence the deposition of submicron particles. Conversely, thermophoresis has negligible impact on the deposition rate of particles larger than one micron, which is predominantly governed by buoyancy forces.

In essence, this thesis presents an investigation of the dynamic interplay between turbulent flow and particle dispersion, providing valuable insights that could contribute to the development of more accurate and efficient models for predicting particle dispersion and deposition in turbulent flows. The findings pave the way for future research endeavors aimed at improving our understanding and control of particle transport in confined spaces, with valuable implications for public health and safety, environmental engineering and fundamental fluid mechanics.

6.2 Future work

The results open new avenues for future research, focusing on enhancing our comprehension and management of aerosol dynamics.

- Incorporation of Realistic Anatomy: Future research endeavors should aim to incorporate the realistic anatomy of the human respiratory system into the simulation models. This would entail modelling realistic oral and nasal passages,the throat and upper regions of the lungs, allowing a more accurate representation of aerosol production and expulsion during violent expiratory events.

- Integration of Body Movements: The introduction of head and body movements into the current simulation models is another avenue worth exploring. As people are naturally mobile during speech, coughing, or sneezing, the integration of these movements could offer a more realistic depiction of how aerosols spread and disperse in various directions.

- Investigation of Complex and Realistic Environments: The studies were conducted in a cubical cavity representing a room. However, real-life indoor environments are typically more complex, with furniture, people, and ventilation systems. Real-world environments, replete with complex background air currents, can significantly augment the realism and relevance of the current models. Thus, future studies could focus on more complex geometries and conditions that better mimic realistic scenarios.

- Exploration of the Nusselt Number versus Rayleigh Number Correlation: Future studies should leverage LES and URANS simulations to generate predictions of Nusselt numbers across a broad range of Rayleigh numbers. The comparison of these predictions to DNS and experimental results could validate the accuracy of LES and URANS simulations, ultimately enabling refinements to existing models as necessary.

- Comparative Study of Particle Deposition Predictions: The predictions of particle deposition rates obtained from LES and URANS simulations should be

compared with DNS and experimental data. This comparison can provide valuable insights into the accuracy of LES and URANS simulations in predicting particle deposition, revealing opportunities for model refinement and advancement.

- Examine the efficacy of the thermophoresis model proposed by Beresnev and Chernyak [34] in precisely forecasting the dynamics and deposition rates of submicron particles within a cubical cavity featuring high Rayleigh numbers.

By exploring these proposed avenues of research, we can build upon the findings presented in this thesis to further deepen our understanding of the intricate dynamics involved in particle transport. Such knowledge is instrumental in fostering the development of more accurate, robust, and comprehensive models that can significantly improve the predictive capabilities of our simulations. It is also worth noting that these enhanced understanding and refined models can inform the development of passive tools for mitigating particle deposition and drive advancements in air filtration methodologies. Ultimately, these endeavors could contribute significantly to public health and environmental science, providing vital tools and knowledge for managing and mitigating the risks associated with airborne diseases.

References

1. Navier C. Mémoire sur les lois du mouvement des fluides. Bulletin de la Société philomathique de Paris 1822; 3:138–42
2. Stokes G. On the Theories of the Internal Friction of Fluids in Motion and of the Equilibrium and Motion of Elastic Solids. Transactions of the Cambridge Philosophical Society 1845; 8:287–319
3. Stokes G. On the effect of the internal friction of fluids on the motion of pendulums. Transactions of the Cambridge Philosophical Society 1845; 9:8–106
4. Reynolds O. Experiment XXIX. An experimental investigation of the circumstances which determine whether the motion of water shall be direct or sinuous, and of the law of resistance in parallel channels. Philosophical Transactions of the Royal Society of London 1883; 174:935–82. DOI: 10.1098/rstl.1883.0029
5. Basset A. B. Treatise on Hydrodynamics. Vol. 2. London: Deighton Bell, 1888
6. Boussinesq J. V. Theorie Analytique de la chaleur. Vol. 2. Paris: I'Ecole Polytechnique, 1903
7. Oseen C. W. Hydrodynamik. Leipzig, 1927
8. Taylor G. I. Diffusion by Continuous Movements. Proceedings of the London Mathematical Society. Series 2 1921; 20:196–212
9. Wells W. F. On air-borne infection: study II. Droplets and droplet nuclei. American Journal of Epidemiology 1934 Nov; 20:611–8. DOI: 10.1093/oxfordjournals.aje.a118097
10. Kolmogorov A. N. The local structure of turbulence in incompressible viscous fluid for very large Reynolds numbers. Doklady Akademii Nauk SSSR 1941; 30:299–303. DOI: 10.1098/rspa.1991.0075

11. Tchen C. M. Mean value and correlation problems connected with the motion of small particles suspended in a turbulent fluid. PhD thesis. The Hague: Delft, Hydraulic Engineering Department, 1947

12. Obukhov A. M. Structure of the temperature field in a turbulent flow. Izvestiya Akademii Nauk SSSR, Seriya Geograficheskaya i Geofizicheskaya 1949; 13:58–69

13. Batchelor GK. The Theory of Homogeneous Turbulence. Proceedings of the Royal Society A: Mathematical, Physical and Engineering Sciences 1953; 213:349–66

14. Corrsin S and Lumley J. On the equation of motion for a particle in turbulent fluid. Appl. Sci. Res. A 1956; 6:114

15. Buevich O. A. Motion resistance of a particle suspended in a turbulent medium. Fluid Dynamics 1966; 1:119

16. Riley J. The road corrugation phenomenon: a simulation and experimental evaluation. PhD thesis. Baltimore, Maryland: The Johns Hopkins University, 1971

17. Maxey Martin R and Riley James J. Equation of motion for a small rigid sphere in a nonuniform flow. Physics of Fluids 1983; 26:883–9. DOI: 10.1063/1.864230

18. Nazaroff William W and Cass Glen R. Mathematical modeling of indoor aerosol dynamics. Environmental Science & Technology 1989; 23:157–66. DOI: 10.1021/es00179a003

19. Xu M, Nematollahi M, Sextro RG, Gadgil AJ, and Nazaroff WW. Deposition of Tobacco Smoke Particles in a Low Ventilation Room. Journal of Aerosol Science 1994; 25:1477–90. DOI: 10.1080/02786829408959676

20. Tracy L. T, Wendy A. F, and William W. N. Particle Deposition from Natural Convection Enclosure Flow Onto Smooth Surfaces. Aerosol Science and Technology 1996; 25:359–74. DOI: 10.1080/02786829608965402

21. Fabregat A and Pallarès J. Heat transfer and boundary layer analyses of laminar and turbulent natural convection in a cubical cavity with differently heated opposed walls. International Journal of Heat and Mass Transfer 2020; 151:119409. DOI: https://doi.org/10.1016/j.ijheatmasstransfer.2020.119409

22. Fabregat A and Pallarès J. Transport and wall surface deposition of airborne particles in enclosed, buoyancy-driven turbulent flows using fully-resolved numerical simulations. International Communications in Heat and Mass Transfer 2022; 134:106048. DOI: https://doi.org/10.1016/j.icheatmasstransfer.2022.106048

23. Pallares J and Fabregat A. Prediction of particle deposition on the walls of a cubical cavity with differentially heated opposed walls using heat and mass transfer laminar mixed convection boundary layer models. International Journal of Heat and Mass Transfer 2021; 165:120691. DOI: https://doi.org/10.1016/j.ijheatmasstransfer.2020.120691

24. Fabregat A, Gisbert F, Vernet A, Dutta S, Mittal K, and Pallares J. Direct numerical simulation of the turbulent flow generated during a violent expiratory event. Physics of Fluids 2021; 33. 035122. DOI: 10.1063/5.0042086

25. Fabregat A, Gisbert F, Vernet A, Ferré JA, Mittal K, Dutta S, and Pallarès J. Direct numerical simulation of turbulent dispersion of evaporative aerosol clouds produced by an intense expiratory event. Physics of Fluids 2021; 33. 033329. DOI: 10.1063/5.0045416

26. Pallares J and Fabregat A. A model to predict the short-term turbulent indoor dispersion of small droplets and droplet nuclei released from coughs and sneezes. Indoor and Built Environment 2022; 31:1393–404. DOI: 10.1177/1420326X211060001

27. Pallares J, Fabregat A, Lavrinenko A, Norshamsudin HA bin, Janiga G, Fletcher DF, Inthavong K, Zasimova M, Ris V, Ivanov N, Castilla R, Gamez-Montero PJ, Raush G, Calmet H, Mira D, Wedel J, Štrakl M, Ravnik J, Fontes D, Souza FJ de, Marchioli C, and Cito S. Numerical simulations of the flow and aerosol dispersion in a violent expiratory event: Outcomes of the "2022 International Computational Fluid Dynamics Challenge on violent expiratory events". Physics of Fluids 2023; 35:045106. DOI: 10.1063/5.0143795

28. Baughman A. V, Gadgil Ashok J, and Nazaroff William W. Mixing of a Point Source Pollutant by Natural Convection Flow within a Room. Indoor Air 1994; 4:123–36. DOI: 10.1111/j.1600-0668.1994.t01-2-00006.x

29. Fischer PF, Lottes JW, and Kerkemeier SG. NEK5000. Available from: http://nek5000.mcs.anl.gov [Accessed on: 2023 Jun 21]

30. OpenFoam. Available from: https://www.openfoam.com/ [Accessed on: 2023 Sep 21]

31. Paraview. Available from: https://www.paraview.org/ [Accessed on: 2023 Sep 21]

32. Visit. Available from: https://visit-dav.github.io/visit-website/index.html [Accessed on: 2023 Sep 21]

33. Lau Z, Griffiths IM, English A, and Kaouri K. Predicting the spatio-temporal infection risk in indoor spaces using an efficient airborne transmission model. Proceedings of the Royal Society A: Mathematical, Physical and Engineering Sciences 2022; 478:20210383. DOI: 10.1098/rspa.2021.0383. Available from: https://royalsocietypublishing.org/doi/abs/10.1098/rspa.2021.0383

34. Beresnev S and Chernyak V. Thermophoresis of a spherical particle in a rarefied gas: Numerical analysis based on the model kinetic equations. Physics of Fluids 1995 Jul; 7. DOI: 10.1063/1.868489

35. Talbot L, Cheng RK, Schefer RW, and Willis DR. Thermophoresis of particles in a heated boundary layer. Journal of Fluid Mechanics 1980; 101:737–758. DOI: 10.1017/S0022112080001905

UNIVERSITAT ROVIRA I VIRGILI
NUMERICAL SIMULATIONS OF PARTICLE TURBULENT DISPERSION AND
DEPOSITION WITH IMPLICATIONS FOR THE SPREADING OF AIRBORNE DISEASES
Akim Lavrinenko

UNIVERSITAT ROVIRA I VIRGILI
NUMERICAL SIMULATIONS OF PARTICLE TURBULENT DISPERSION AND DEPOSITION WITH IMPLICATIONS FOR THE SPREADING OF AIRBORNE DISEASES
Akim Lavrinenko

UNIVERSITAT
ROVIRA i VIRGILI